Development of a Cable Robot and Measurement of Stay Cable Roundness

PUBLICATION NO. FHWA-HRT-24-043

MARCH 2024

U.S. Department of Transportation
Federal Highway Administration

Research, Development, and Technology
Turner-Fairbank Highway Research Center
6300 Georgetown Pike
McLean, VA 22101-2296

FOREWORD

Cable-stayed bridges have become the form of choice over the past several decades for bridges with medium to long spans. In some cases, serviceability problems have been observed involving large amplitude vibrations of stay cables under certain wind and wind-rain conditions. This study was conducted in response to State transportation departments' requests to develop improved design guidance for mitigation of excessive cable vibrations on cable-stayed bridges. Previous research has shown that cable shape can play an important role in the aerodynamic stability of cables. This study included the development of a unique robotic device to climb and scan the out-of-roundness of in-service bridge stay cables. The study also included the use of this device to scan and document the shapes of representative stay cables from 11 major cable-stayed bridges located in the eastern United States. The results of this study will be made available to the Post-Tensioning Institute's DC-45 Cable-Stayed Bridge Committee for consideration during their periodic updates of *Recommendations for Stay Cable Design, Testing and Installation*.[1]

This report will be of interest to bridge engineers, wind engineers, and consultants involved in the design of cable-stayed bridges. It is the ninth in a series of published reports addressing the subject of aerodynamic stability of bridge stay cables. (See references 2–9.)

Jean A. Nehme, Ph.D., P.E.
Director, Office of Infrastructure
Research and Development

Notice

This document is disseminated under the sponsorship of the U.S. Department of Transportation in the interest of information exchange. The U.S. Government assumes no liability for the use of the information contained in this document.

Non-Binding Contents

Except for the statutes and regulations cited, the contents of this document do not have the force and effect of law and are not meant to bind the States or the public in any way. This document is intended only to provide information regarding existing requirements under the law or agency policies.

Quality Assurance Statement

The Federal Highway Administration (FHWA) provides high-quality information to serve Government, industry, and the public in a manner that promotes public understanding. Standards and policies are used to ensure and maximize the quality, objectivity, utility, and integrity of its information. FHWA periodically reviews quality issues and adjusts its programs and processes to ensure continuous quality improvement.

Disclaimer for Product Names and Manufacturers

The U.S. Government does not endorse products or manufacturers. Trademarks or manufacturers' names appear in this document only because they are considered essential to the objective of the document. They are included for informational purposes only and are not intended to reflect a preference, approval, or endorsement of any one product or entity**.**

TECHNICAL REPORT DOCUMENTATION PAGE

1. Report No. FHWA-HRT-24-043	2. Government Accession No.	3. Recipient's Catalog No.
4. Title and Subtitle Development of a Cable Robot and Measurement of Stay Cable Roundness		5. Report Date March 2024
		6. Performing Organization Code:
7. Author(s) Harold R. Bosch and James R. Pagenkopf (ORCID: 0000-0001-5392-8628)		8. Performing Organization Report No.
9. Performing Organization Name and Address Genex Systems, LLC 11848 Rock Landing Dr., Suite 303 Newport News, VA 23606		10. Work Unit No. 11. Contract or Grant No. DTFH61-13-D-00011
12. Sponsoring Agency Name and Address Office of Research, Development, and Technology Federal Highway Administration 6300 Georgetown Pike McLean, VA 22101-2296		13. Type of Report and Period Covered Final Report; March 2014–January 2018 14. Sponsoring Agency Code HRDI-40

15. Supplementary Notes
The Contracting Officer's Representative was Harold R. Bosch (HRDI-40).

16. Abstract

A previous study involving a wind tunnel investigation of a stay cable found that rotating the cable along its longitudinal axis changed its wind-induced response, revealing that the slight eccentricity of the cross-sectional shape was influencing the response. The study speculates that surface deformation could have caused nonsymmetrical separation of the boundary layer on either side of the cable, inducing across-wind forces and other instabilities.

Although using high-density polyethylene pipe is an extremely popular method to shield a stay cable's steel strands from environmental impacts, not much is known about its exact geometry other than a few simple characteristics such as nominal diameter and pipe thickness. While the cross-sectional shape is often assumed to be circular, the actual shapes found in the field are generally unknown and could be affected by various factors, including manufacturing, storage, and sag-deformations over time. To study these shapes, an FHWA team built a cable robot capable of climbing stay cables and taking cross-sectional measurements of the pipes in the field. This report discusses the design process for developing the robot, including automating and calibrating the robot and analyzing the resulting field data.

The team selected and visited 11 bridge sites during testing, and the results are presented and discussed, including visualizations of the cable shapes. Overall, 67 individual cables were tested and over 1,700 roundness measurements were recorded. Averaged eccentricity values ranged from 0.8–5.2 percent per cable.

17. Key Words	18. Distribution Statement
Cable-stayed bridges, cables, vibrations, HDPE, pipe roundness, helical fillets, hazard mitigation	No restrictions. This document is available to the public through the National Technical Information Service, Springfield, VA 22161. https://www.ntis.gov

19. Security Classif. (of this report)	20. Security Classif. (of this page)	21. No. of Pages	22. Price
Unclassified	Unclassified	122	N/A

SI* (MODERN METRIC) CONVERSION FACTORS

APPROXIMATE CONVERSIONS TO SI UNITS

Symbol	When You Know	Multiply By	To Find	Symbol
		LENGTH		
in	inches	25.4	millimeters	mm
ft	feet	0.305	meters	m
yd	yards	0.914	meters	m
mi	miles	1.61	kilometers	km
		AREA		
in^2	square inches	645.2	square millimeters	mm^2
ft^2	square feet	0.093	square meters	m^2
yd^2	square yard	0.836	square meters	m^2
ac	acres	0.405	hectares	ha
mi^2	square miles	2.59	square kilometers	km^2
		VOLUME		
fl oz	fluid ounces	29.57	milliliters	mL
gal	gallons	3.785	liters	L
ft^3	cubic feet	0.028	cubic meters	m^3
yd^3	cubic yards	0.765	cubic meters	m^3
	NOTE: volumes greater than 1,000 L shall be shown in m^3			
		MASS		
oz	ounces	28.35	grams	g
lb	pounds	0.454	kilograms	kg
T	short tons (2,000 lb)	0.907	megagrams (or "metric ton")	Mg (or "t")
		TEMPERATURE (exact degrees)		
°F	Fahrenheit	5 (F-32)/9 or (F-32)/1.8	Celsius	°C
		ILLUMINATION		
fc	foot-candles	10.76	lux	lx
fl	foot-Lamberts	3.426	$candela/m^2$	cd/m^2
		FORCE and PRESSURE or STRESS		
lbf	poundforce	4.45	newtons	N
lbf/in^2	poundforce per square inch	6.89	kilopascals	kPa

APPROXIMATE CONVERSIONS FROM SI UNITS

Symbol	When You Know	Multiply By	To Find	Symbol
		LENGTH		
mm	millimeters	0.039	inches	in
m	meters	3.28	feet	ft
m	meters	1.09	yards	yd
km	kilometers	0.621	miles	mi
		AREA		
mm^2	square millimeters	0.0016	square inches	in^2
m^2	square meters	10.764	square feet	ft^2
m^2	square meters	1.195	square yards	yd^2
ha	hectares	2.47	acres	ac
km^2	square kilometers	0.386	square miles	mi^2
		VOLUME		
mL	milliliters	0.034	fluid ounces	fl oz
L	liters	0.264	gallons	gal
m^3	cubic meters	35.314	cubic feet	ft^3
m^3	cubic meters	1.307	cubic yards	yd^3
		MASS		
g	grams	0.035	ounces	oz
kg	kilograms	2.202	pounds	lb
Mg (or "t")	megagrams (or "metric ton")	1.103	short tons (2,000 lb)	T
		TEMPERATURE (exact degrees)		
°C	Celsius	1.8C+32	Fahrenheit	°F
		ILLUMINATION		
lx	lux	0.0929	foot-candles	fc
cd/m^2	candela/m2	0.2919	foot-Lamberts	fl
		FORCE and PRESSURE or STRESS		
N	newtons	2.225	poundforce	lbf
kPa	kilopascals	0.145	poundforce per square inch	lbf/in^2

*SI is the symbol for International System of Units. Appropriate rounding should be made to comply with Section 4 of ASTM E380. (Revised March 2003)

TABLE OF CONTENTS

LIST OF FIGURES

LIST OF TABLES

CHAPTER 1. INTRODUCTION

With the growing popularity of cable-stayed bridges as the design form of choice for new medium- and long-span bridge construction, there has been a corresponding increase of studies regarding the behavior of these cables. Various issues have been reported, most notably the cables ease of excitation into galloping when subjected to certain wind loads, especially during rainy conditions. Many cable vibration mitigation solutions have been proposed and adopted, including dampers, crossties, and surface treatments, but the aerodynamics of these cables are complex and still being explored.

The Federal Highway Administration (FHWA) has initiated many studies on cables in this timeframe, including investigating the dynamic properties of cables during various stages of bridge construction, developing guidelines to prevent dry-galloping and other undesired behaviors, and investigating the effectiveness of surface treatments, such as a helical fillet.

An interesting phenomenon was discovered during a wind tunnel investigation of an inclined cable with a helical fillet: When the cable was rotated along its axis, the wind-induced response changed dramatically, revealing that the test cable's cross section was not perfectly round and that the cable's eccentricity affected the response more than expected.[4]

The National Research Council of Canada (NRC) performed this FHWA-sponsored study at the NRC's 3-by-6-m Propulsion and Icing Wind Tunnel, a facility that allows for full-scale cable testing. The initial purpose of the study was to explore a cable's dynamic response at various inclination and yaw angles, in both laminar and turbulent flow, and with and without a helical fillet. During one round of testing, observers noted large amplitude displacements in the first sway mode (across-wind) of 30–75 mm at a specific rotation angle, but at other rotation angles, these displacements remained at or below 10 mm. Making matters more complex, the maximum measured eccentricity was only 1 percent of the mean diameter, which would not initially appear significant. The report speculates that the surface deformation could have caused nonsymmetrical separation of the boundary layer on either side of the cable, inducing across-wind forces and other instabilities.

However, this study's primary purpose was not to test for cable rotation, and with limited testing time available in the wind tunnel, the researchers could not diverge from the planned schedule to explore the issue further. However, the report concluded that future tests should be designed to focus on studying in detail cables with various cross sections and different cable rotations.

Before future tests could be designed to explore this issue in more detail, there needed to be a better understanding of the cross-sectional shapes of cables that currently exist in the field. The cables of most cable-stayed bridges comprise numerous steel wire strands protected by a high-density polyethylene (HDPE) pipe. A common practice is to place a neoprene bushing inside the anchorage guide pipe near its upper end to keep the strands centered and protect the strands/anchorage. Sometimes, cement grout is pumped into the HDPE pipe to further protect the strands. Usually, the HDPE pipe is shipped to the bridge site as roughly 9-m-long segments that are welded together onsite, creating longer lengths to form a complete stay cable. This assembly

procedure can introduce even more randomness to the shape of the pipe, as the cross section could change or rotate multiple times over the full length of the stay cable.

Each segment of produced HDPE pipe has three known simple characteristics: nominal diameter, pipe wall thickness, and unit weight. However, the tolerances for these characteristics are not always well defined. While the cross-sectional shape is assumed to be circular, the extrusion process can introduce a small amount of initial eccentricity. When pipes are stacked for long periods of time at a warehouse or bridge site, their cross-sectional shape can potentially be affected. Similarly, once the pipes are mounted on the cable, no data exists for whether the pipes exhibit any sag (creep) issues, and if those deflections worsen over time.

To study this issue, FHWA authorized a new project to design and build a robot capable of climbing a variety of stay cables in the field and measuring their cross sections. From these scans, FHWA could develop a database of typical cable cross-sectional shapes, with a selection of the more interesting shapes studied further in future wind tunnel tests. The cross-sectional shapes could also complement some of the recent research on the effects of cable shape and surface roughness on aerodynamic properties and behavior.[10,11]

This report documents the design and development of the robot at the former Aerodynamics Laboratory at Turner-Fairbank Highway Research Center (TFHRC) and discusses the robot's automation and measurement capabilities. The report also discusses the software created for postprocessing the measurement data and includes a chapter for every bridge test site featuring a brief description of the bridge, a summary of the cables tested, and plots of the resulting data. Finally, the report summarizes and discusses the full results from all testing.

CHAPTER 2. DESIGN AND DEVELOPMENT

INITIAL DISCUSSION

Preliminary meetings began in fall 2013 to brainstorm the different requirements of the robot. Initial discussions included how the robot would climb the cable, how the robot would take measurements, and to determine any of the potential obstacles the robot would encounter. In addition to these discussions, journal and conference papers were collected and shared regarding existing cable robots. (See references 12–16). Most existing cable- and pole-climbing robots were constructed to perform functions related to the routine inspection, cleaning, or painting of cables; none of the discovered robots took roundness measurements.

To establish the target parameters or characteristics for the new robot, project staff engineers, system control programmers, and equipment fabricators convened many brainstorming sessions. Once a consensus was reached on the overall concept for the prototype, the team established the following key requirements:

- Ability to measure a range of cable diameters between 100 and 300 mm (originally up to 400 mm, but the robot would have been too large).
- Maximum weight of 23 kg (so two people can deploy it).
- Climb inclination angle between 20 and 70 degrees.
- Laser precision of 0.1 mm.
- Ability to climb past fillets and joints (acceptable to not pass tougher obstacles like crossties).

The final concept included four circular platform rings that would surround the cable. Two of the platforms would move relative to each other, and both of these two platforms would have a set of three retractable clamps. By alternatingly gripping the pipe with each set of clamps, the robot could shuffle its way up the cable. A third platform ring would contain the measuring equipment, consisting of dual lasers mounted on a carriage that could roll along a precision gear to navigate the exterior of the cable. The fourth platform would be used to help stabilize the two clamping platforms. All the platforms would be attached by a series of steel rods, and each platform could separate in half by use of a hinge, allowing the robot to be opened and closed to mount on the cable.

INITIAL CONSTRUCTION

With the final concept and list of requirements defined as per the previous section, construction on the robot began in winter 2013 by an outside contractor specializing in robotics. The contractor's role was to create a functional version of the robot, including the frame and all basic electromechanical parts plus a hard-wired controller to operate the mechanics. Contractor staff in the FHWA Aerodynamics Laboratory would later add automated computer control of the robot

and data acquisition capabilities. The initial version of the robot arrived at the Aerodynamics Laboratory in fall 2014.

The robot includes four steel-ring platform plates, three of which are used for climbing while the fourth supports the measurement equipment. The rings have an outer diameter of 45.72 cm and an inner diameter of about 34.29 cm, with a thickness of about 6.35 mm. However, the rings contain areas that extend beyond this stated outer diameter where the hinge and stabilizer shafts are mounted and where the clamps are mounted on the inner rings. Each ring is split into left and right halves so that the robot can be opened and then mounted on the cable. These halves are connected at the hinge shaft and close opposite the shaft with a bolt attached to a large plastic knob. In addition to the 16-mm diameter hinge shaft, two 20-mm diameter stabilizer shafts are mounted on either side of the connector bolt. All three shafts are 91.44 cm tall and are mounted to the platforms with bearing blocks, except for the middle ring, which is attached using slide bearings that allow that platform to move. An eye screw is located at the top of the hinge shaft, which allows a lift to pick up the robot if necessary.

This middle ring platform, ring A, is the only platform that can move along the three shafts. The lower climbing ring platform, ring B, is locked in place on the shafts. These two rings have three mounted retractable clamps that grip the pipe. The topmost platform, ring C, has no clamps and is also locked in place at the top of the robot, which helps keep the shafts stable while the robot is climbing. The bottom platform, the laser ring, carries the measurement equipment. This ring is mounted 100 mm directly below ring B and is locked directly to the shafts. Figure 1 shows a photo of the initial robot with all four rings labeled.

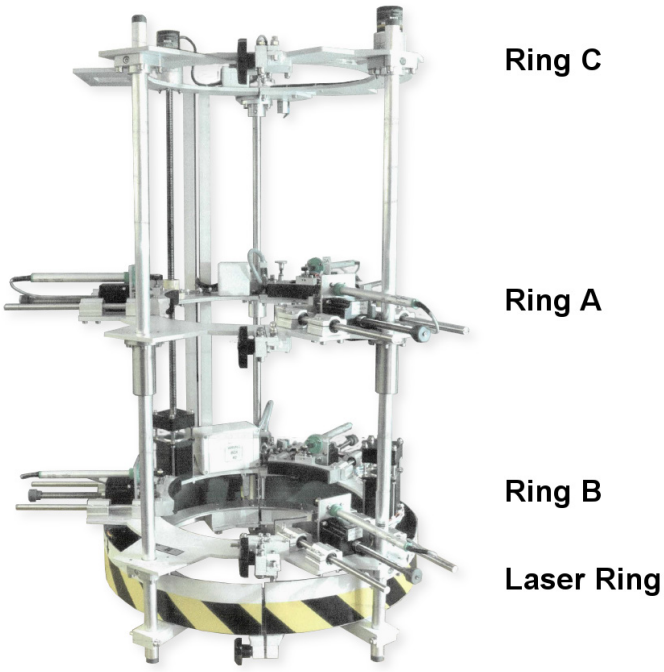

Source: FHWA.

Figure 1. Photo. The cable robot's four rings.

Rings B and C are stationary and connected by a pair of trapezoid spindles, which act as power screws to linearly move ring A up and down in an elevator motion. A stepper motor located on ring B controls each spindle, while a rotary encoder on ring C measures rotations. A special bar mounted on ring A will trigger limit switches if the platform gets too close to either rings B or C. Ring A has about 472-mm range of motion.

Rings A and B each have three clamp assemblies spaced evenly apart at 120 degrees, which grip the cable. Figure 2 shows a schematic drawing of the clamp assemblies mounted on a ring, with the shafts labeled. Each clamp assembly is composed of a curved bracket head that can be extended or retracted using a smaller trapezoid spindle controlled by a small stepper motor. The bracket head has additional support on either side of the spindle from a pair of guide shafts mounted securely to the ring platform with linear bearings. A linear potentiometer on top of the clamp assembly provides accurate positioning data related to the clamp's bracket head. A pair of limit switches mounted on either side of the stepper motor keep the clamp's bracket head positioned within an acceptable range.

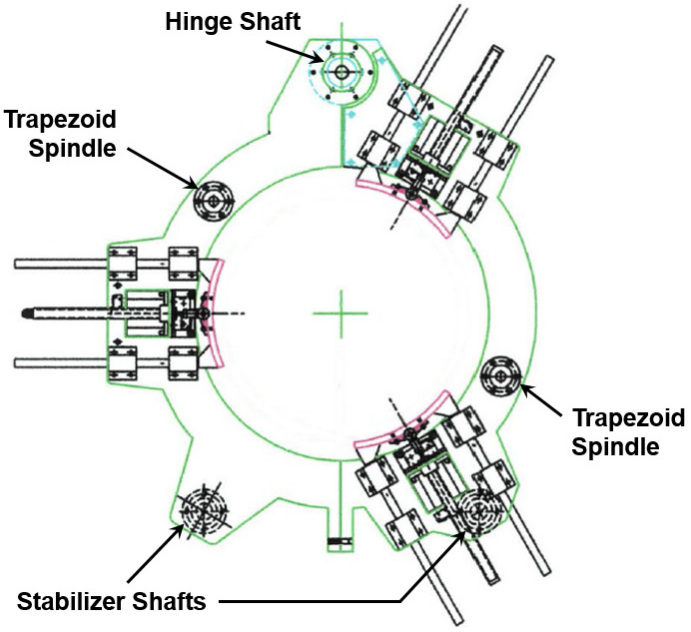

Source: FHWA.

Figure 2. Illustration. A schematic drawing of rings A and B showing the location of the three clamp assemblies.

The laser ring platform is mounted below ring B and contains the laser measurement equipment. Attached to the platform are two specialty rings, a precision ring guide with V-shaped edges on which the laser carriage can smoothly roll, and a toothed gear ring that allows a stepper motor to drive the laser carriage around the ring. The laser carriage, shown in figure 3, consists of the stepper motor to drive the carriage, a pinion gear to connect the stepper motor to the toothed gear ring, four "V-rollers" that support the carriage along the precision ring, two laser-distance sensors, and the electronic equipment that controls the carriage. A flexible housing carries and protects the wires that transmit data from the laser sensors and control the stepper motor. An

80-mm-high plastic housing surrounds the laser ring platform to protect the laser sensors from glare and any loose obstructions.

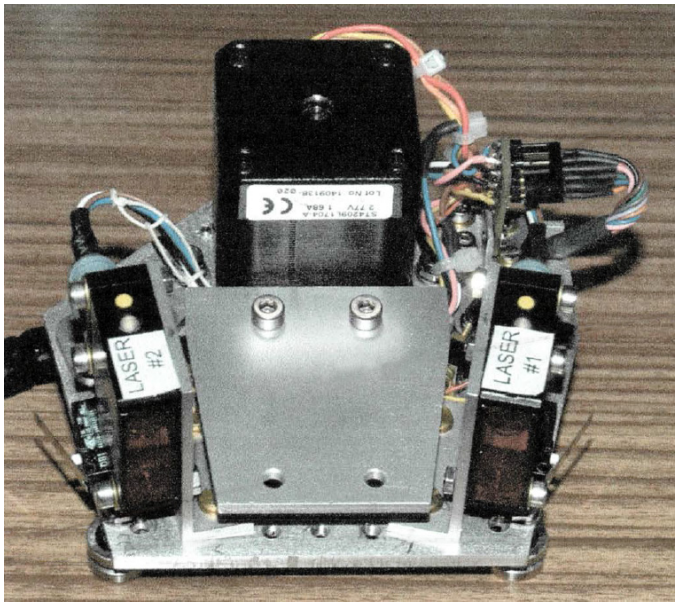

Source: FHWA.

Figure 3. Photo. The laser carriage.

The robot can be manually operated using the control unit, a large box containing the electrical circuitry that controls the stepper motors and receives signal feedback from the encoders, linear potentiometers, laser sensors, and limit switches. In the control unit, eight stepper drive boards control each individual stepper motor by first selecting a turn direction and then, when an "enable" command is applied, running the motor via a clock pulse. Also in the control unit is an analog board that converts the output of the linear potentiometers from 0 to 10 V to a distance of 0–103 mm. Additionally, the analog board converts the output from the rotary encoders and creates voltages from the limit switches. The control unit contains a power supply board that generates supply voltages of ±15 V and two power supply units that supply +24 V with 4.5 A capacity and +5 V with 4 A capacity, respectively.

The front panel of the control unit box, shown in figure 4, contains all the knobs and buttons to manually control the robot, while the back panel has the input/output interface connector to control the robot via a computer. The back panel also contains a series of three connectors that connect the control box to wiring box no. 2 on ring B of the robot via a 15.24-m-long instrumentation cable carrying 62 stranded wires. From wiring box no. 2, the wires run through a special housing, mounted next to the hinge shaft, that connects the wires to junction boxes on each remaining ring. The wires are separated at each junction box and then connect to each individual stepper motor, sensor, or limit switch.

Source: FHWA.

Figure 4. Photo. The front panel of the control unit box.

The robot control unit requires a standard 110 V/60 Hz/1 A power supply. Power consumption is 20 W when three clamps are activated and 80 W when the elevator stepper motors are activated, totaling a maximum load of 100 W. Note that while there are two sets of three clamps, only one set will be active and require power at a time.

A complete set of instructions accompanied the cable robot, the control unit, and cables. These instructions included photos and schematics labeling all parts, wiring diagrams, detailed descriptions of all electronics, and an overview of how to control the robot. Also included were a list of safety checks to perform before using the robot and maintenance routines to keep the robot in prime operating condition.

AUTOMATION

Following the delivery of the robot and initial setup and tests, lab contract staff began connecting the robot control unit to a laptop computer for automated control of the robot. A multifunctional input/output data acquisition module (DAQ module) was selected for this purpose. Designed for mobile applications, this portable module is powered via USB and does not require an external power supply. The DAQ module can read and write at fast sampling rates to both digital and analog inputs and outputs and connects to the control unit through the interface connector on the back panel. The module's USB connection allows it to communicate via LabVIEW™ software installed on a laptop.[(17)] LabVIEW simplifies the coding by offering pre-programmed blocks of software that easily allow users to check inputs, send commands, and acquire and process data.

After setting up the DAQ module, the team had to figure out how to program the stepper motors, starting with the motors for the clamps. They quickly discovered that the DAQ module did not contain enough pins to individually control all nine of the stepper motors, so a supplementary microcontroller was connected, adding 54 pins. The addition of the microcontroller helped with the LabVIEW programming because lower-level commands could be programmed directly into the microcontroller, simplifying the commands on the laptop. For example, a simple "close clamp" command could be sent to the microcontroller from LabVIEW, which would trigger a subroutine that could be directed toward a specific clamp. Figure 5 shows the DAQ

module and the microcontroller mounted in a custom three-dimensional (3D)-printed storage box, which was connected between the laptop computer and the control unit box.

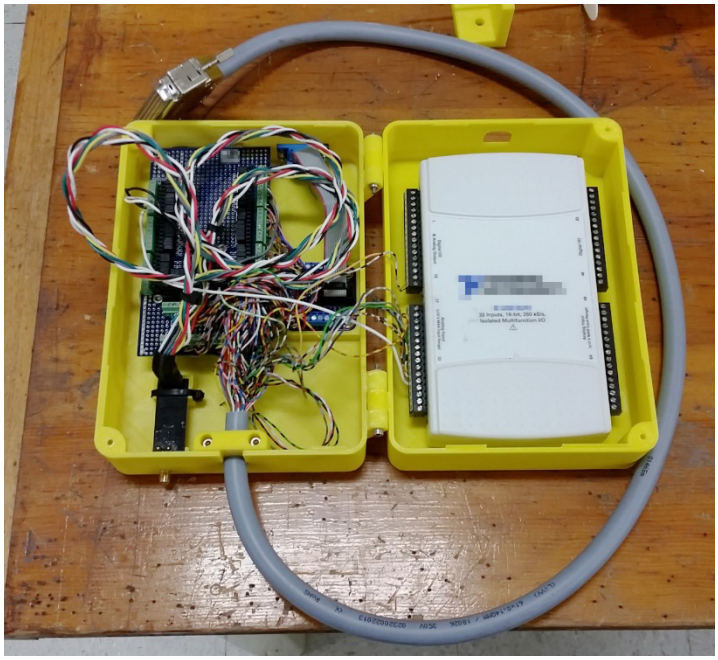

Source: FHWA.

Figure 5. Photo. The DAQ module and microcontroller that help control the cable robot and collect data.

With the clamps now working, the next step was to program the sequence of commands to perform climbing activities. The initial climbing tests began using a vertically mounted pipe, which simplified the task by eliminating side forces on the robot. Before the robot could climb, an important question had to be answered: How do you know that the ring platform is securely clamped? The original design of the robot called for the linear potentiometers to relay back the bracket head's position to the control unit, which would use this distance and the pipe's diameter to determine whether the ring's clamps were fully closed. However, a serious problem with this method was immediately encountered. The robot was designed to send the data signal from the potentiometer down the 15.24-m cable to the control unit and the DAQ module. However, the cable was unshielded, and interference from the pulse signal to the stepper motor created noise in the potentiometer's signal. Even with averaging, the position data would bounce and vary and thus not be a reliable method to accurately drive the clamp's stepper motor. Instead, a different approach was taken, in which a command was sent to drive the stepper motor, causing the clamp to close, and when the potentiometer's averaged data had stopped moving for a specified time, usually a few seconds, the clamps were assumed to be closed against the pipe. Using this method, the potentiometers did not require accurate calibration each time. The program simply had to recognize when the clamps stopped moving. The downside, however, was that without accurate positioning among all three clamps, there was no guarantee that the robot was centered on the pipe.

The second half of programming the climbing activity involved instituting the elevator motion. The elevator stepper motors receive a simple command to drive the ring platforms together or

apart. Therefore, monitoring data from the rotary encoders mounted on ring C provides the actual distance traveled. The encoders record the revolutions, to a fraction of a degree, which are then translated to height using a ratio provided from the instructions. As with the potentiometer, the encoder data sent to the DAQ module over the 15.24-m cable experienced interference from commands to the stepper motor, but unlike the potentiometer data, the signal was a digital pulse count that could still be read. Technically, the distance traveled could be measured by calculating the number of steps the motor performed, but an external force could jam the spindle and prevent the motor from turning. Therefore, the most accurate way to measure the distance was to count revolutions using the encoder. During this initial setup, the project team discovered that data from only one encoder could be measured successfully. As a result, the elevator algorithm was based on the data from that encoder and required visual inspection to ensure that both stepper motors were functioning in sync.

With algorithms for the clamping motion and elevator motion programmed, they were then structured in a loop to perform a climbing routine. The routine went as follows (starting with ring A and ring B fully clamped):

1. Ring A unclamp.
2. Elevator stepper motors move ring A away from ring B.
3. Ring A clamp.
4. Ring B unclamp.
5. Elevator stepper motors move ring B toward ring A.
6. Ring B clamp.

The most important rule was that, at any time, either ring A or ring B had to be fully clamped.

With this task completed, the next step was to program the laser carriage. Unlike the stepper motors that drive the elevator spindles, the stepper motor that controls the carriage does not experience much torque since it drives the lightweight carriage around the precision ring using the pinion and toothed gear ring. Therefore, no encoder was needed to check the distance traveled. The position was calculated by counting the steps taken by the stepper motor, which was then translated to a fraction of a degree using a formula in the instruction manual. Driving the carriage was therefore simpler than controlling either the clamp or elevator stepper motors. With limit switch sensors at either end of the laser ring, the carriage could be driven until it hit the sensor to reset the step count to zero, then reverse back around the ring, keeping track of each motor step to mark the corresponding degree.

At this point in development, a familiar issue reemerged. The robot was designed to take cable measurements with a set of dual laser-distance sensors, but the data traveling down the 15.24-m cable to the DAQ module from these laser sensors experienced interference from the stepper motor commands. This issue was known during the initial development of the robot. However, the proposed solution was to shut off power to the stepper motors, take a measurement, and then restore power to move the carriage a few steps before disengaging the power once again and taking the next measurement. This stop-gap solution has two major issues. The first is that this series of steps is extremely slow and inefficient. The second is that shutting off the power to the stepper motor removes any applied torque, so the pull of gravity could move the carriage if the robot was at an angle. An alternate solution was needed.

To solve the interference problem and transmit a clean data stream from the lasers, the team added a second microcontroller to the laser carriage. Not only could this microcontroller read the data from the laser sensors at a high sampling rate, but it could also broadcast the data directly to a wireless receiver attached to the microcontroller connected to the DAQ module. All issues with interference were eliminated by avoiding transmitting data over the 15.24-m cable, and the stepper motors could now run simultaneously with data collection, resulting in a much faster process. As mentioned earlier, the stepper motor for the carriage did not have an encoder, and the motor's position was known by counting the number of steps that the microcontroller sent to the motor. The microcontroller at the DAQ module would receive the wireless laser sensor data and sync it with the step count sent to the robot, resulting in some inherent but minimal delay (a fraction of a millisecond). The microcontroller then sent the combined angle and measurement data to LabVIEW for further analysis. The sample rate of the laser sensor was high enough that the signal could be averaged in LabVIEW to produce a smoother curve.

Now that programming had been successfully completed for both climbing activities and laser measurements, the team modified the test conditions to more accurately replicate field conditions. Until this point, the robot had still only been tested on a vertically mounted pipe, but in the field, that scenario would not be encountered. A test rig was built in the Aerodynamics Laboratory that could simulate a range of different field conditions, including an adjustable angle from horizontal and varying pipe diameter. The rig's base structure was constructed with aluminum T-slotted framing. A 2.87-m-long single profile aluminum frame was mounted upright on the lab wall at 1.38 m above the floor to support the upper end of rig. The lower end of the rig was supported by a 52.1-cm-long single profile aluminum frame bolted perpendicularly into a 50.8 cm by 40.6 cm by 2.54 cm iron plate. A 4.57-m-long double profile aluminum frame was mounted between the base and wall frames. The wall frame had four mounting positions, permitting a range of test angles from 11–56 degrees. Two sections of polyvinyl chloride (PVC) pipe, one 3.05-m long and the other 1.52-m long, rested on the double profile aluminum frame and were joined together by a standard 18.4-cm PVC pipe fitting. The PVC pipe had an outer diameter of 16.8 cm while the connector fitting had an outer diameter of 18.5 cm. Additionally, the lab had a collection of bigger HDPE pipe segments that could be mounted on the PVC pipe to test a wider range of diameters.

Using the new rig, the robot performed the first climbing tests at an angle, and a new problem was encountered. The robot was mounted so that it balanced via a single clamp, with the two remaining clamps on opposite sides on the bottom half of the pipe. When the robot climbed, one of the rings would unclamp, but the weight of half the robot would rest on that single clamp, so when the elevator motion started, the clamp would drag along the pipe. This behavior might be tolerable on a smooth test rig in the lab, but in real-world situations, the robot would likely need to maneuver over helical fillets on the HDPE pipe or welded joints. With the clamp dragging on the surface of the pipe, the possibility exists that the clamp could get bent, stuck, or otherwise damage the pipe. To solve this issue, the team decided that ring C needed support wheels that would allow the top clamp to fully retract from the surface of the pipe.

The first set of wheels tested were 5.1-cm-diameter rubber wheels on a metal bearing. A frame was created from aluminum T-slotted framing that bolted into utility holes predrilled into ring C, and the pair of wheels were mounted on either side of the top edge of the pipe. This configuration could successfully support the robot when the clamps on ring A were open, but

when ring A was closed and ring B was opened, the robot's weight distribution would rock back and cause the top clamp on ring B to drag. Wheels also had to be added to the bottom of the robot on ring C. The wheels themselves required upgrading as well, since the rubber on the wheels was getting squeezed off the metal bearing, and concerns arose regarding the ability of the wheels to roll over obstacles on the pipe. Those wheels were replaced by larger, sturdier 10.2-cm-diameter blue plastic wheels on metal bearings. The plastic was sturdier than the rubber and could not be removed from the bearing, plus the wheels' larger diameter allowed them to more easily roll over fillets and joints. In the new design, one wheel was mounted on the robot at the top of the pipe, and two wheels were mounted below the pipe at the location of the clamps on rings A and B. The top wheel was mounted in the middle of the clamp section, while the two bottom wheels were off-center, putting their contact point closer to the centerline of the pipe. Figure 6 shows the cable robot with the new wheel configuration mounted on the test rig in the lab.

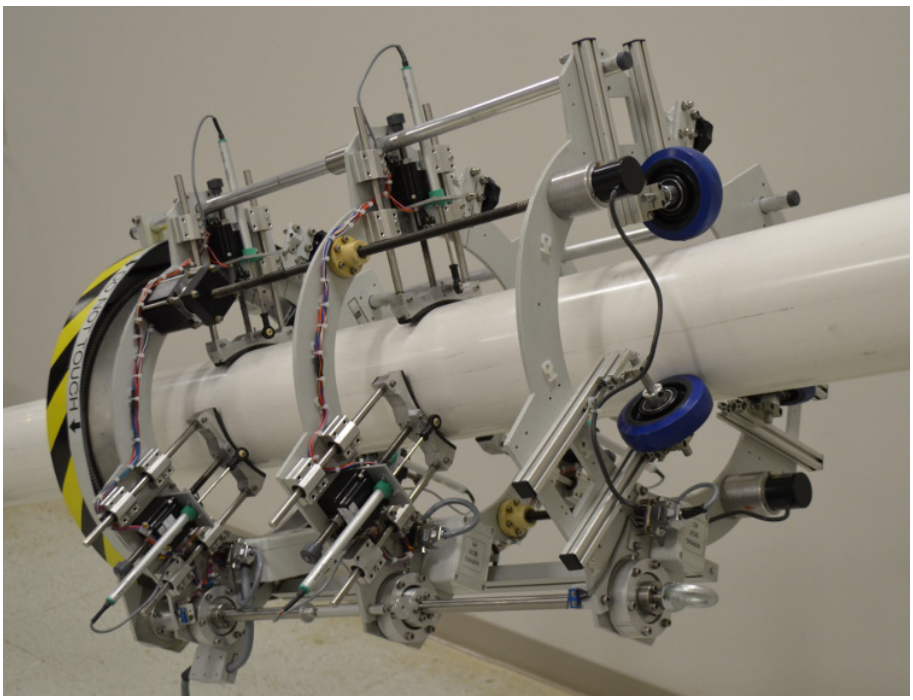

Source: FHWA.

Figure 6. The cable robot mounted on the test rig.

The new wheel configuration on ring C could successfully support the robot's weight, but only when ring A and ring C were not positioned too close together during climbing activities. The clamps on the opened ring no longer dragged on the surface of the cable, and the wheels helped smoothly roll the robot up the cable during the elevator motion. The clamps' algorithm was modified to improve the clamps' ability to keep the robot centered on the pipe. Instead of all three clamps on the ring closing simultaneously, now the bottom clamps would close first and then the top clamp would close, securing the ring on the pipe. However, if the lower clamps weren't perfectly synced, the robot tended to go off axis. Therefore, the clamping order was reversed so that the top clamp would close first to a specific position to center the robot on the pipe, then the bottom two clamps would close simultaneously to secure the rings on the cable.

This prevented the robot's tendency to drift off-center from the axis but introduced a new problem: The robot should never rotate on its axis and must remain centered on the top clamp.

To keep the robot centered on the top clamp, the team first decided to lower the robot's center of gravity by adding more weight, thus forcing the robot to realign while it climbed. Unfortunately, adding more weight to the robot wasn't ideal, and preliminary tests on the rig failed. The next method involved bolting 91.44-cm-long aluminum T-slotted framing members to ring C to act as balancing arms or outriggers. Straps hung from these outriggers, and the operator used the straps to manually steer the robot back to center (on course). This solution was not the most technologically advanced design, but with a tight deadline approaching for field testing, the team decided that it was the easiest solution to implement, and more importantly, it worked well.

CHAPTER 3. LASER MEASUREMENTS AND DATA ANALYSIS

LASER CALIBRATION

The robot used a pair of laser distance sensors to measure the cables' surface. These sensors were chosen because they were small enough to mount on the carriage but accurate enough to return measurements with a resolution of 10 μm. The sensors work by projecting a laser beam onto a surface, with the distance calculated by measuring the difference in angle at which the reflection returns. The sensors have an output of 0–10 V and are programmed to return an accuracy of 0.1 mV, which LabVIEW converted to a 5-digit integer. Before these integers could be converted to distances, they had to be calibrated by lab staff, which ended up being an ongoing process for the robot's functioning.

The instructions for the robot stated that a laser output of 0.4 V was equivalent to 17 mm while an output of 10 V was equivalent to 117 mm. The instruction manual also stated that the precision ring had an inner radius of 167 mm. From this information, the first programs were designed in LabVIEW to provide real-time graphical feedback and visualize the shapes the robot was scanning. One of the first tests was measuring a piece of sample pipe with a pencil taped to the outer wall. This simple test allowed the lab staff to adjust and align the plots from the two lasers and get an initial feel for how the measured data would appear.

The team quickly discovered that the calibration values provided in the instruction manual were based solely from values from the lasers' datasheets and were not as accurate as possible. Therefore, lab staff designed and 3D-printed a special plastic calibration tool. The tool mounted to the bottom of each laser sensor and had two targets at different distances. From these two measurements, the team could use a simple linear equation to convert the voltage into distance. This step was a good start to complete the initial calibration, but there were two drawbacks: The accuracy of the measurement was limited by the accuracy of the 3D printer, and the measurement was static. In actual field measurements, the laser would move around the ring, which this tool did not consider.

Another significant issue was that the laser sensors' carriage mount was adjustable, and great effort was made to ensure that both lasers aimed at the robot's center line. However, this work was all done by hand, which meant the procedure would have limited accuracy. By simply tightening a screw that fastened the laser sensor to the carriage one could alter the sensor's direction by a fraction of a millimeter.

With the lasers calibrated using the special tool, the first measurements were taken on a sturdy piece of white PVC pipe that could stand upright, with an anchor at the bottom for additional stability. Initial measurements were taken for both clockwise (CW) and counterclockwise (CCW) directions and at various levels of resolution. At this point in time, low resolution was defined as one measurement per degree, while high resolution was one measurement every quarter of a degree. From these initial measurements, the first postprocessing programs were developed in MATLAB® to perform additional calculations, including filling gaps in the data, centering the measurements, and producing output graphics such as "heatmap" plots that could easily illustrate a varying pipe radius.[18]

To help improve the quality of the measurements, the TFHRC's machine shop smoothed a pipe on a lathe to be perfectly round within a fraction of a millimeter. With this newly smoothed pipe, the team could fine-tune both LabVIEW and MATLAB programs to more precisely analyze the data and improve the algorithms. Another issue preventing accurate measurements was uncertainty whether both lasers pointed to the exact center line of the robot. To assist in this alignment, lab staff clamped a thin straw at the robot's center, with the goal of keeping the red laser points reflected on the straw for an entire revolution. After a few attempts, this test was successful, and it was determined that this level of accuracy would suffice and that building a precise calibration rig was not required.

After laser centering was completed, additional scans of the white pipe were collected and compared to those taken before the adjustment. Afterward, three more samples of HDPE cable segments from various bridge sites arrived at the lab and were also scanned and analyzed. These pipe segments were not used for calibration but rather to verify that the analysis software could successfully process a variety of cable sizes and shapes.

Numerous scans of the smoothed pipe were processed under different conditions, including slight rotations of the pipe or clamped versus unclamped. Although the measurements were accurate and repeatable within a millimeter, an underlying pattern to the radius plots kept appearing in the measurements. This pattern implied that, perhaps, the laser sensors were not moving perfectly smoothly as they traveled around the precision ring. To test this theory, the lasers were shut off and a small aluminum T-slotted frame was attached to the carriage extending to the robot's center line. At the end of the frame, a triple-axis accelerometer was mounted to trace the movements of the carriage as it circled around the precision ring. The first test was performed with the robot standing flat on the floor, then two tests followed with the robot leaning at different angles, and finally a test with the robot on the floor but rotated 180 degrees from the original test. When the data obtained was translated to a global coordinate system, the results confirmed what had been suspected: The carriage was not rolling perfectly on the precision ring but rather was bobbing vertically up and down and slightly left to right. The same pattern, however, repeated during each test run, so there was hope that the measurement errors were consistent and could theoretically be subtracted out. The patterns from the accelerometer seemed to match patterns found repeatedly in the laser measurements themselves, which also was encouraging.

While attempting to determine exactly how to measure the tiny deflections in the precision ring, there was also growing concern that the instruction manual's claim of exactly 167 mm for the robot's inner ring radius was not entirely accurate. Although the pipe had been smoothed on the lathe, its precise diameter was unknown. Therefore, an alternate test was proposed to measure a noncircular object at various positions and use optimization techniques to verify the exact ring radius and each laser's linear equation variables. An aluminum block was machined to be exactly 7-inches long with each end 90 degrees perpendicular to the edge. The block was then placed in eight different positions within the ring, and a scan was taken for each position. Results from these experiments were processed in MATLAB, where a script converted the laser measurements to Cartesian coordinates and then calculated a best fit line for each edge of the block. Using these best fit lines, the script then calculated the distance between edges and compared it to the block's known length of 17.78 cm and compared the angle between the best fit lines to 90 degrees. A matrix of values was computed to evaluate which set most closely fit these requirements across

all block positions. Unfortunately, the test proved to be inconclusive. No set of values fit best across all block positions. It was speculated that without canceling out the imperfections in the precision ring, the measurements could not be assumed accurate.

Since the same pattern appeared repeatedly in the data, it was decided that the best way to deal with the issue would be to simply subtract the pattern when calculating the laser's distance. Therefore, using the smoothed pipe, seven different measurements were taken and centered, and the results for each laser were averaged and the first "zero ring" was calculated. A simple graphical user interface (GUI) created in MATLAB allowed the researchers to smooth out the curve by hand. The zero ring was saved and applied to the datasets and brought the variability of the measurements within half a millimeter.

This idea was taken a step further with a set of plastic discs that were machined on the lathe to produce perfectly smooth diameters. The three plastic discs had diameters of 102, 154, and 200 mm respectively and are shown in figure 7. A stand was built using a heavy iron weight from which an aluminum bar was mounted. The discs could be easily swapped from the bar without displacing the stand. For each disc, five measurements were taken, each time rotating the disc a short turn. Since the same pattern appeared despite each disc's rotations, for the first time there was obvious visual evidence that the patterns appearing in the measurement plots were due to the carriage and the precision ring and not the pipe itself. That the lasers were not returning data on a perfectly linear scale also became clear. Variables used to convert the laser signal, which were accurate for the 200-mm disc, would not produce the correct radius for the 102-mm disc, and vice versa. Fortunately, most cable diameters in the field are closer to the 200-mm disc; with the lasers calibrated for that distance the results were assumed to be accurate.

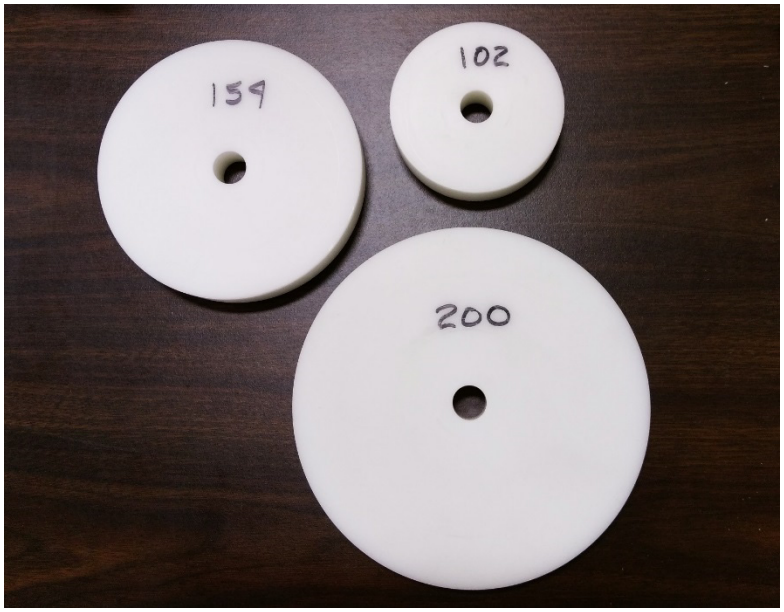

Source: FHWA.

Figure 7. Photo. The three calibration discs.

The average curve of all five measurements for the 200-mm disc and the average curve of all five measurements of the 154-mm disc were themselves averaged at a ratio of 3:1 in favor of the

200-mm disc. This curve was then smoothed using the MATLAB GUI, and the new zero ring was saved. By applying this averaged zero ring to the disc data, the difference in variability was less than 0.5 mm. This level of accuracy was deemed acceptable.

CONTROL SOFTWARE

Lab staff developed a simple program in LabVIEW that served three main purposes. First, the program could control all aspects of the robot and receive feedback simultaneously and using this information could run the robot using automated loops. Secondly, it could receive all laser measurements, pair them with the corresponding angle of the carriage, and save that data to a file. And finally, it had a GUI that provided real-time feedback using plots and other methods to relay to the field user the status of the robot and its latest measurements.

CABLE CENTERING ALGORITHM

As mentioned previously in this report, due to interference along the unshielded 15.24-m cable, the linear potentiometers were rendered of limited usefulness in the early versions of the robot. Instead of knowing the precise location of each clamp's bracket head, the control unit drove the clamps until they stopped moving against the pipe, and the potentiometer could only relay when the clamp stopped moving. Without assurance of accurate positioning of the clamps, it would not be known if the robot had been centered perfectly on the cable when taking measurements. Therefore, an algorithm was developed to center each measurement automatically in postprocessing so that the robot's position while climbing the cable would be irrelevant.

Several reasons exist for centering the measurement. Although the shape of the cable can be recreated by simply taking the positioning of the laser carriage in degrees and the distance measurement, the minimum and maximum radius cannot be calculated without centering the cable. The minimum and maximum radius were needed to determine the out-of-roundness for each shape. Additionally, comparing measurements taken at various locations along the cable becomes difficult if no common reference point exists among the laser scans.

The centering algorithm required three main assumptions to be true: the outer ring was perfectly round, the laser pointed perpendicular to the ring, and the measurements were taken at regular intervals as the laser moved around the ring. Unfortunately, neither of the first two assumptions were 100 percent true, but both were close enough that the algorithm still worked.

If the cable is off-center in the robot, the laser will take a lower density of measurements on the surface as it passes close to the cable while the measurements will be more concentrated on the opposite side. Since the density of data points is unbalanced around the surface of the cable, the center of gravity of all points is weighted closer to the denser concentration of measurements.

If the polar measurements are translated to Cartesian coordinates, the distance between each point can be determined. Normalizing those distances by summing them and dividing by their mean provides a multiplication factor. Taking this normalized multiplication factor and applying it to every X and Y coordinate creates a set of weighted coordinates that balance out the density. The mean of these weighted coordinates is the true center of the pipe.

The preceding steps are the equivalent to assuming the pipe has a constant wall thickness, finding the length of each mass segment between coordinates, then finding the center of mass by adding up all the mass segments multiplied by their position and dividing by the total mass.

The algorithm was tested with two sets of dummy data mimicking both a perfect circle and an oval. The algorithm successfully centered both shapes. However, there was one caveat. A fourth and previously unmentioned assumption is that the robot is aligned parallel with the cable. If that is not the case, then it will be impossible to tell in postprocessing if the cable is not round or if it is misaligned. Fortunately, with the adapted climbing algorithms, maintaining a parallel alignment wasn't much of an issue.

DATA POSTPROCESSING

Postprocessing of the data was performed in MATLAB using a specially designed GUI. The preprocessed data contained metadata including date, time, bridge name, sample rate, and the distance up the cable, and the measured data including the laser measurements and angular position data for each laser. MATLAB imported this data and then displayed it on two plots, with the first plot being angle versus radius and the second plot the cable shape plotted in Cartesian coordinates. Data from each laser could be analyzed individually or simultaneously.

Once the data was initially loaded and the zero ring applied, the first step was to fill in the data gap located near the hinge of the precision ring where the carriage is blocked by the limit switches. The actual measurement arc of the robot is around 327 degrees, which leaves a 33-degree gap, although the ranges of lasers 1 and 2 were offset to ensure at least one measurement for most of the gap. The radius curve was plotted twice, once from −360 to 0 degrees and again from 0 to 360 degrees with the 33-degree gap appearing around 0 degrees. Using the polyfit function, an algorithm filled in the gap using polynomial curve fitting. The default curve was a fifth-order polynomial that overlapped the data by 12 percent, although the order of the curve and the overlap could be adjusted. Code was later added to the algorithm to partially ignore data during the curve fit, like a bump from a helical fillet. Once the fit was determined to match the pattern of the radius, the gap was filled using the generated data.

The next step was to remove any invalid data that was part of the curve. The biggest source of invalid data was bright sunlight shining onto the cable, which caused errors with the laser sensors. Additionally, any sort of nonpermanent obstacle like an insect or loose piece of tape that wasn't part of the cable shape could be removed. The process for removing the invalid data was similar to the process of filling in the gap, using a polynomial curve to replace the measurements between two selected data points.

The last step before centering was removal of the helical fillets. This process was similar to replacing the invalid data or filling in the gap with the polynomial curve, but the fillet data was saved in a separate dataset to be accessed later for plotting and visualization purposes. However, removing the fillets was required for the centering algorithm to work, to determine the maximum and minimum radii, and to calculate the out-of-roundness.

With the gap filled and fillets removed, the centering algorithm could then calculate the true center point of the pipe and shift to the new center. Both plots in the GUI were updated to show

the new angle versus radius plot and the shifted pipe in Cartesian coordinates. Text boxes displayed the maximum and minimum radii for each laser, as well as the x and y shifts in mm. The data for each measurement, the distance the measurement was taken up the cable, and other metadata, including date, time, bridge name, and cable name, were saved as a MATLAB data file.

Additional MATLAB scripts were created to summarize the data in tabular form and save plots that helped visualize the roundness of the cable shapes.

CHAPTER 4. CHESAPEAKE AND DELAWARE CANAL BRIDGE TESTING

FIELD TESTS

The first field tests of the cable roundness robot were performed in April and June 2015 on cables at the Chesapeake and Delaware (C&D) Canal Bridge, officially known as the Senator William V. Roth, Jr. Bridge, located in St. Georges, DE. This elevated cable-stayed bridge with a 228.6-m main span and 137.2-m side spans carries Delaware Route 1 over the C&D Canal. This bridge was optimal for initial tests because of its proximity to the TFHRC and for having cable stays located in the center of the bridge deck, protected from traffic by two concrete barriers. The bridge has two 98.2-m-tall pylon towers, with 16 parallel cables in each fan on both sides of each tower supporting the deck. A photo of the bridge is shown in figure 8.

Source: FHWA.

Figure 8. Photo. The C&D Canal Bridge.

Unlike most cable-stayed bridges in the United States, the stays on this bridge are sheathed in steel pipe instead of the typical HDPE pipe. This steel pipe is painted yellow and has an unusually rough texture as well as a few rusty areas, particularly at connections. Figure 9 and figure 10 show examples of the surface texture and rust.

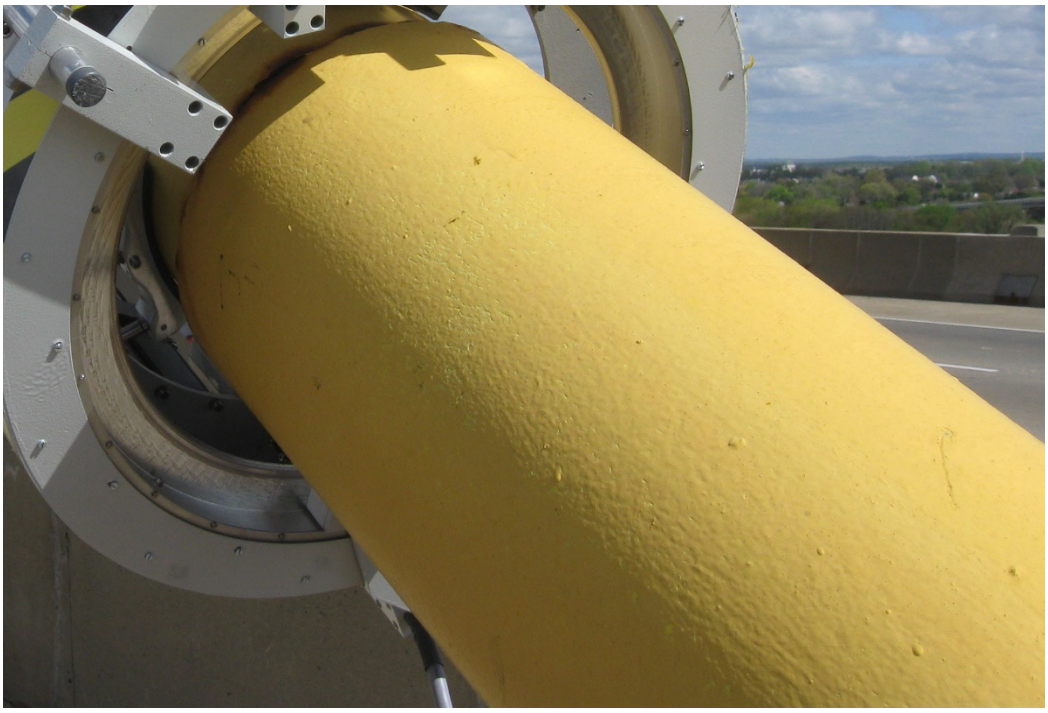

Source: FHWA.

Figure 9. Photo. Surface texture of steel pipe sheathing stay cable.

Source: FHWA.

Figure 10. Photo. Rust near a connection in steel pipe.

The initial field testing was performed on April 28, 2015, on cable South S1, the shortest cable closest to the south tower. The test was a success; the robot managed to climb 5.1 m up the cable, taking 19 measurements on the way up and back down. A few months later, the robot returned to the site and measured three additional cables. Photos of the cable robot climbing and taking

measurements at the C&D Canal Bridge are shown in figure 11 and figure 12. Figure 13 shows the laptop and control unit setup at the base of the bridge. A summary of the testing is listed in table 1.

Source: FHWA.

Figure 11. Photo. The cable robot mounted on a cable at the C&D Canal Bridge.

Source: FHWA.

Figure 12. Photo. The cable robot climbing up cable South S1.

Source: FHWA.

Figure 13. Photo. The laptop, DAQ module, and control unit.

Table 1. Summary of C&D Canal Bridge testing.

Date	Cable	No. of Measurements	Maximum Distance (mm)
4/28/2015	South S1	19	5,097
6/10/2015	South S13	8	3,516
6/10/2015	South S14	11	5,133
6/9/2015	South S15	17	6,201

ANALYSIS AND RESULTS

Data from testing was processed using the custom software described in chapter 3. The gaps in the data surrounding the hinge were filled in using polynomial curve fitting, the data was centered, and the mean (r_{mean}), maximum (r_{max}), and minimum (r_{min}) radii were calculated for each laser. The resulting data was saved in multiple data file formats.

An out-of-roundness percentage was calculated for each cable scan by taking the difference between the maximum and minimum radii and dividing it by the mean radius, shown in equation 1. Table 2 contains a summary of the results from field testing where the mean, maximum, and minimum radii are averaged from all scans for each cable measured.

$$\text{Out-of-roundness} = \frac{r_{max} - r_{min}}{r_{mean}} \quad (1)$$

Table 2. Averaged cable radius data from laser 2 for the C&D Canal Bridge.

Cable	No. of Measurements	Maximum Distance (m)	Mean Radius (mm)	Maximum Radius (mm)	Minimum Radius (mm)	Out-of-Roundness (percent)
South S1	10	5.1	123.32	123.96	122.71	1.0
South S13	7	3.5	123.55	124.09	123.09	0.8
South S14	11	5.1	123.52	124.05	123.06	0.8
South S15	11	6.2	123.38	123.95	122.72	1.0

The first measurement from cable South S1 features the biggest variability in the radius, but this event also marked the first cable ever measured using the robot, whose laser accuracy was subsequently improved. The remaining three cables all featured an out-of-roundness under 1 percent, with a difference between maximum and minimum of about 1 mm, indicating that these steel cables were relatively round.

Visualization plots were produced that overlaid all the cross-sectional scans from an individual cable to help identify the cable's general shape and compare how that shape varied along the cable. The cross sections were normalized by the cable's mean diameter, and then the deviation from zero was shown by percentage. The plots were exaggerated by factors of 10 or 15 to make slight deviations more visible. Figure 14 through figure 17 contain the visualization plots for the four cables tested at C&D Canal. A note contains the range of distances up the cable where the scans were taken, measured either from the anchorage or the end of a guide pipe. The cable diameter is shown as *D*.

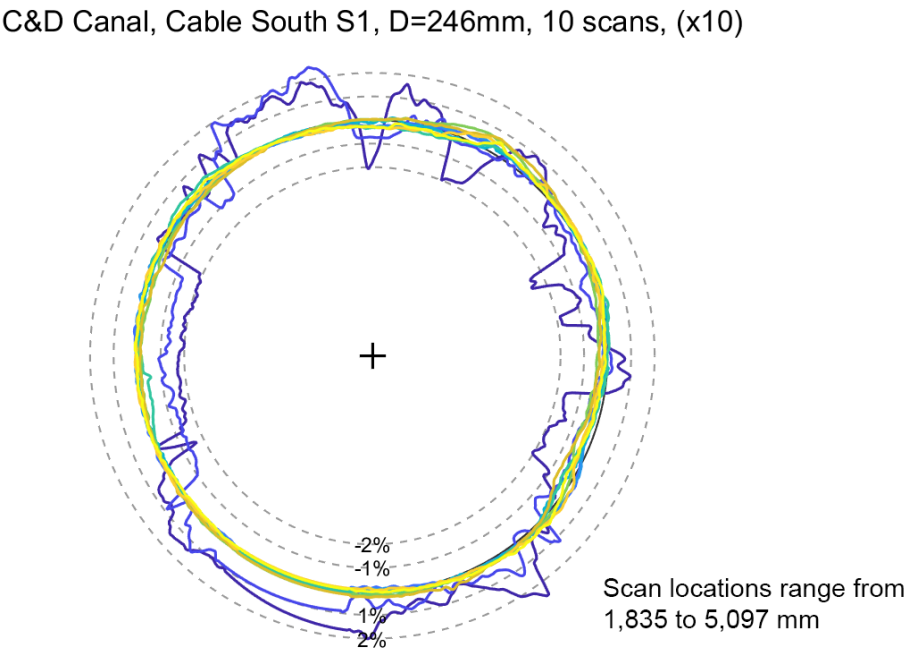

Source: FHWA.

Figure 14. Graph. Percent deviation from the mean plot for South S1 cable on the C&D Canal Bridge.

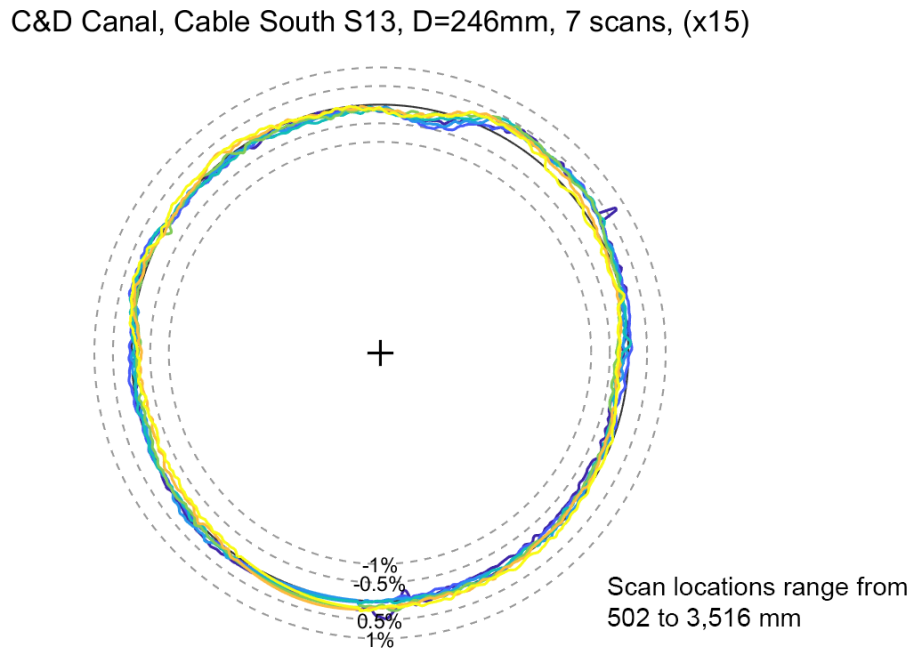

Source: FHWA.

Figure 15. Graph. Percent deviation from the mean plot for South S13 cable on the C&D Canal Bridge.

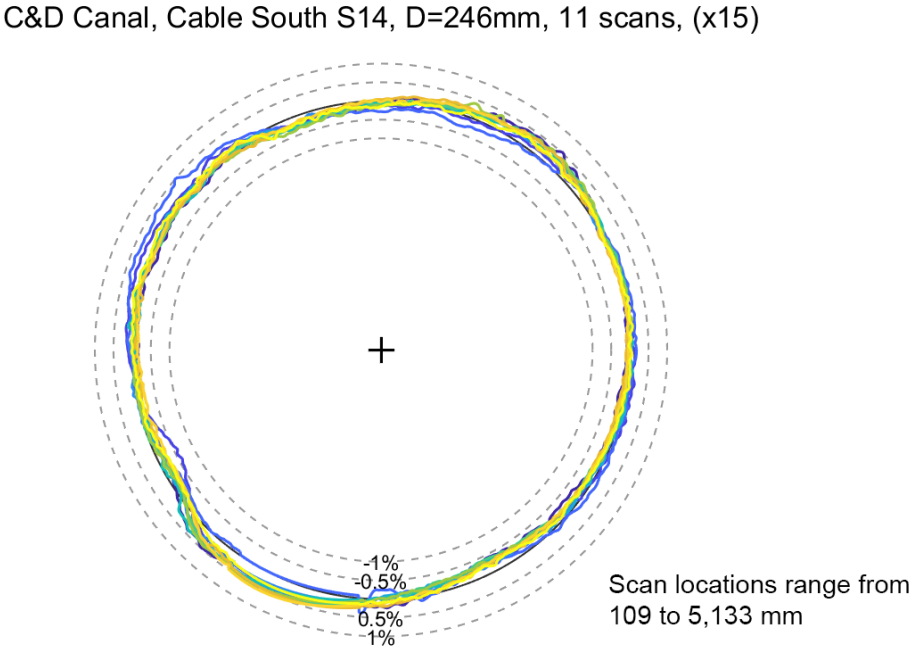

Source: FHWA.

Figure 16. Graph. Percent deviation from the mean plot for South S14 cable on the C&D Canal Bridge.

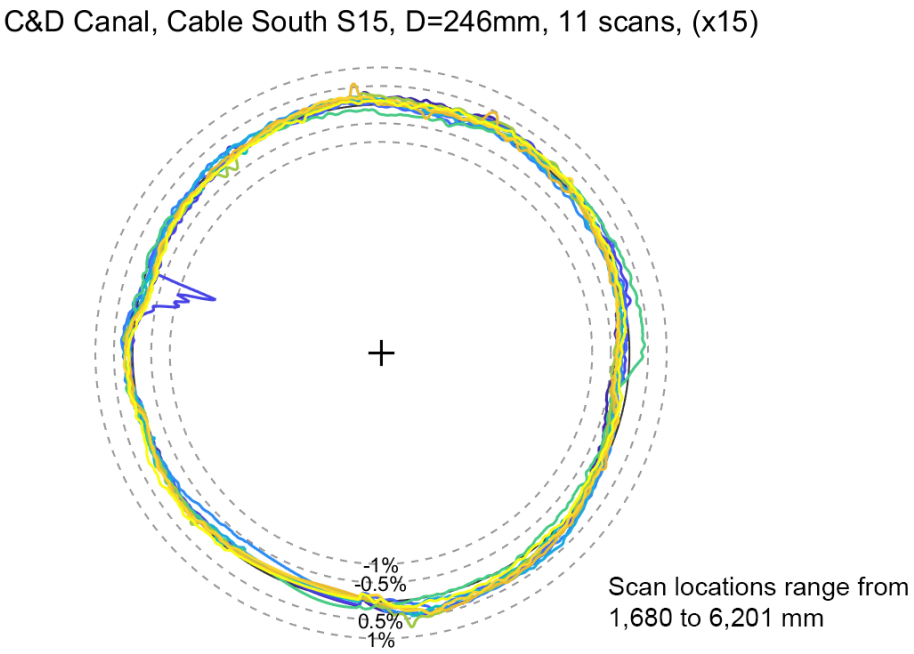

Source: FHWA.

Figure 17. Graph. Percent deviation from the mean plot for South S15 cable on the C&D Canal Bridge.

For the first cable tested, South S1, the first few measurements on the pipe contain a lot of random noise and general randomness, but that noise dissipates further up the cable. Note that this cable was the first measured in the field and that the accuracy improved in future tests. However, this noise and randomness might also have been caused by measurements of a rusty connector on the pipe.

The visualization plots for all four cables show that these cables, with an out-of-roundness below 1 percent, were extremely round in general shape, which supports the results from table 2. Very rarely did the radius exceed the 0.5 percent threshold, likely the result of these cables being sheathed with steel pipes and not HDPE pipes. While convenient for the first round of testing, these cables did not produce interesting shapes worth studying further.

CHAPTER 5. INDIAN RIVER BRIDGE TESTING

FIELD TESTS

The second bridge tested by the cable roundness robot was the Indian River Inlet Bridge, officially known as the Charles W. Cullen Bridge, located near Rehoboth Beach, DE. This cable-stayed bridge has four pylon towers in pairs on opposite sides of the bridge deck, with each tower supporting 38 cables in their fans. The main span of the bridge is 289.6 m long and carries Delaware Route 1 across the Indian River Inlet, which connects the Atlantic Ocean to the Indian River Bay. Although the cables are anchored at the edges of the bridge deck, this bridge was optimal for early testing due to a 3.66-m protected sidewalk located next to the stay cables on the east side of the bridge deck. A photo of the bridge is shown in figure 18.

Source: FHWA.

Figure 18. Photo. The Indian River Inlet Bridge.

Testing was performed in June 2015 in two phases. The first phase was one day following the initial testing at the C&D Canal Bridge, and the second phase was a week later and lasted four days. The robot measured seven cables and reached the furthest distance up any cable to this point, climbing nearly 13 m. In May 2016, the robot was returned to the site to test two more cables. During the setup and cable testing at this bridge, the team noticed that the surface of the HDPE pipe contained longitudinal grooves (see figure 19), probably resulting from the extrusion process. Photos of the cable robot mounted and climbing cables are shown in figure 20 and figure 21. A summary of the testing is listed in table 3.

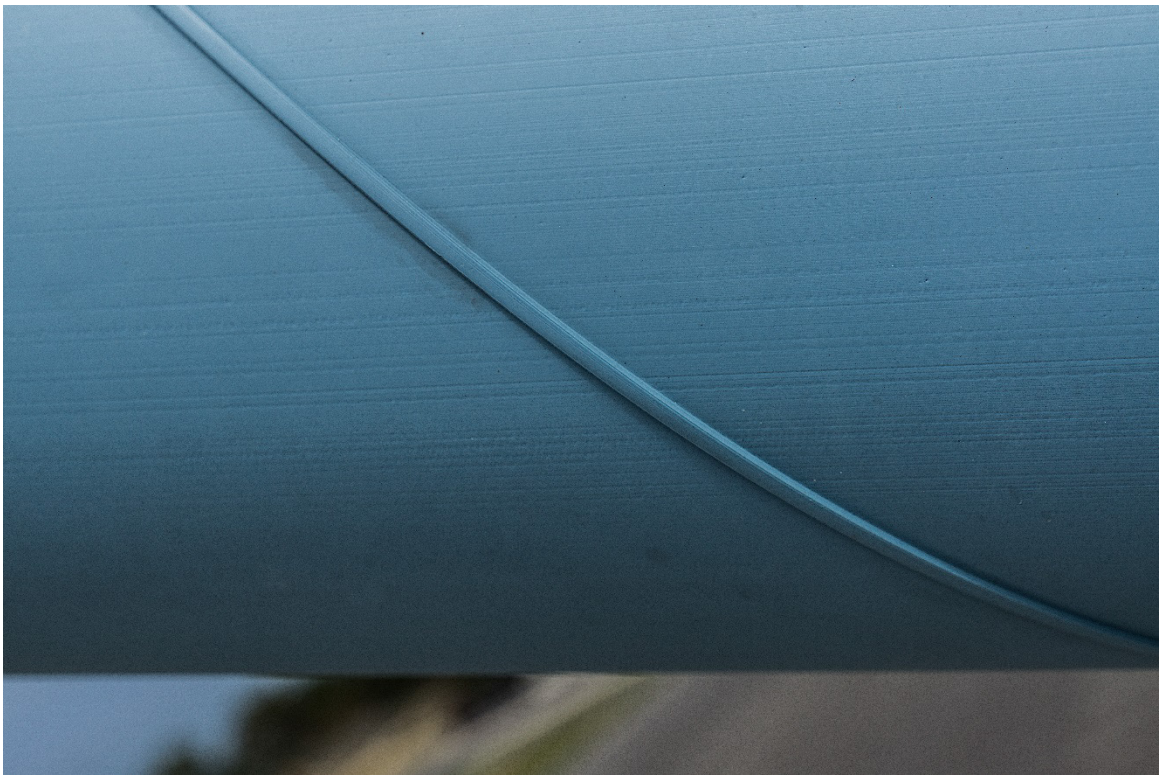

Source: FHWA.

Figure 19. Photo. HDPE pipe with helical fillet and longitudinal grooves in the surface.

Source: FHWA.

Figure 20. Photo. The cable robot mounted on a cable at the Indian River Inlet Bridge.

Source: FHWA.

Figure 21. Photo. The cable robot climbing a cable with the Indian River Inlet Bridge in the background.

Table 3. Summary of Indian River Bridge testing.

Date	Cable	No. of Measurements	Maximum Distance (mm)
5/12/2016	111E	22	10,463
6/19/2015	112E	10	5,139
6/19/2015	113E	14	6,292
6/17/2015	114E	10	5,779
6/17/2015	115E	29	12,979
5/12/2016	116E	15	7,130
6/16/2015	117E	16	1,260
6/18/2015	118E	16	8,296
6/11/2015	119E	21	8,188

ANALYSIS AND RESULTS

Data from testing was processed using the custom software described in chapter 3. The gaps in the data surrounding the hinge were filled in using polynomial curve fitting, the data was centered, and the mean, maximum, and minimum radii were calculated for each laser. The resulting data was saved in multiple data file formats.

The out-of-roundness percentage was calculated for each cable scan using equation 1. Table 4 contains a summary of the results from field testing where the mean, maximum, and minimum radii are averaged from all scans for each cable measured.

Table 4. Averaged cable radius data from laser 2 for the Indian River Bridge.

Cable	No. of Measurements	Maximum Distance (m)	Mean Radius (mm)	Maximum Radius (mm)	Minimum Radius (mm)	Out-of-Roundness (percent)
111E	21	10.5	85.79	86.35	85.28	1.2
112E	9	5.1	75.04	75.73	74.37	1.8
113E	12	6.3	85.51	87.03	83.98	3.6
114E	9	5.8	85.53	86.56	84.26	2.7
115E	24	13.0	85.53	86.63	84.34	2.7
116E	14	7.1	85.98	86.80	85.19	1.9
117E	15	8.5	96.01	97.84	94.26	3.7
118E	15	8.3	95.74	98.29	93.35	5.2
119E	17	8.2	96.07	97.47	94.43	3.2

The out-of-roundness for the cables tested for the Indian River Bridge varied between 1.2–5.2 percent with most of those cables falling in the range between 1.8–3.2 percent. But three of those cables, 113E, 117E, and 118E, had higher out-of-roundness values. For this bridge, the diameters of the cables varied based on their length and the number of steel strands in the cable, and three different diameters were tested: 151, 172, and 192 mm. Three of the top four highest out-of-roundness measurements came from the largest cable diameter tested, suggesting that the bigger cables were more likely to have larger eccentricities.

Visualization plots were produced that overlaid all the cross-sectional scans from an individual cable to help identify the cable's general shape and compare how that shape varied along the cable. The cross sections were normalized by the cable's mean diameter and then the deviation from zero was shown by percentage. The plots were exaggerated by factors of 10 to 15 to make slight deviations more visible. Figure 22 through figure 30 contain the visualization plots for the nine cables tested at Indian River. A note contains the range of distances up the cable where the scans were taken, measured either from the anchorage or the end of a guide pipe.

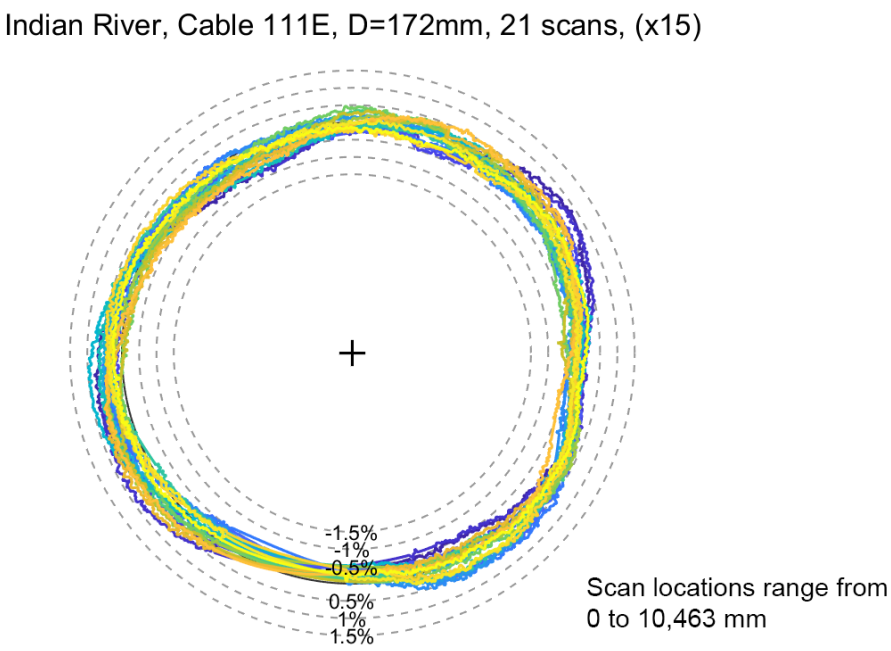

Source: FHWA.

Figure 22. Graph. Percent deviation from the mean plot for cable 111E on the Indian River Bridge.

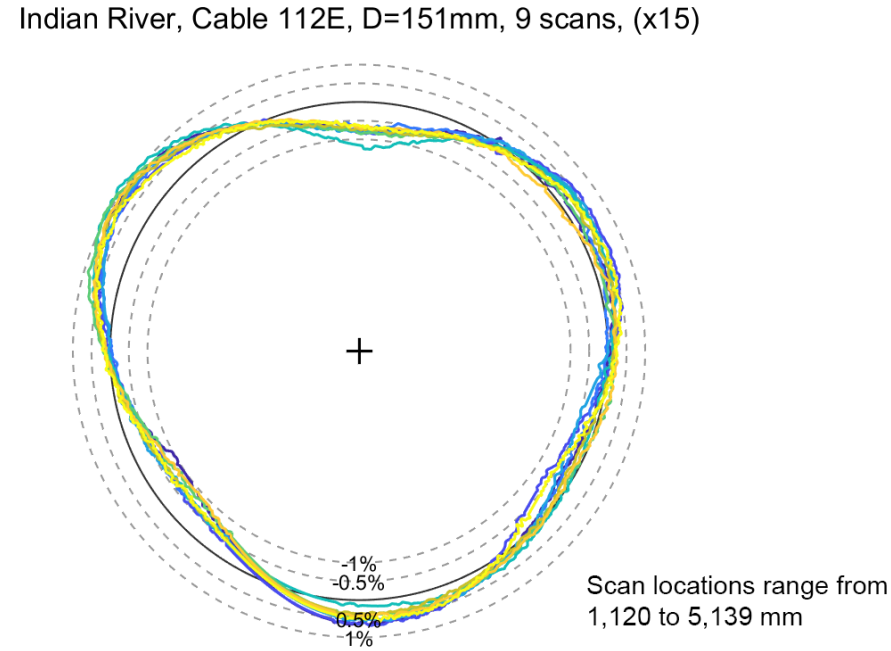

Source: FHWA.

Figure 23. Graph. Percent deviation from the mean plot for cable 112E on the Indian River Bridge.

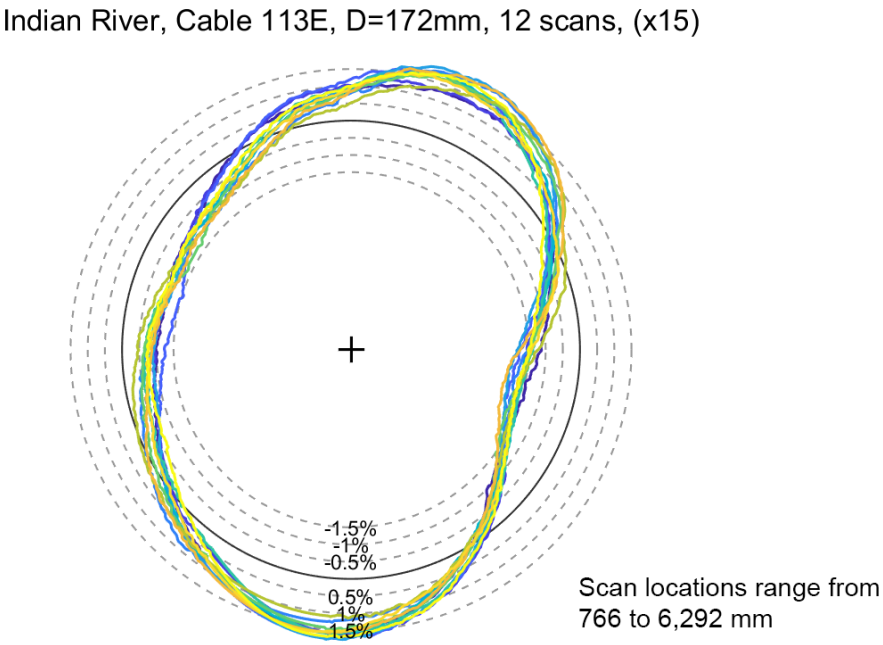

Source: FHWA.

Figure 24. Graph. Percent deviation from the mean plot for cable 113E on the Indian River Bridge.

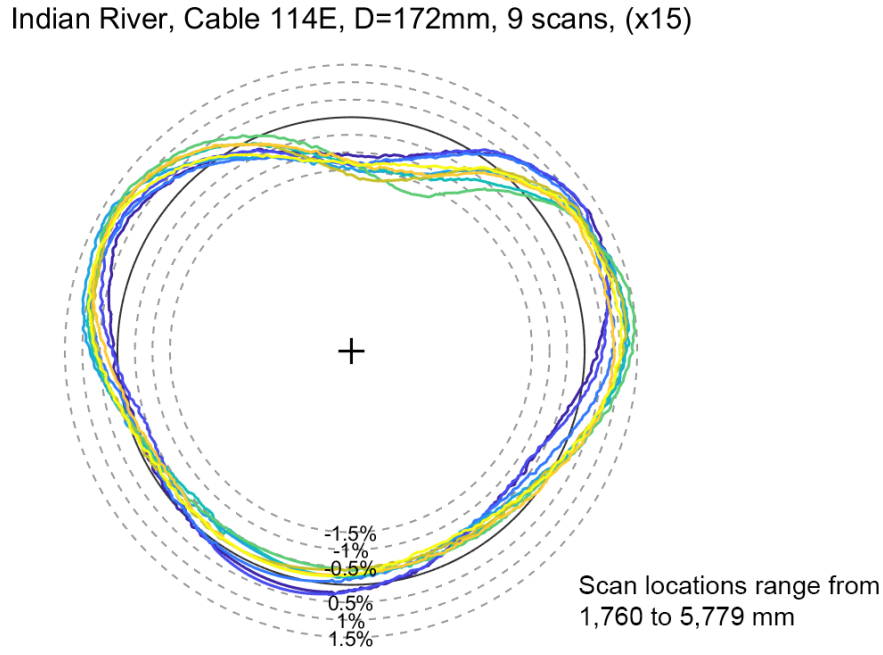

Source: FHWA.

Figure 25. Graph. Percent deviation from the mean plot for cable 114E on the Indian River Bridge.

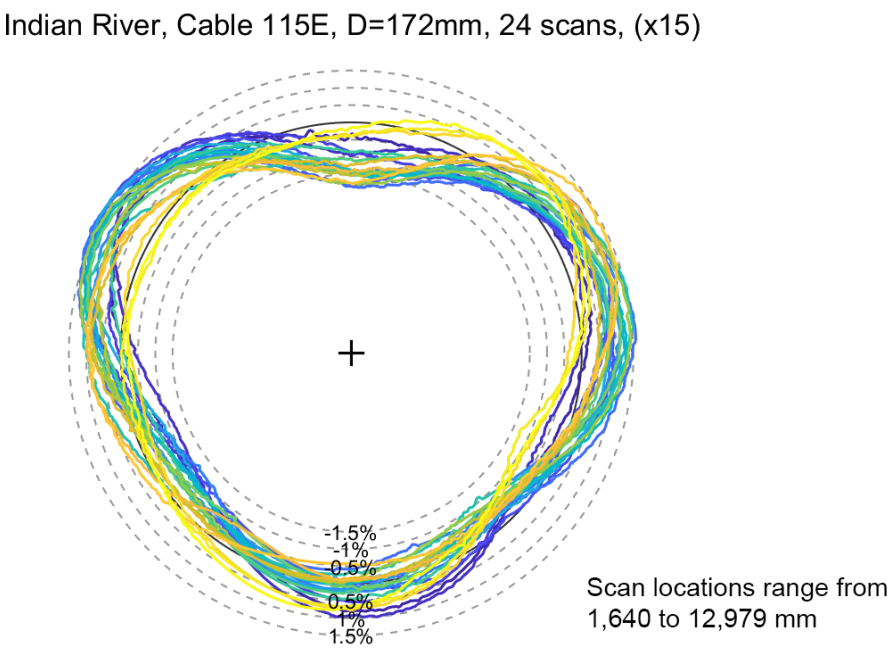

Source: FHWA.

Figure 26. Graph. Percent deviation from the mean plot for cable 115E on the Indian River Bridge.

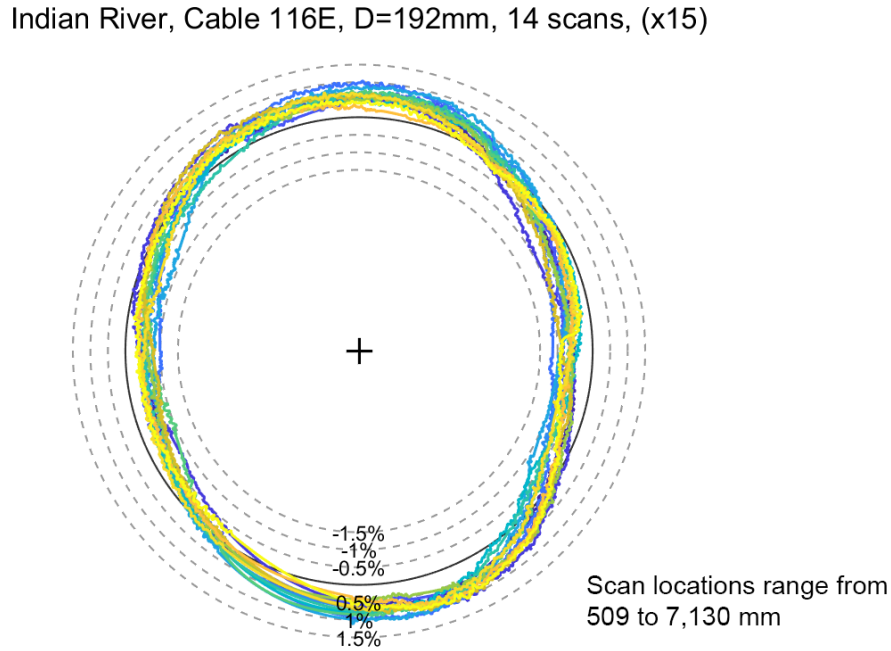

Source: FHWA.

Figure 27. Graph. Percent deviation from the mean plot for cable 116E on the Indian River Bridge.

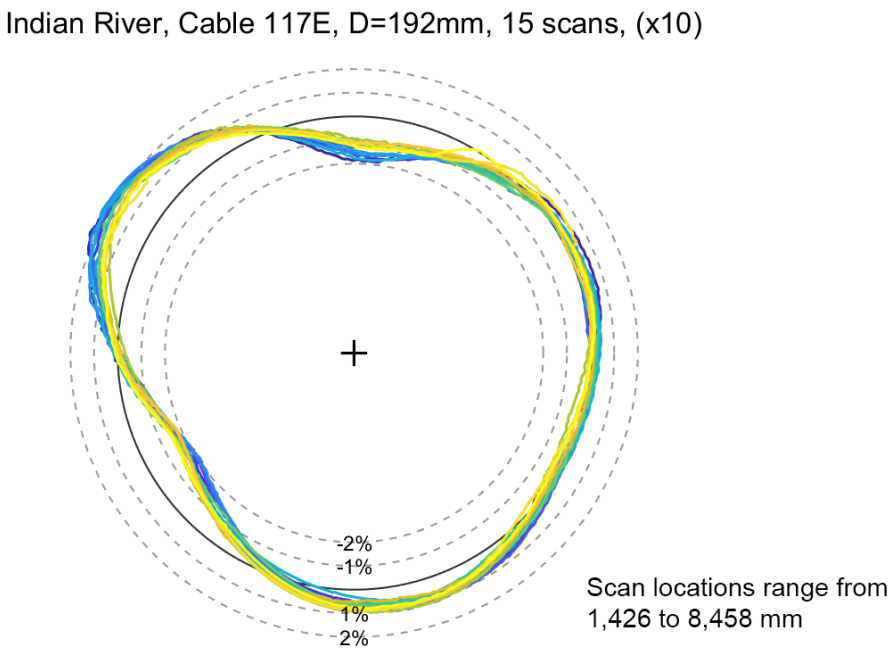

Source: FHWA.

Figure 28. Graph. Percent deviation from the mean plot for cable 117E on the Indian River Bridge.

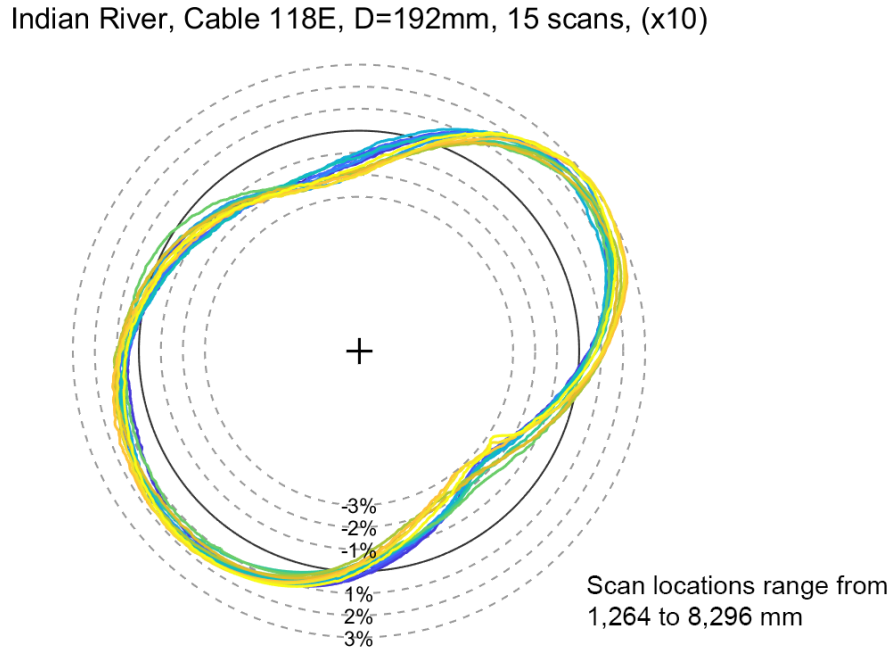

Source: FHWA.

Figure 29. Graph. Percent deviation from the mean plot for cable 118E on the Indian River Bridge.

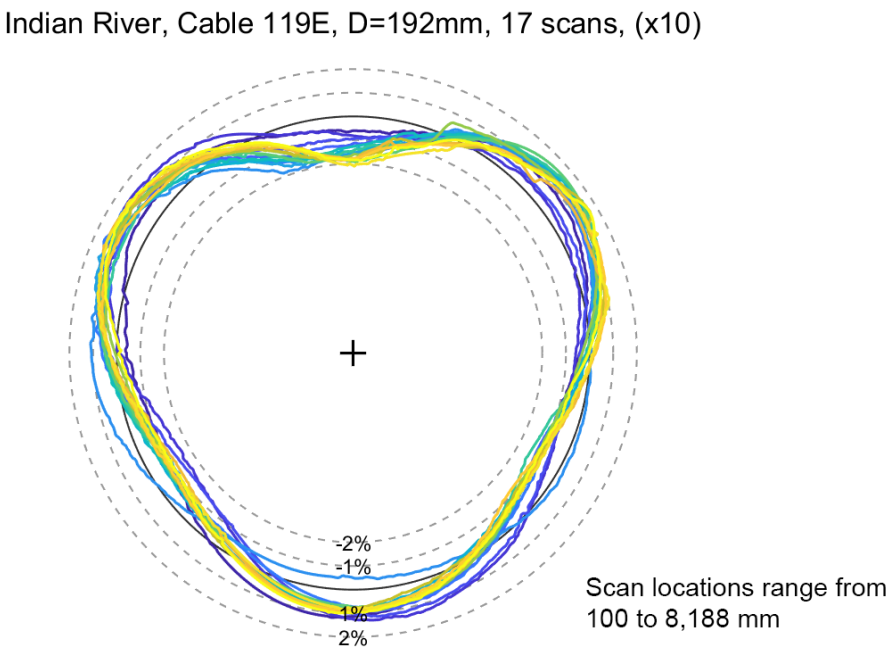

Source: FHWA.

Figure 30. Graph. Percent deviation from the mean plot for cable 119E on the Indian River Bridge.

Although the shapes between cables varied quite a bit, the cross-sectional shape for each individual cable remained similar, indicating that for this bridge, the shape along the length of the cable was generally consistent. Four cables, 113E, 116E, 117E, and 118E, all featured an ellipse or peanut-like shape, which included all three cables with the highest out-of-roundness measurements in table 4. Deviations for cable 118E reached up to 3 percent of the mean, the most of any cable tested for this bridge.

Another reoccurring shape among four of the cables resembled an upside-down triangle. After the initial testing, the team raised the possibility that the clamps could influence the cable's shape by applying too much pressure while closed. Indeed, later tests performed in the lab proved that some HDPE cables could be deformed by the clamp pressure. The robot's climbing algorithm was then adjusted to keep only the upper ring clamped during a measurement, while the lower ring closer to the laser ring relaxed the clamps to prevent any unintentional deformation.

Data from two cables, 113E and 118E, were provided by FHWA to an outside contractor to construct a 3D-printed model of each cable for further wind tunnel testing of a cable's shape's influence on its aerodynamic properties and behavior, which is documented in references 8 and 9.

CHAPTER 6. VARINA-ENON BRIDGE TESTING

FIELD TESTS

The final bridge tested in summer 2015 was the Varina-Enon Bridge, also known as the James River Bridge, located near Richmond, VA. This cable-stayed bridge carries I–295 over the James River and has a main span of 192 m and side spans of 137.2 m. Similar to the C&D Canal Bridge, the Varina-Enon Bridge has two 86.6-m-tall pylon towers that each carry 26 cables anchored at the center of the bridge deck. Two concrete barriers protect the cable anchorages on either side, again providing an ideal, safe testing environment. A photo of the bridge is shown in figure 31.

Figure 31. Photo. The Varina-Enon Bridge.

The robot tested six cables over four days of testing in early July. One unusual observation regarding this bridge: The stay cables had no helical fillets, but the HDPE pipe was wrapped in protective tape. During testing, it was noticed that areas of the tape were exhibiting signs of aging and deterioration, with some peeling and tears as illustrated in figure 32. This uneven surface with flaps of peeling tape, wrinkles, and missing pieces of tape periodically interfered with the laser measurements. Figure 33 shows a photo of the cable robot climbing a cable. A summary of the testing is listed in table 5.

Source: FHWA.

Figure 32. Photo. Protective tape wrapped on HDPE pipe on stay cables.

Source: FHWA.

Figure 33. Photo. The cable robot climbing up a cable at the Varina-Enon Bridge.

Table 5. Summary of Varina-Enon Bridge testing.

Date	Cable	No. of Measurements*	Maximum Distance (mm)
7/10/2015	SS07	13	8,315
7/10/2015	SS08	13	8,170
7/9/2015	SS09	15	9,280
7/9/2015	SS10	21	12,330
7/8/2015	SS11	10	8,940
7/7/2015	SS13	12	2,940

*Note: Some measurements were made multiple times at same location with different resolution.

ANALYSIS AND RESULTS

Data from testing was processed using the custom software described in chapter 3. The gaps in the data surrounding the hinge were filled in using polynomial curve fitting, the data was centered, and the mean, maximum, and minimum radii were calculated for each laser. The resulting data was saved in multiple data file formats.

The out-of-roundness percentage was calculated for each cable scan using equation 1. Table 6 contains a summary of the results from field testing where the mean, maximum, and minimum radii are averaged from all scans for each cable measured.

Table 6. Averaged cable radius data from laser 2 for the Varina-Enon Bridge.

Cable	No. of Measurements	Maximum Distance (m)	Mean Radius (mm)	Maximum Radius (mm)	Minimum Radius (mm)	Out-of-Roundness (percent)
SS07	11	8.3	110.89	111.97	109.99	1.8
SS08	11	8.2	110.56	111.30	109.86	1.3
SS09	13	9.3	110.48	111.46	109.48	1.8
SS10	19	12.3	110.57	111.08	110.11	0.9
SS11	13	8.9	110.55	111.25	109.89	1.2
SS13	10	7.6	110.97	111.57	110.23	1.2

The out-of-roundness of cables tested for the Varina-Enon Bridge varied between 0.9–1.8 percent, which was generally rounder than the cables tested at Indian River Bridge. The diameters of these cables were also much larger than the cables tested at Indian River, although they were slightly smaller than those tested at C&D Canal.

Visualization plots were produced that overlaid all the cross-sectional scans from an individual cable to help identify the cable's general shape and compare how that shape varied along the cable. The cross sections were normalized by the cable's mean diameter, and then the deviation from zero was shown by percentage. The plots were exaggerated by a factor of 15 to make slight deviations more visible. Figure 34 through figure 39 contain the visualization plots for the six cables tested at Varina-Enon. A note contains the range of distances up the cable where the scans were taken, measured either from the anchorage or the end of a guide pipe.

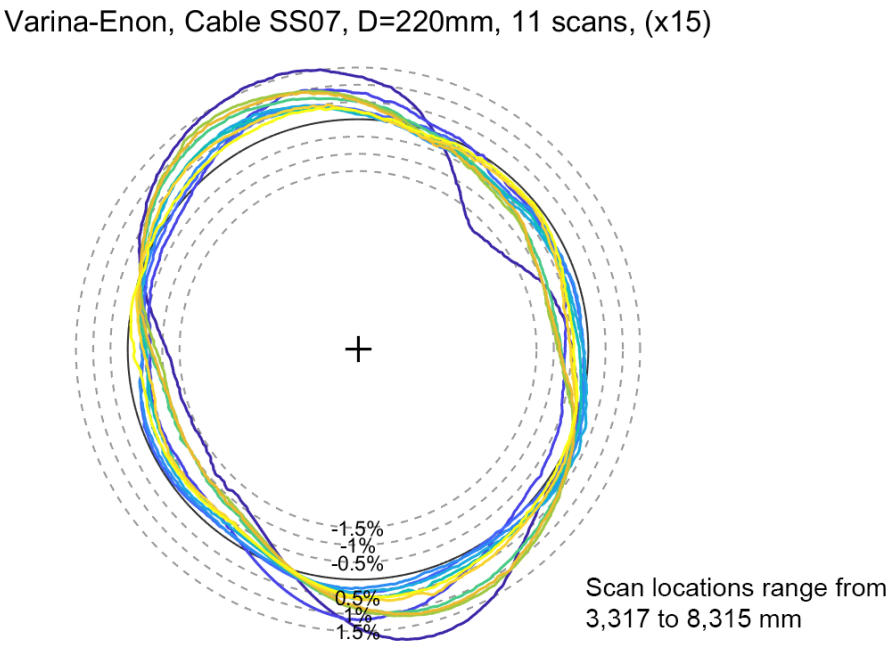

Source: FHWA.

Figure 34. Graph. Percent deviation from the mean plot for cable SS07 on the Varina-Enon Bridge.

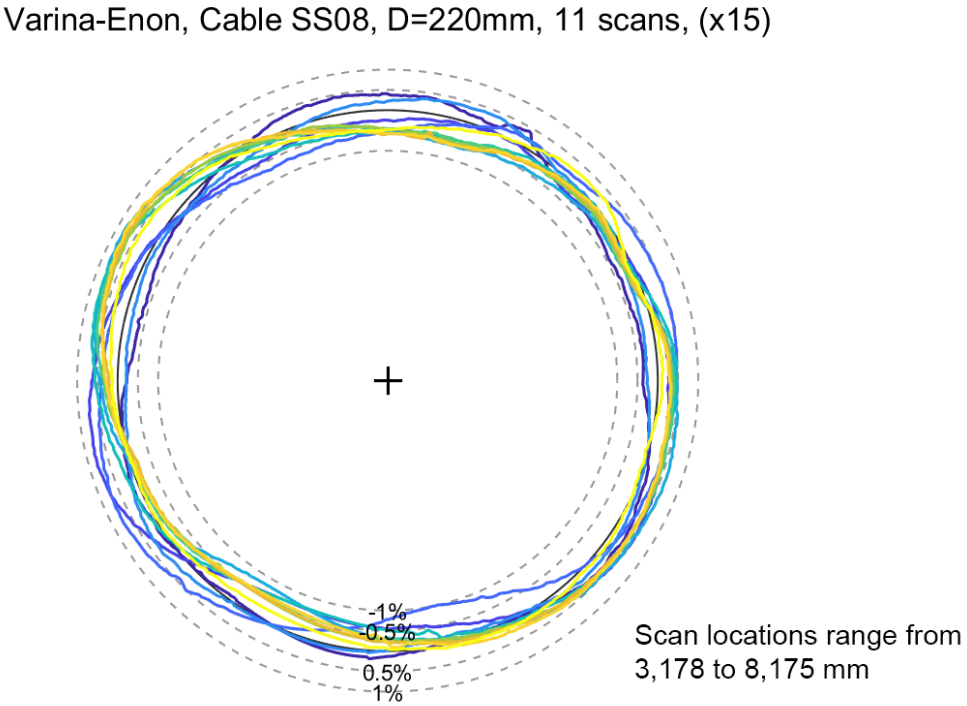

Source: FHWA.

Figure 35. Graph. Percent deviation from the mean plot for cable SS08 on the Varina-Enon Bridge.

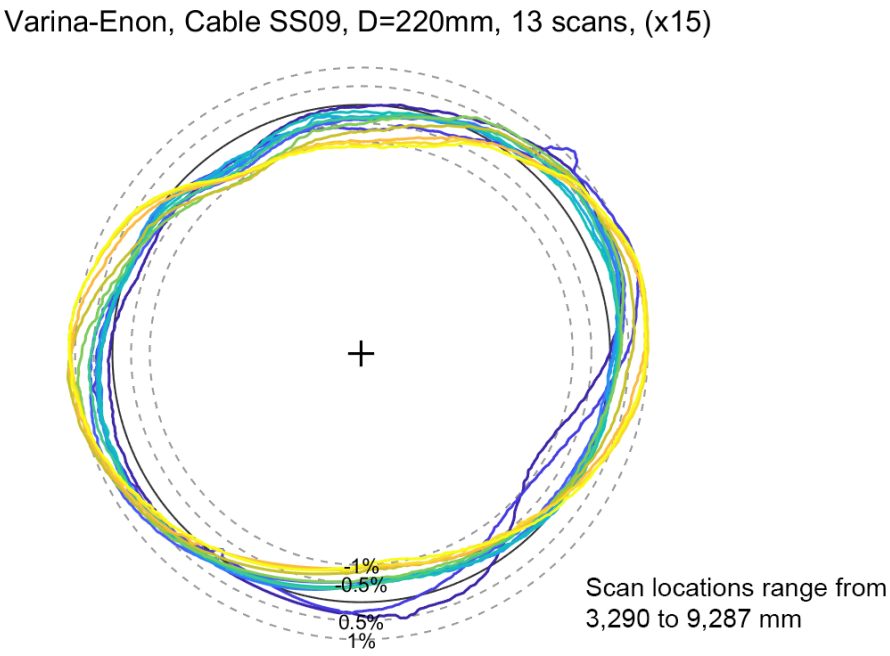

Source: FHWA.

Figure 36. Graph. Percent deviation from the mean plot for cable SS09 on the Varina-Enon Bridge.

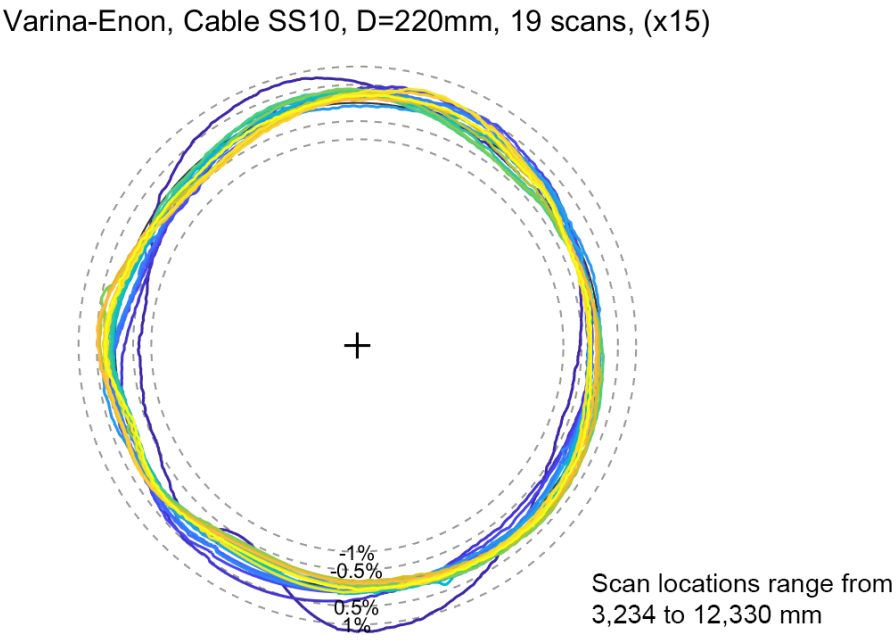

Source: FHWA.

Figure 37. Graph. Percent deviation from the mean plot for cable SS10 on the Varina-Enon Bridge.

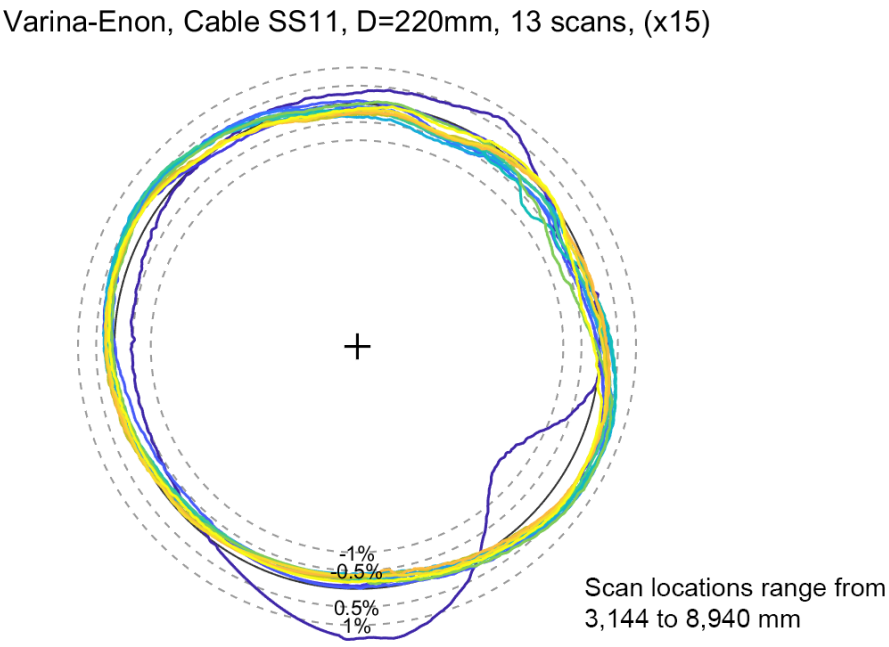

Source: FHWA.

Figure 38. Graph. Percent deviation from the mean plot for cable SS11 on the Varina-Enon Bridge.

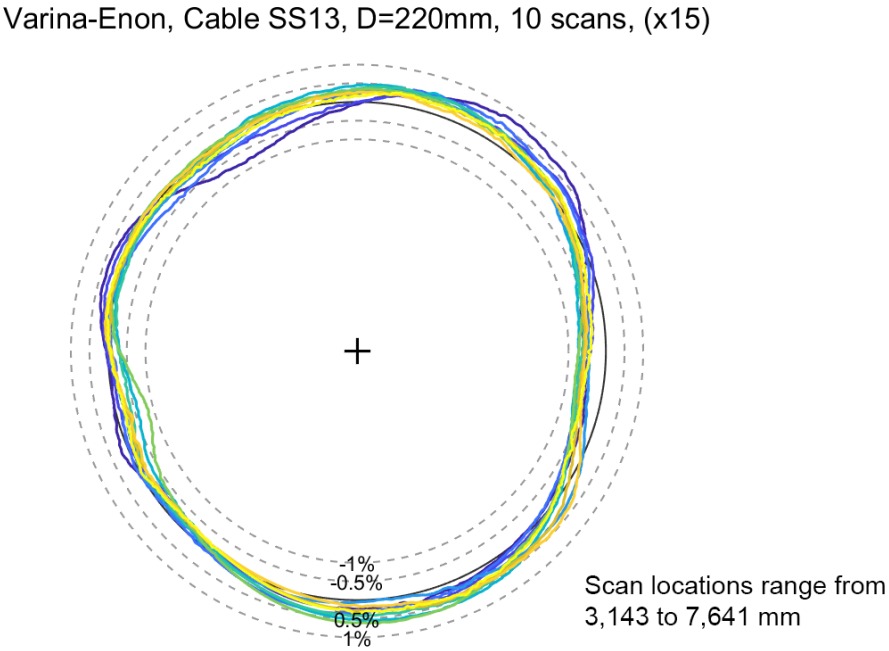

Source: FHWA.

Figure 39. Graph. Percent deviation from the mean plot for cable SS13 on the Varina-Enon Bridge.

The cross-sectional shapes measured along each cable remain fairly consistent. A few noticeable trends exist, the first being that the initial measurements closest to the bridge deck tend to have the most variability. The cross-section measurements become more uniform as they continue along the cable. Cables SS07 and SS09 have the most out-of-roundness, with the cable shapes becoming elliptical and reaching at least one percent of deviation from the mean on either end.

As with data obtained from the Indian River Bridge testing, data from two cables, SS08 and SS13, were provided to an outside contractor to construct a 3D-printed model of the cable for further wind tunnel testing of a cable's shape's influence on its aerodynamic properties and behavior. This research is documented in references 8 and 9.

CHAPTER 7. CONTINUED ROBOT DEVELOPMENT AND UPGRADES

INTRODUCTION

After the initial run of cable testing over summer 2015 was complete, 3 bridge sites were visited, with over 250 cross-sectional scans captured of 17 cables. Data had been successfully collected and postprocessed, and detailed summary datasheets and visualization plots were produced and used to select the most interesting cable shapes for further testing.

Despite the many successes of the cable robot, there were plenty of areas noted for improvement. There was a significant desire to make the robot faster and a more efficient climber to take more measurements on longer stretches of cable in a shorter amount of time. The robot could climb faster if it could stretch its climbing rings further apart, but that would require adding external stabilizing mechanisms to prevent torque from bending and damaging the main spindles and shafts. Another area marked for improvement was the laser carriage and how it relayed data to the DAQ module. A solution was developed that used a wireless transmitter to bypass the interference along the main cable that drives the stepper motors. But the wireless transmission introduced some new problems, as the stepper driver and the DAQ module weren't fully synchronized. As the robot climbed further up the cable away from the receiver, it was more likely to lose contact with the DAQ module and corrupt the data.

This chapter details the improvements implemented on the robot after the initial round of testing was complete.

ELECTROMECHANICAL SYSTEM UPGRADES

Laser Carriage

The laser carriage, which had already undergone significant upgrades before the robot was even tested in the field, was completely overhauled after the initial run of testing. The wireless data system involving the microcontroller and wireless transmitter were discarded and a new digital system was developed that could communicate using the existing robot cable while withstanding interference from the stepper motor controls.

To accomplish this, the driver for the stepper motor on the laser carriage was moved from the control unit box to the carriage itself, connecting directly to the laptop and DAQ module and bypassing the control unit box completely. Thus, the carriage now contained a dedicated system with a microcontroller to act as both a stepper driver for the motor control and data collector from the laser sensors. With all the necessary equipment located directly on the carriage, it could receive a command from the LabVIEW program on the laptop to take a measurement and then very accurately synchronize the steps on the motor with the laser readings. The microcontroller on the carriage converted the laser measurements to a digital signal that could be transmitted back to the laptop on the cable without interference. This new system also produced many more data measurements, from approximately 1,340 to more than 150,000.

To support this new setup an entirely new custom housing unit for the laser carriage was designed and 3D printed. Some of the previous carriage's equipment from the base of the

carriage remained, such as the four V-rollers and the stepper motor and pinion, but the box containing the electronic equipment was completely new. To give more room for the new set of equipment, the lasers were pushed further apart from each other. An additional benefit was gained by spreading the lasers apart: they now could cover more of the 33-degree gap left between them due to the robot's hinge. The gap remained at 33 degrees, but the wider stance of the two lasers permitted more overlap between them. Figure 40 shows a photo of the overhauled laser carriage with the laser sensors mounted on the sides and the stepper motor sitting in the rear.

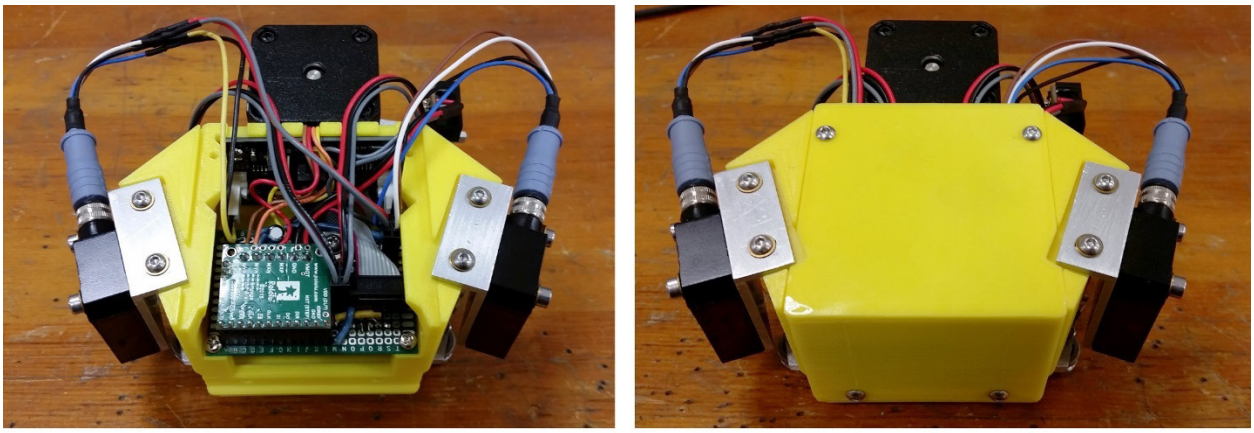

(a) (b)

Source: FHWA.

Figure 40. Photo. The new laser carriage with the electronic circuitry access door (a) open and (b) closed.

Rotary Encoder

Previously, only one of the two rotary encoders located at the top of the trapezoidal spindles could be measured at a time to count the number of rotations of the spindle. This information was then translated to distance traveled and therefore height climbed. To rectify this issue, a pair of special counter chips were added that were designed to communicate with the encoders and produce a simple output of position data. This data was broadcast wirelessly to the DAQ module using the old wireless transmitter from the original laser carriage setup. The electronics equipment for the rotary encoder was enclosed in a new 3D-printed box and mounted to the robot's top ring. Now, the settings of both rotary encoders could be relayed down to the laptop, and the positions of both spindles could be known at all times.

Linear Potentiometers

Despite interference and calibration issues with the linear potentiometers in the early stages of development, by the second year, the potentiometers were fully enabled to help control the clamps. The potentiometer data still experienced a great deal of interference along the cable, which required extensive averaging to cancel out the noise, but the resulting position data helped improve the climbing algorithms that were programmed in LabVIEW.

CLIMBING SYSTEM UPGRADES

Wheel Supports

Another focus area was the wheels added to the ring C platform to help support the robot and prevent the open clamps from dragging along the cable as it climbed. When the robot's center of gravity shifted as the robot climbed, the weight shifts would rock the robot and subject it to sudden stresses. To prevent this rocking motion, a variety of new wheel placements were tested that could more evenly support the robot's weight.

A wheel was added to the bottom rear of the laser ring platform, supporting the robot on the top edge of the stay cable, which allowed the removal of two wheels on the other end. The addition of the rear wheel made the robot faster, but the wheel mount, built using 3D-printed plastic, ultimately fractured after repeated climbing tests in the lab.

However, after seeing that a rear wheel successfully distributed the robot's weight more evenly and allowed the robot to extend its ring platforms further without added stress, which in turn allowed it to climb faster, a new concept was tested. A special bracket head was designed that combined the clamp head with a pair of wheels for one of the lower ring platform clamps. When the clamps were open, the wheels would sit on a spring-loaded rig to allow the clamp to roll along the cable. When the force of the clamp was applied, the wheels would be pushed out of the way and the clamp could close. This custom-designed bracket allowed the robot to smoothly roll up the cable as it climbed, supporting the weight evenly, reducing the stresses, and improving the speed. Additionally, the pair of wheels on the clamp were parallel to each other, allowing the robot to self-center as it climbed. Figure 41 shows a photo of the clamp with the special spring-loaded wheel assembly.

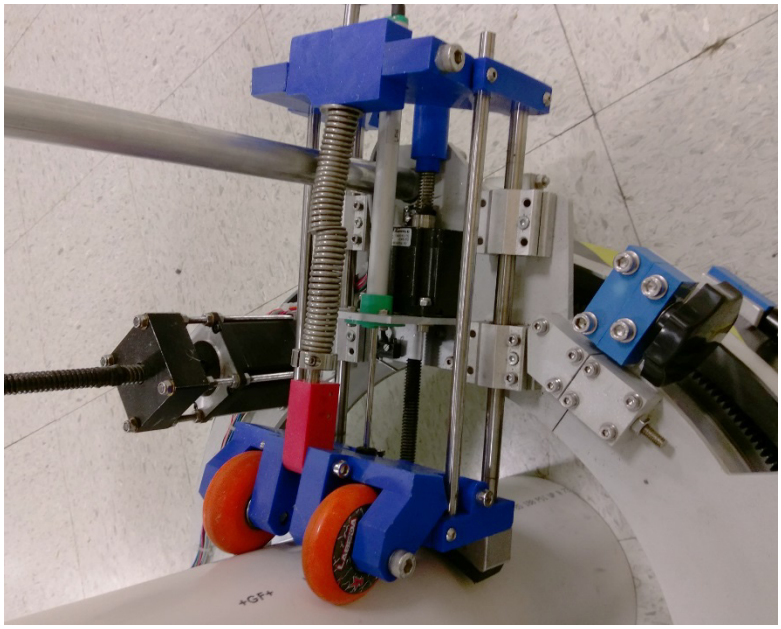

Source: FHWA.

Figure 41. Photo. Clamp with a spring-loaded wheel assembly.

Customized Bracket Heads

A change to the clamp bracket heads was also implemented to allow better compatibility with a wider range of cable diameters. The original bracket heads were steel with a rubber grip and contained a specific (fixed) curvature. For cables with a smaller diameter, all the pressure from the clamp on the bracket head would concentrate at a single tangent point on the cable.

The bracket heads were replaced with a newer version that allowed the front of the head to be changed as needed. Multiple bracket heads with a variety of curvatures were machined to better fit the wide range of cables found in the field. These new heads could be easily changed using a screwdriver. Figure 42 shows a collection of the replaceable bracket heads with a variety of curvatures.

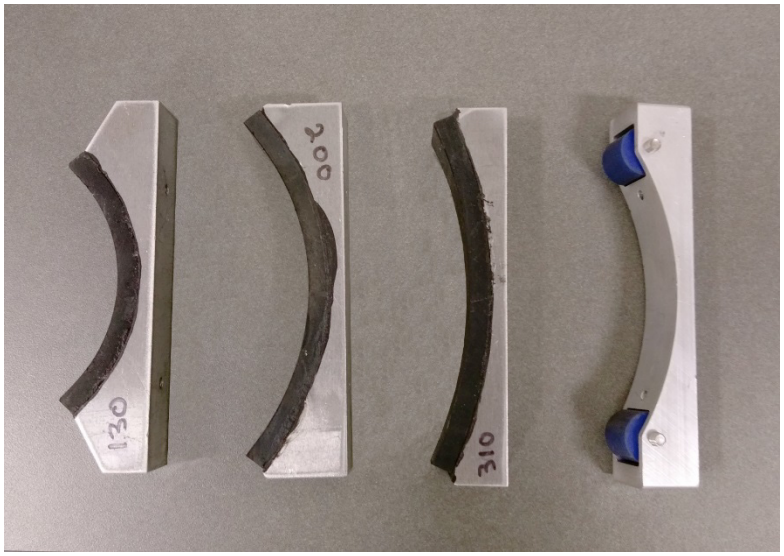

Source: FHWA.

Figure 42. Photo. Replaceable steel bracket heads featuring a range of curvatures and a bracket with rubber bearings.

Eventually, another concept for the bracket head was designed and tested. These brackets were 3D-printed and essentially flat but contained anchor spots for steel or rubber bearings. The goal of introducing bearings to the bracket heads was to allow the head to self-center as the clamp closed. Therefore, if the clamp closed off-center, the bearings allowed the clamp to slide to the side and ease back in place. Figure 43 shows a clamp with a 3D-printed swappable bracket head with two rubber bearings resting against a pipe.

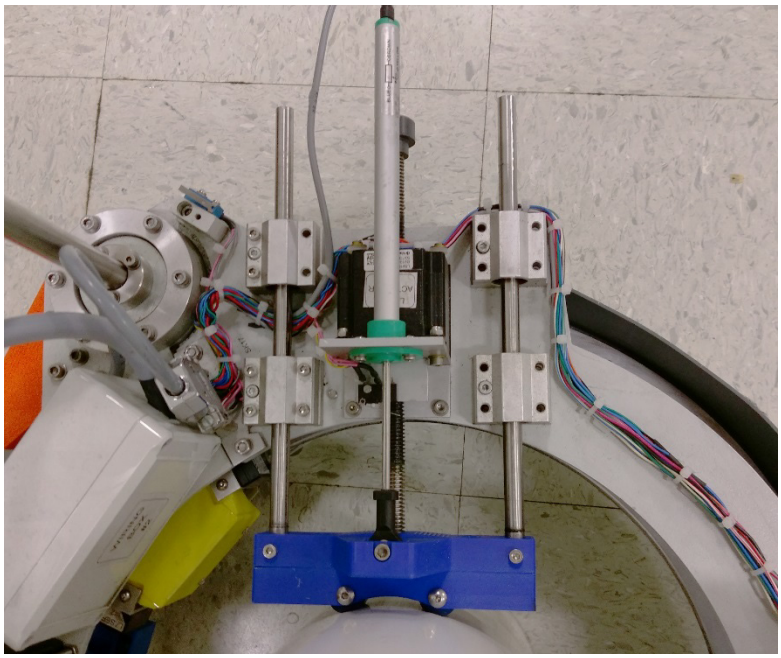

Source: FHWA.

Figure 43. Photo. A clamp utilizing a 3D-printed bracket head with rubber bearings.

This new variety of customized bracket heads provided more appropriate clamp heads for a larger variation of cable sizes and clamping scenarios.

PRECISION CALIBRATION PLATFORM

A special calibration tool was also designed and constructed during this phase to facilitate accurate measurements of the machined plastic discs. The tool comprised an aluminum frame with three special 3D-printed mounts where the robot's stabilizer shafts could rest. The center of the frame had a small movable platform that could be finely adjusted in the X and Y directions by turning a pair of knobs. The discs could then be mounted on the platform for taking calibration measurements. Additionally, a thin steel rod could be mounted on the platform to help center the lasers. This calibration tool was an asset in improving the accuracy of the robot's measurements. Figure 44 is a photo of the calibration tool with a disc mounted on the adjustable platform.

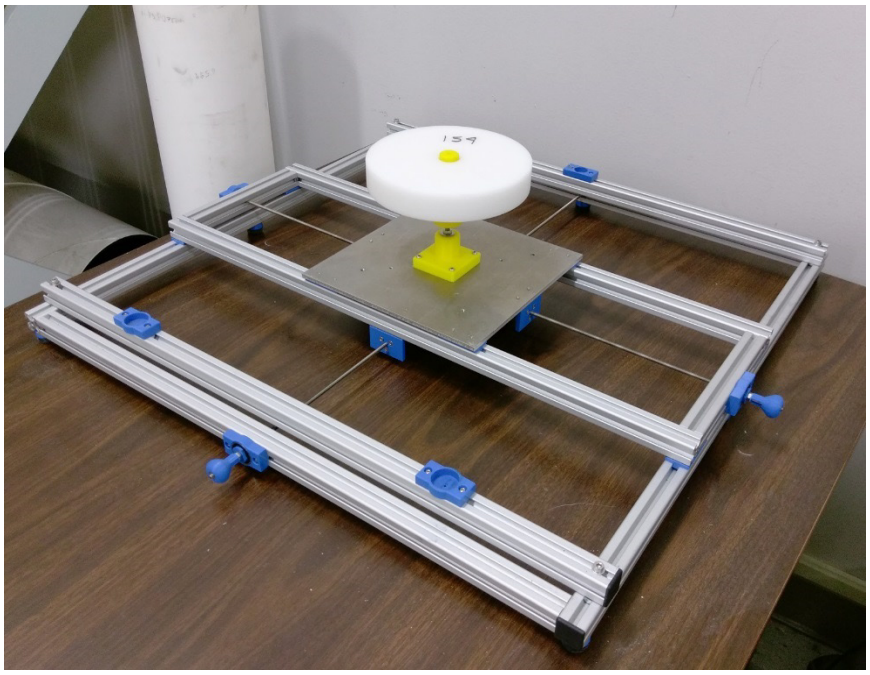

Source: FHWA.

Figure 44. Photo. The precision calibration platform.

CHAPTER 8. IRONTON-RUSSELL BRIDGE TESTING

FIELD TESTS

The first bridge tested in summer 2016 was the Ironton-Russell Bridge, officially known as the Oakley C. Collins Memorial Bridge, a two-lane cable-stayed bridge that connects Ironton, OH, and Russell, KY, over the Ohio River. The bridge consists of two 96.0-m tall, diamond-shaped towers that support a 274.3-m main span and two 112.8-m side spans with 30 pairs of cable stays per tower anchored at either edge of the bridge deck. This bridge replaced an outdated, cantilevered thru-truss structure that had been ruled structurally deficient and functionally obsolete by the Ohio Department of Transportation in 2000. Figure 45 is an aerial photo of the Ironton-Russell Bridge.

Figure 45. Photo. The Ironton-Russell Bridge.

The bridge was tested in July while it was still under construction, which provided an ideal testing environment free of vehicular traffic. At this stage of construction, the deck was fully connected and supported by the cable stays, but smaller projects such as the erection of concrete barriers and damper installation were ongoing. Eight cables in total were tested, including the longest four cables from each side span of the bridge, although one of the cables included only a single measurement due to poor weather. Figure 46 shows the robot climbing a cable at the bridge site and the laptop and other equipment set up on the bridge deck. Figure 47 shows a view from the side of the robot with the sunshade visible, a piece of sturdy plastic wrapped around the robot to prevent sunlight and shadows from interfering with the laser measurements. A summary of all testing is listed in table 7.

Source: FHWA.

Figure 46. Photo. The robot climbing a cable on the Ironton-Russell Bridge.

Source: FHWA.

Figure 47. Photo. The robot climbing a cable, with the sunshade visible.

Table 7. Summary of Ironton-Russell Bridge testing.

Date	Cable	No. of Measurements	Maximum Distance (mm)
7/20/2016	B12	16	8,955
7/20/2016	B13	33	16,901
7/19/2016	B14	20	10,000
7/19/2016	B15	28	14,559
7/22/2016	B27	1	104
7/21/2016	B28	15	8,907
7/21/2016	B29	32	15,879
7/22/2016	B30	30	14,340

ANALYSIS AND RESULTS

Data from testing was processed using the custom software described in chapter 3. The gaps in the data surrounding the hinge were filled in using polynomial curve fitting, then the data was centered, and the mean, maximum, and minimum radii were calculated for each laser. The resulting data was saved in multiple data file formats.

The out-of-roundness percentage was calculated for each cable scan using equation 1. Table 8 contains a summary of the results from field testing where the mean, maximum, and minimum radii are averaged from all scans from each cable measured.

Table 8. Averaged cable radius data from laser 2 for the Ironton-Russell Bridge.

Cable	No. of Measurements	Maximum Distance (m)	Mean Radius (mm)	Maximum Radius (mm)	Minimum Radius (mm)	Out-of-Roundness (percent)
B12	16	9.0	80.61	81.53	79.47	2.5
B13	33	16.9	80.49	81.29	79.52	2.2
B14	20	10.0	80.50	81.63	79.28	2.9
B15	28	14.6	90.57	91.76	89.41	2.6
B27	1	0.1	80.62	81.56	79.67	2.3
B28	15	8.9	80.79	81.45	79.91	1.9
B29	32	15.9	80.51	81.31	79.45	2.3
B30	30	14.3	90.64	91.49	89.60	2.1

The tested cables' out-of-roundness varied between 1.9–2.9 percent, which was slightly rounder than the cables tested at the Indian River Bridge (the Indian River cables were the most out-of-round cables tested). The Ironton-Russell Bridge's cables' diameters were the smallest tested, about a centimeter smaller than Indian River.

Visualization plots were produced that overlaid all the cross-sectional scans from an individual cable to help identify the cable's general shape and compare how that shape varied along the cable. The cross sections were normalized by the cable's mean diameter, and then the deviation from zero was shown by percentage. The plots were exaggerated by a factor of 15 to make slight deviations more visible. Figure 48 through figure 55 contain the visualization plots for the eight

cables tested at the Ironton-Russell Bridge. A note contains the range of distances up the cable where the scans were taken, measured either from the anchorage or the end of a guide pipe.

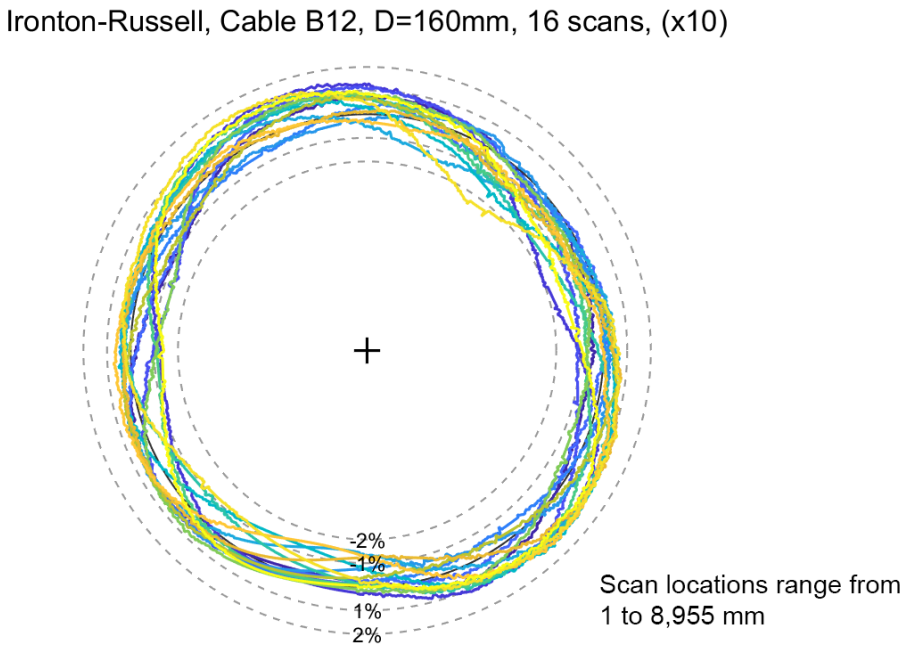

Source: FHWA.

Figure 48. Graph. Percent deviation from the mean plot for cable B12 on the Ironton-Russell Bridge.

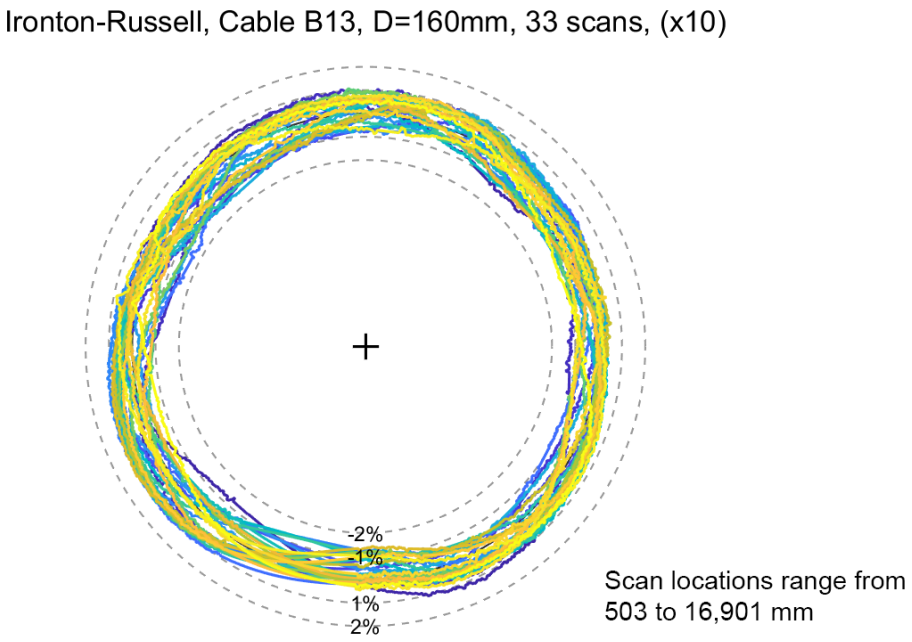

Source: FHWA.

Figure 49. Graph. Percent deviation from the mean plot for cable B13 on the Ironton-Russell Bridge.

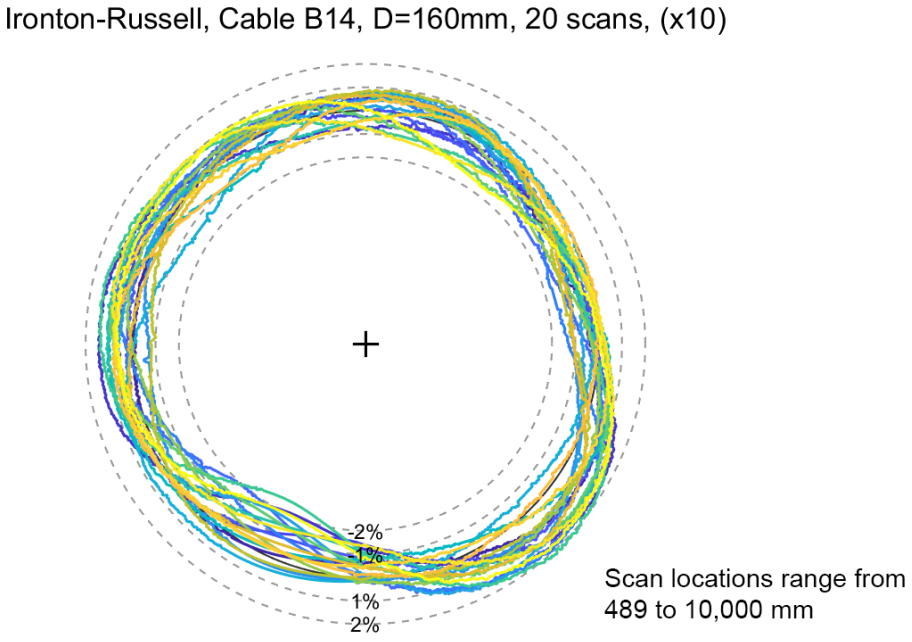

Source: FHWA.

Figure 50. Graph. Percent deviation from the mean plot for cable B14 on the Ironton-Russell Bridge.

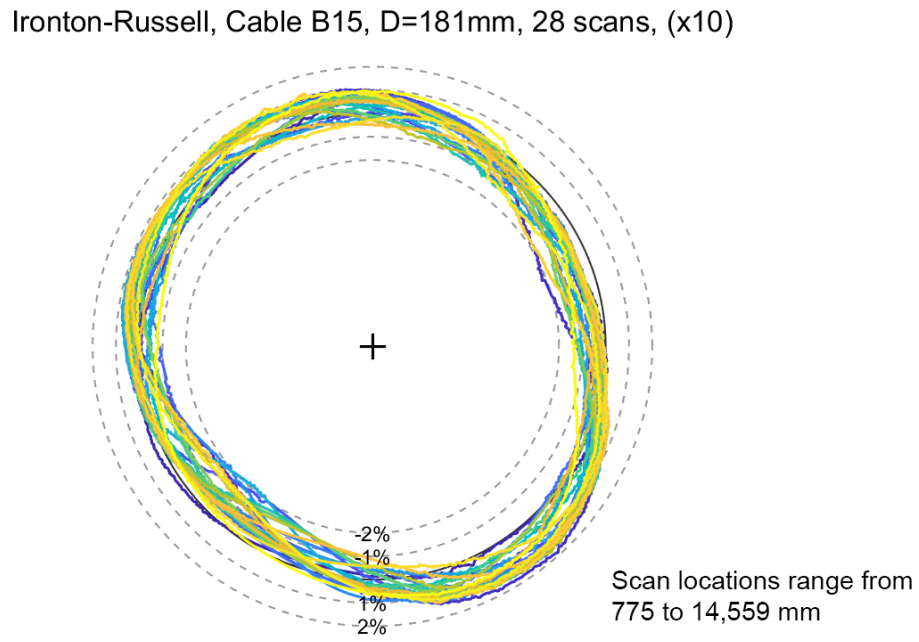

Source: FHWA.

Figure 51. Graph. Percent deviation from the mean plot for cable B15 on the Ironton-Russell Bridge.

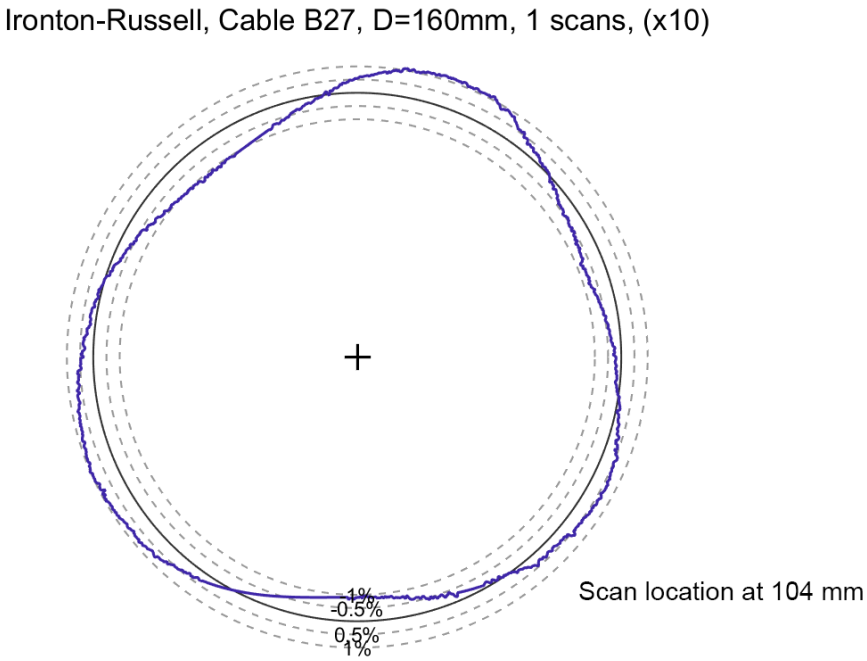

Source: FHWA.

Figure 52. Graph. Percent deviation from the mean plot for cable B27 on the Ironton-Russell Bridge.

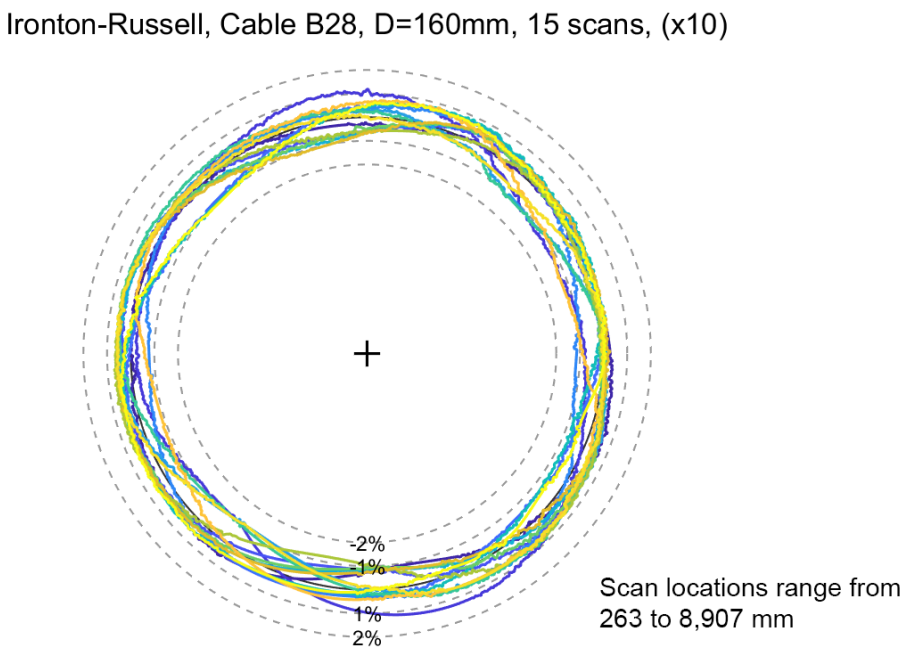

Source: FHWA.

Figure 53. Graph. Percent deviation from the mean plot for cable B28 on the Ironton-Russell Bridge.

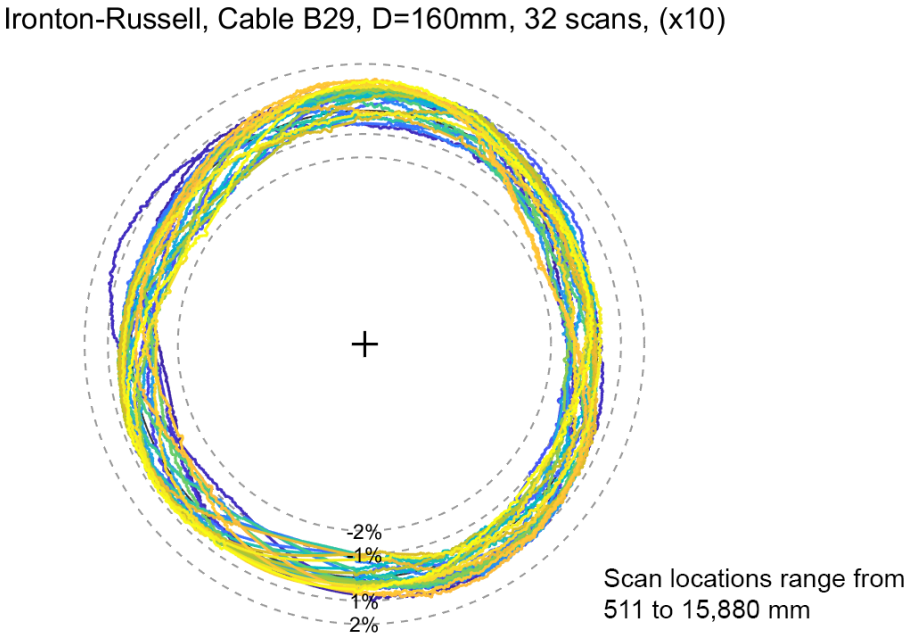

Source: FHWA.

Figure 54. Graph. Percent deviation from the mean plot for cable B29 on the Ironton-Russell Bridge.

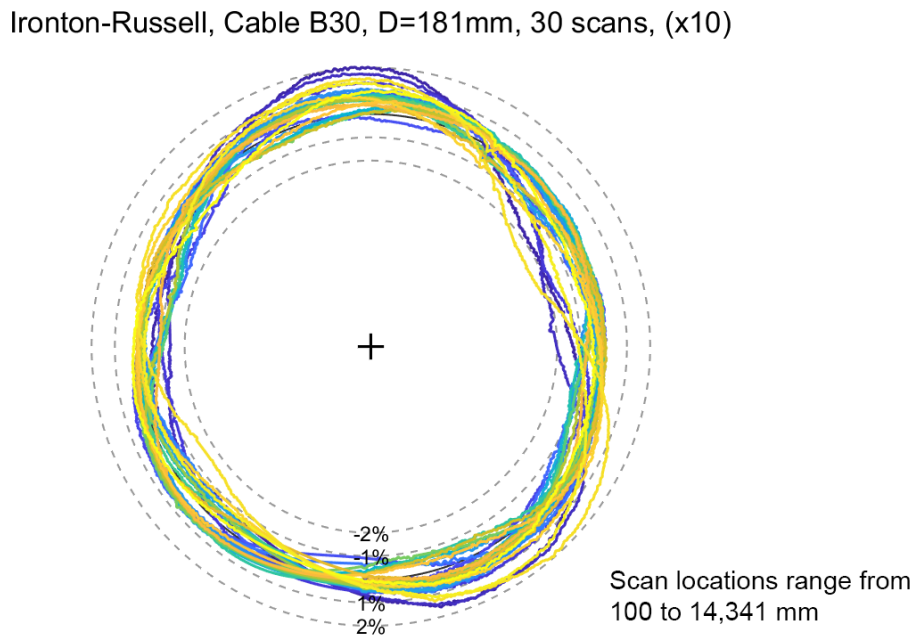

Source: FHWA.

Figure 55. Graph. Percent deviation from the mean plot for cable B30 on the Ironton-Russell Bridge.

Compared to earlier testing, the more efficient cable robot was able to greatly increase the number of scans recorded, with four cables reaching 28, 30, 32, and 33 measurements. For the first time, the robot was able to collect multiple scans from different sections of the same cable. Ironton-Russell Bridge cables all contained a short initial section slightly larger than a half-meter, before transitioning to a full cable section that was usually 12–13-m long. For three cables, the robot reached a third section for measurements.

Considering the high volume of scans on each cable, it is notable that the shape for each cable tended to remain consistent along the length of the cable, even across multiple sections. Most of the cables had a fairly round shape, but cables B15 and B30 had more of an egg shape. These cables were also the longest cables measured on the bridge, and their cable diameters were larger than the other cables tested.

CHAPTER 9. U.S. GRANT BRIDGE TESTING

FIELD TESTS

The U.S. Grant bridge was tested in late fall 2016. The bridge is a lightly traveled, two-lane cable-stayed bridge carrying U.S. Route 23 and connecting Portsmouth, OH, and South Portsmouth, KY, over the Ohio River. The cable-stayed bridge has a main span of 266.7 m, one side span of 106.7 m, and another side span of 140.2 m. The spans are supported by two 87.9-m-tall pylon towers that each carry 32 cable stays anchored at the edges of the bridge deck. The cables were located on the outside of a 91.4-cm-high concrete barrier with steel railings. This bridge was the first tested where the stay cables were interconnected with crossties. Each tower quadrant had two lines of crossties installed, which were anchored to the deck. A photo of the bridge is shown in figure 56.

Source: FHWA.

Figure 56. Photo. The U.S. Grant Bridge.

Testing occurred in two phases, the first taking place while the bridge was closed to vehicular traffic as a State contractor resurfaced the overlay of the deck. However, after three days the session was interrupted by inclement weather, which cut short the week of testing. A month later, testing resumed. By this time, the resurfacing project was complete, and the bridge had reopened to traffic. However, the bridge features a wide shoulder equal to a lane of traffic, offering enough space to safely set up all the testing equipment. An additional four days of testing were successfully completed in the second session. The presence of crossties served as an obstacle and limited the available climbing distance on certain cables. During testing, it was observed that some of the crosstie segments seemed to have little or no pretension. A photo of the robot climbing the cable is shown in figure 57. Table 9 contains a summary of all the testing.

Source: FHWA.

Figure 57. Photo. The robot climbing a cable at the U.S. Grant Bridge.

Table 9. Summary of U.S. Grant Bridge testing.

Date	Cable	No. of Measurements	Maximum Distance (mm)
9/28, 10/24/2016	CN1D	57	24,945
10/25/2016	CN2D	51	24,855
10/26/2016	CN1U	26	12,220
10/26/2016	CN2U	26	12,639
9/27/2016	CS1D	26	12,830
9/26/2016	CS2D	17	8,064
9/27/2016	CS3D	29	13,302
10/27/2016	CS16D	24	11,216

ANALYSIS AND RESULTS

Data from testing was processed using the custom software described in chapter 3. The gaps in the data surrounding the hinge were filled in using polynomial curve fitting, then the data was centered, and the mean, maximum, and minimum radii were calculated for each laser. The resulting data was saved in multiple data file formats.

The out-of-roundness percentage was calculated for each cable scan using equation 1. Table 10 contains a summary of the results from field testing where the mean, maximum, and minimum radii are averaged from all scans for each cable measured.

Table 10. Averaged cable radius data from laser 2 for the U.S. Grant Bridge.

Cable	No. of Measurements	Maximum Distance (m)	Mean Radius (mm)	Maximum Radius (mm)	Minimum Radius (mm)	Out-of-Roundness (percent)
CN1D	57	24.9	100.19	100.57	99.75	0.8
CN2D	51	24.9	100.04	100.44	99.54	0.9
CN1U	26	12.2	100.24	100.63	99.76	0.9
CN2U	26	12.6	100.14	100.48	99.71	0.8
CS1D	26	12.8	100.22	100.83	99.60	1.2
CS2D	17	8.1	100.44	100.91	99.96	0.9
CS3D	29	13.3	100.33	100.83	99.83	1.0
CS16D	24	11.2	100.19	100.61	99.74	0.9

The out-of-roundness for the cables was extremely small, with all but one cable in the range of 0.8–1 percent. The one cable with a larger out-of-roundness was still at only 1.2 percent. By comparison, Ironton-Russell's smallest percentage out of all cables tested was 1.9 percent.

Visualization plots were produced that overlaid all the cross-sectional scans from an individual cable to help identify the cable's general shape and compare how that shape varied along the cable. The cross sections were normalized by the cable's mean diameter, and then the deviation from zero was shown by percentage. The plots were exaggerated by a factor of 15 to make slight deviations more visible. Figure 58 through figure 65 contain the visualization plots for the eight cables tested at U.S. Grant Bridge. A note contains the range of distances up the cable where the scans were taken, measured either from the anchorage or the end of a guide pipe.

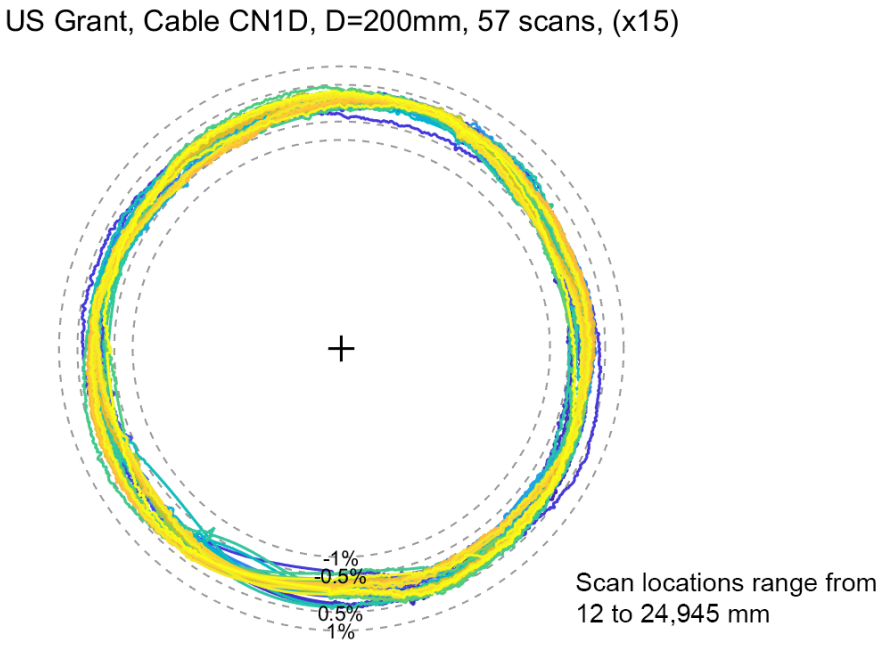

Source: FHWA.

Figure 58. Graph. Percent deviation from the mean plot for cable CN1D on the U.S. Grant Bridge.

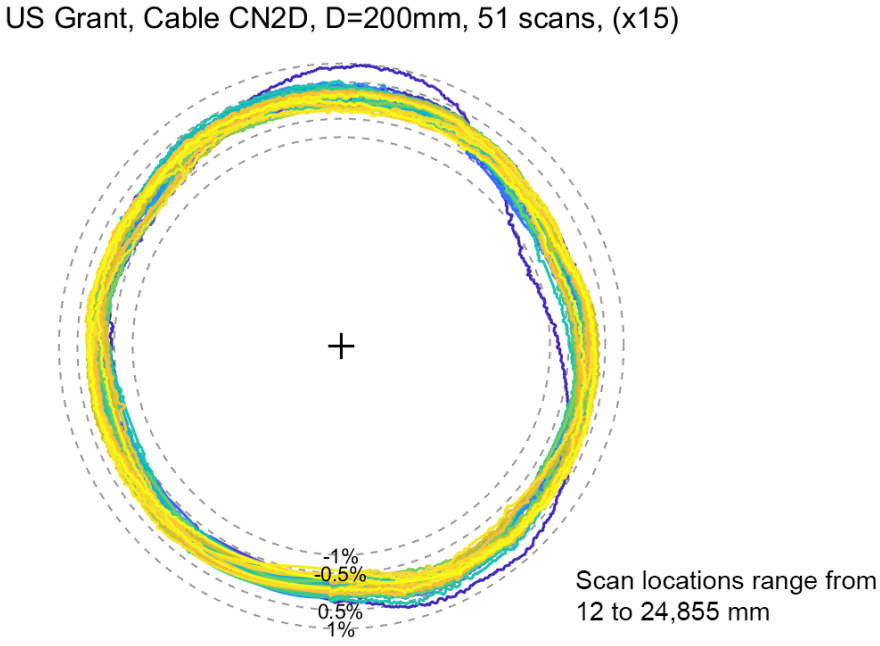

Source: FHWA.

Figure 59. Graph. Percent deviation from the mean plot for cable CN2D on the U.S. Grant Bridge.

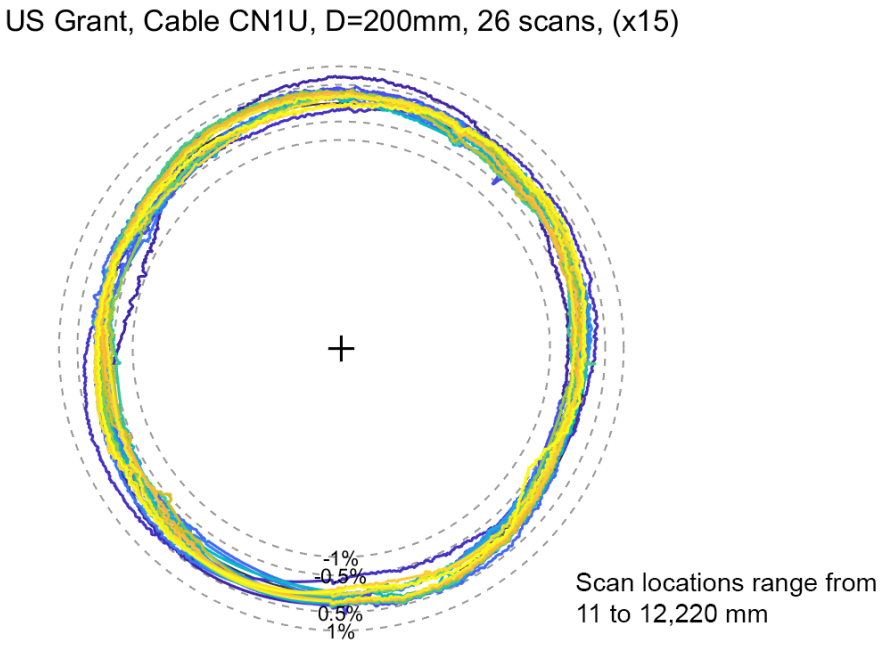

Source: FHWA.

Figure 60. Graph. Percent deviation from the mean plot for cable CN1U on the U.S. Grant Bridge.

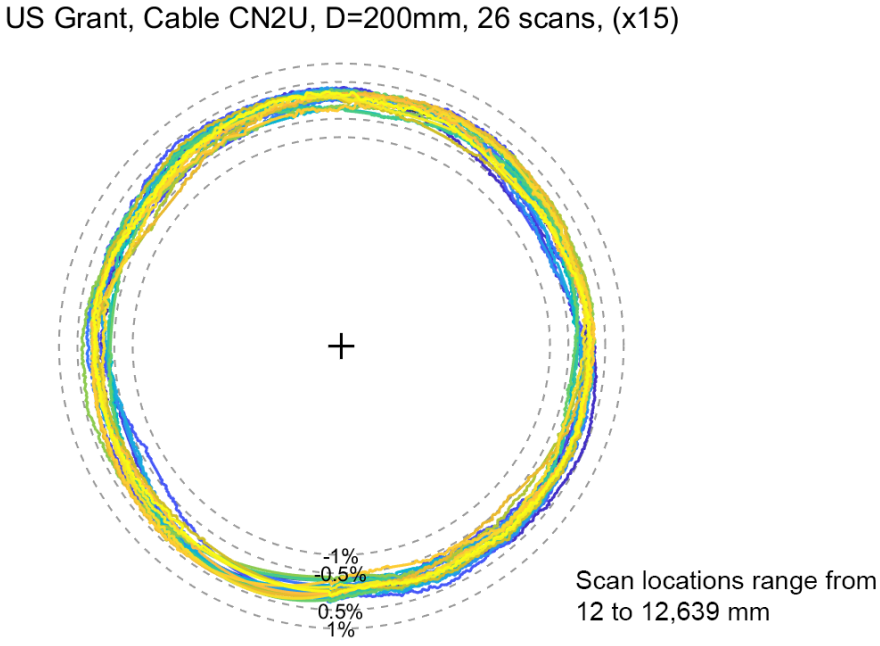

Source: FHWA.

Figure 61. Graph. Percent deviation from the mean plot for cable CN2U on the U.S. Grant Bridge.

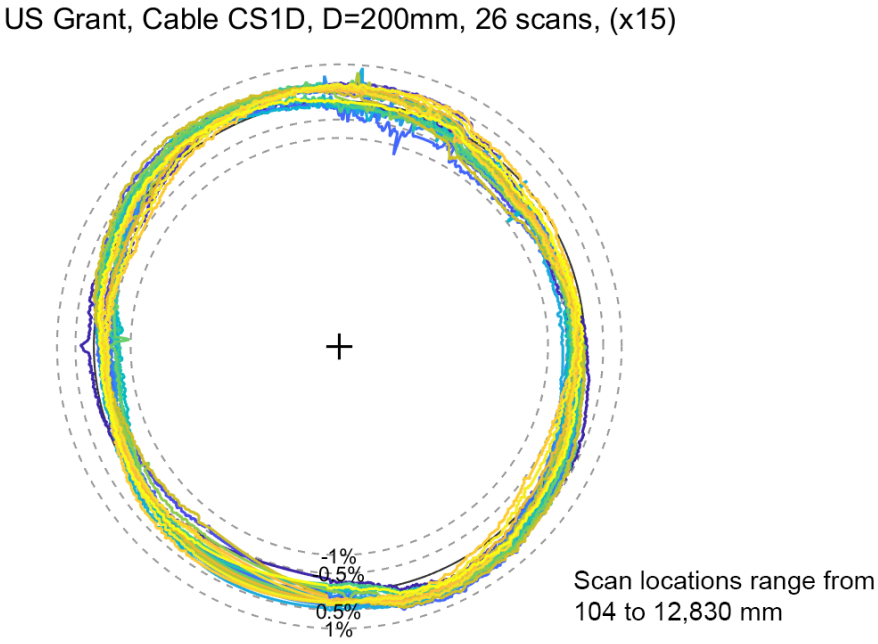

Source: FHWA.

Figure 62. Graph. Percent deviation from the mean plot for cable CS1D on the U.S. Grant Bridge.

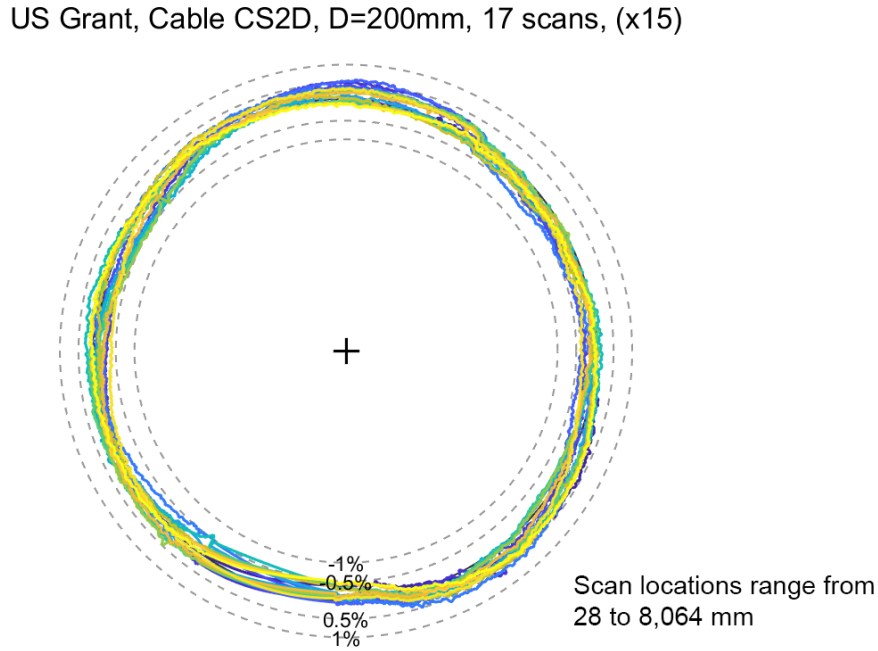

Source: FHWA.

Figure 63. Graph. Percent deviation from the mean plot for cable CS2D on the U.S. Grant Bridge.

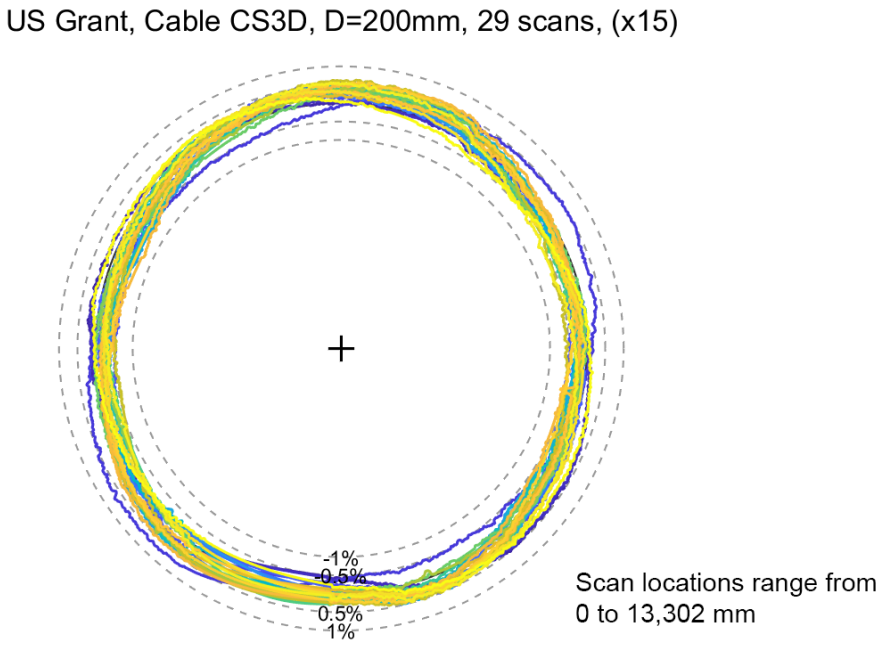

Source: FHWA.

Figure 64. Graph. Percent deviation from the mean plot for cable CS3D on the U.S. Grant Bridge.

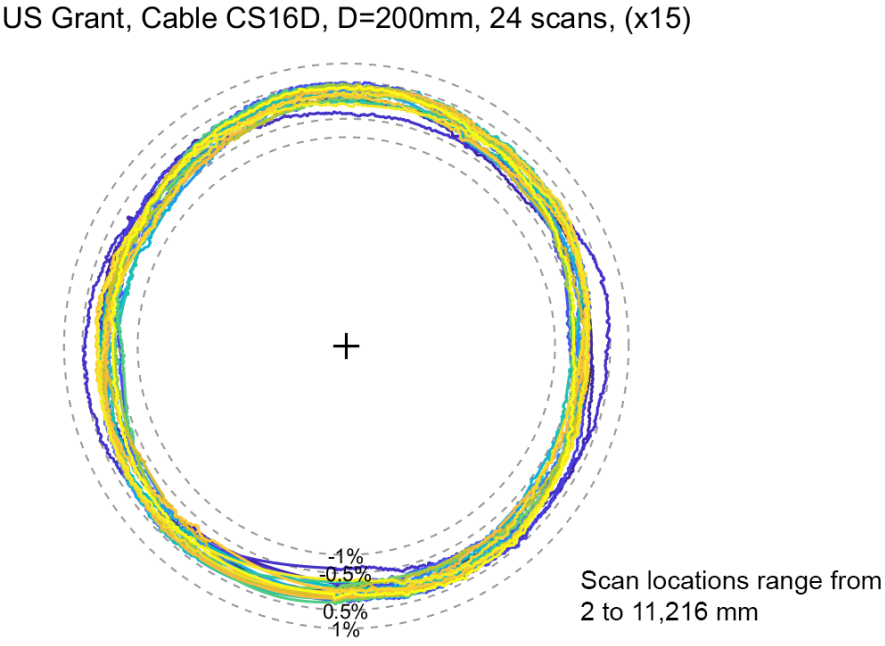

Source: FHWA.

Figure 65. Graph. Percent deviation from the mean plot for cable CS16D on the U.S. Grant Bridge.

Although this report stated previously that the tested cables of this bridge were some of the most round according to the simple out-of-roundness formula, close analysis of the cable scans reveals slight but distinct deformations in the profile. One of the most notable deformations appears as a bump on the right side of the scans around 90 degrees. This deformation appears as a small bump on cables CS1D, CS2D, CS3D, and CS16D but is much larger on cables CN1D, CN2D, CN1U, and CN2U. Another bulge common among all the cable scans appears 15-degrees counterclockwise from the top of the cable.

Despite these small deformations, the radii of these scans mainly stay within ±0.5 percent. It should also be noted that the scans are very consistent among the cables, although for some cables, scans nearer the bottom of the cable have more variability.

CHAPTER 10. EAST END BRIDGE TESTING

FIELD TESTS

The East End Bridge (officially known as the Lewis and Clark Bridge) is a newly constructed cable-stayed bridge carrying I–265 traffic over the Ohio River northeast of Louisville, KY, connecting the outskirts of the city with Indiana. The bridge has a main span of 365.8 m, side spans of 164.6 m, and a large 3.35-m walkway/bike path on the downriver side. Two inverted-V towers, each carrying 26 cables per side, support the bridge spans. The anchorages were located on the edges of the bridge deck outside a concrete-and-steel barrier. The East End Bridge is accompanied by several thru-truss bridges in the greater Louisville area and has a companion sister cable-stayed bridge, the Abraham Lincoln Bridge, in downtown Louisville. A photo of one of the East End Bridge's towers detailing the cable arrangement is shown in figure 66.

Source: FHWA.

Figure 66. Photo. One of the towers of the East End Bridge.

Testing occurred in early December 2016 while the bridge was still under construction, allowing easy access to the cables without any vehicular traffic. Due to a complex, above-deck anchorage and guide pipe system, the first measurable section of the cable was located roughly 2.44–3.05 m above the bridge deck, which required scaffolding around the concrete-and-steel barrier for accessing and mounting the robot. Figure 67 shows the robot climbing on a cable from the East End Bridge and shows the scaffolding near the anchorage used to access the cable. Figure 68 is a different angle of the test setup, which includes the entire bridge deck and the towers in the background. Table 11 contains a summary of all the testing.

Source: FHWA.

Figure 67. Photo. The test setup on the East End Bridge, including the scaffolding near the cable anchorage.

Source: FHWA.

Figure 68. Photo. The test setup on the East End Bridge, with the towers in the background.

Table 11. Summary of East End Bridge testing.

Date	Cable	No. of Measurements	Maximum Distance (mm)
11/30/2016	C4B8U	37	17,916
12/1/2016	C4B7U	44	21,387
12/2/2016	C3B8U	44	22,405
12/3/2016	C4M8U	42	21,280
12/5/2016	C4M7U	52	26,774

ANALYSIS AND RESULTS

Data from testing was processed using the custom software described in chapter 3. The gaps in the data surrounding the hinge were filled in using polynomial curve fitting, then the data was centered, and the mean, maximum, and minimum radii were calculated for each laser. The resulting data was saved in multiple data file formats.

The out-of-roundness percentage was calculated for each cable scan using equation 1. Table 12 contains a summary of the results from field testing where the mean, maximum, and minimum radii are averaged from all scans from each cable measured.

Table 12. Averaged cable radius data from laser 2 for the East End Bridge.

Cable	No. of Measurements	Maximum Distance (m)	Mean Radius (mm)	Maximum Radius (mm)	Minimum Radius (mm)	Out-of-Roundness (percent)
C3B8U	44	22.4	112.81	113.62	111.96	1.5
C4B7U	44	21.4	112.78	113.63	111.92	1.5
C4B8U	36	17.9	112.97	114.09	111.56	2.2
C4M7U	52	26.8	112.84	113.66	111.96	1.5
C4M8U	41	21.3	112.80	113.88	111.63	2.0

The out-of-roundness for these cables varied from 1.5–2.2 percent, which was about average compared to all the cables tested for the project thus far. The cables did have one of the larger diameters tested, just slightly larger than the Varina-Enon Bridge cables.

Visualization plots were produced that overlaid all the cross-sectional scans from an individual cable to help identify the cable's general shape and compare how that shape varied along the cable. The cross sections were normalized by the cable's mean diameter and then the deviation from zero was shown by percentage. The plots were exaggerated by factors of 10–15 to make slight deviations more visible. Figure 69 through figure 73 contain the visualization plots for the five cables tested at East End Bridge. A note contains the range of distances up the cable where the scans were taken, measured either from the anchorage or the end of a guide pipe.

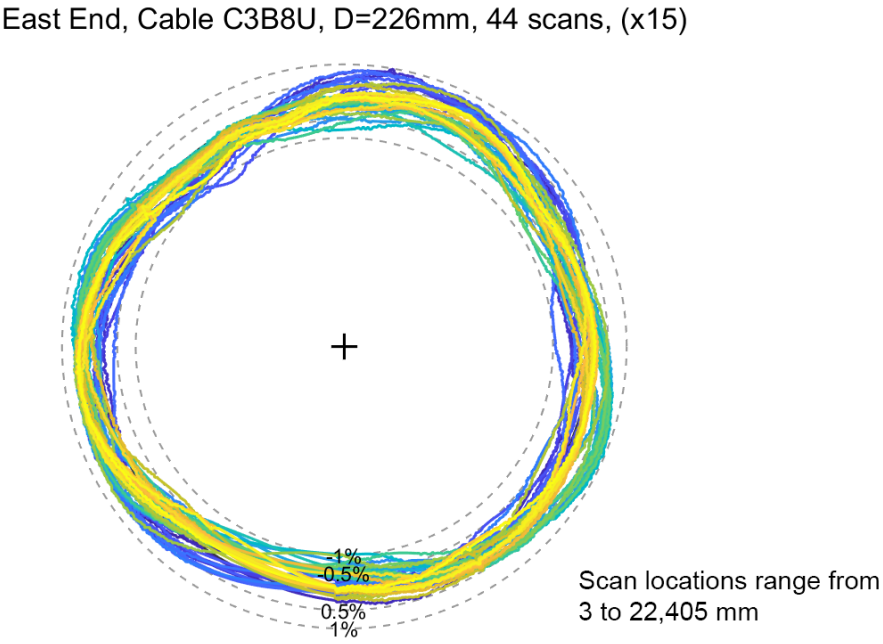

Source: FHWA.

Figure 69. Graph. Percent deviation from the mean plot for cable C3B8U on the East End Bridge.

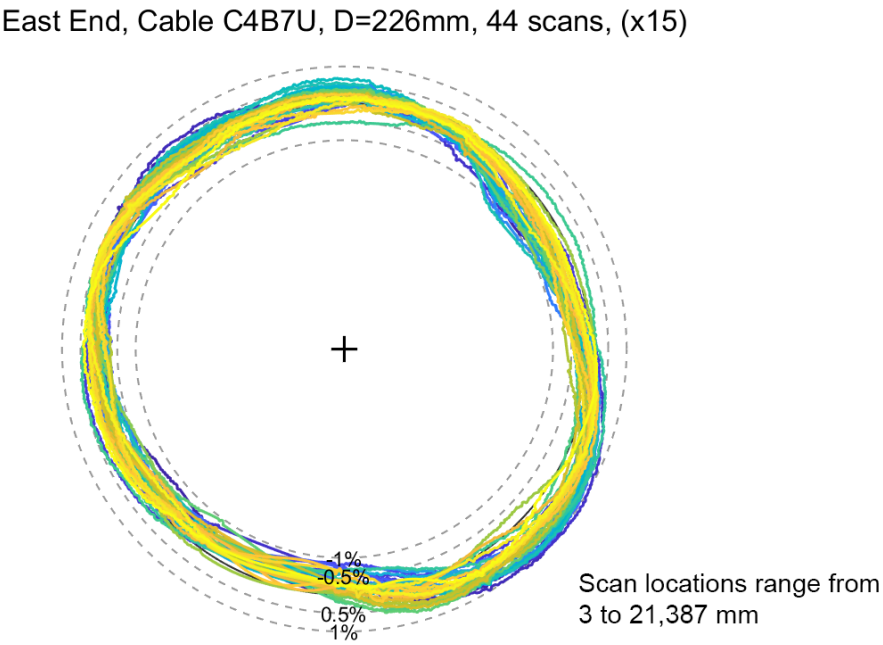

Source: FHWA.

Figure 70. Graph. Percent deviation from the mean plot for cable C4B7U on the East End Bridge.

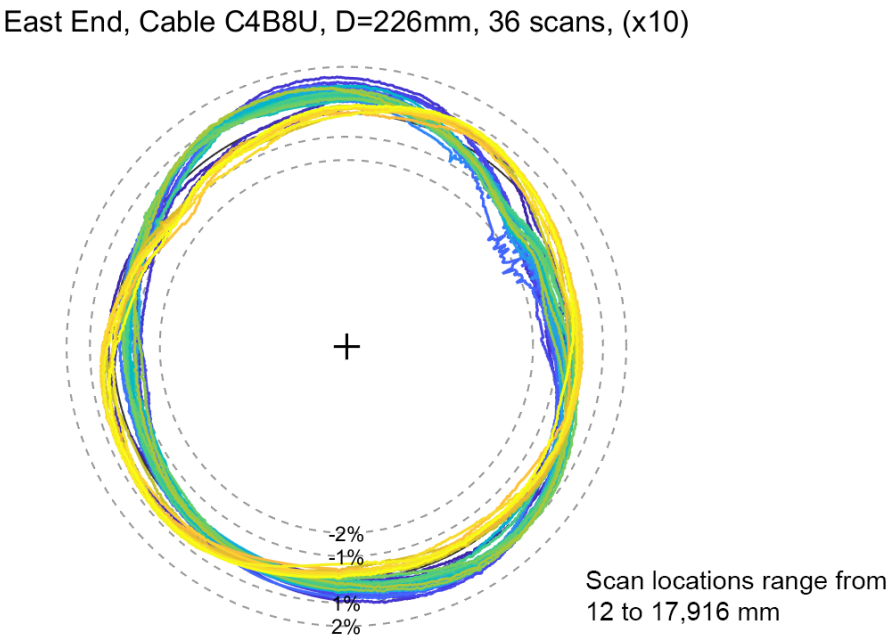

Source: FHWA.

Figure 71. Graph. Percent deviation from the mean plot for cable C4B8U on the East End Bridge.

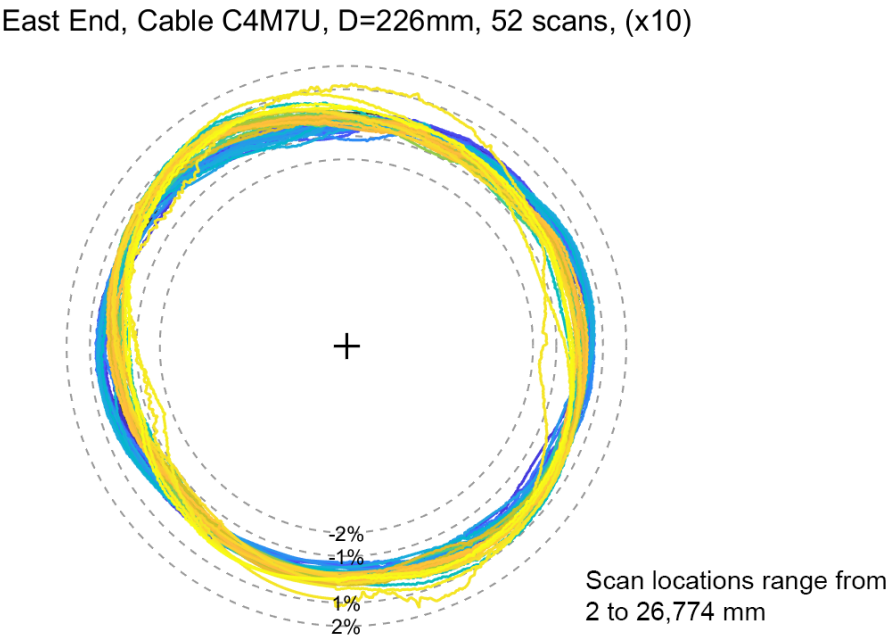

Source: FHWA.

Figure 72. Graph. Percent deviation from the mean plot for cable C4M7U on the East End Bridge.

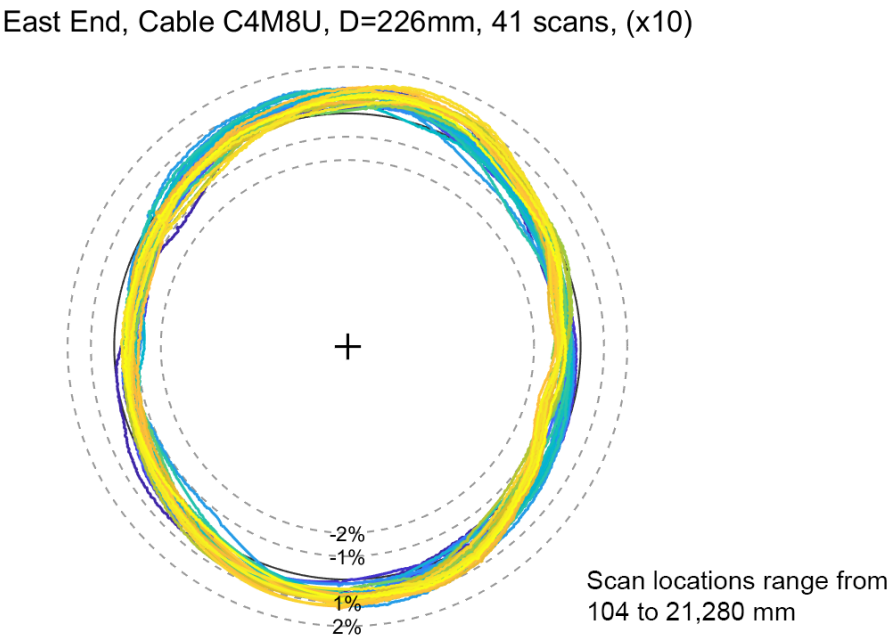

Source: FHWA.

Figure 73. Graph. Percent deviation from the mean plot for cable C4M8U on the East End Bridge.

The results from this set of tests produced some interesting cable shapes, but one of the more important findings is that—for the first time during testing—it was clear that the cable's shape might be changing between sections or at least rotating by a certain degree. Cable C4B8U had two distinct clusters of cable shapes, one circular and the other oval. These clusters match the cable section change that occurred at 13,339 mm up the cable. These groupings are annotated in figure 74. Similarly, cable C4M7U appears to go through a similar change at 12,417 mm, although the shift isn't as visibly obvious.

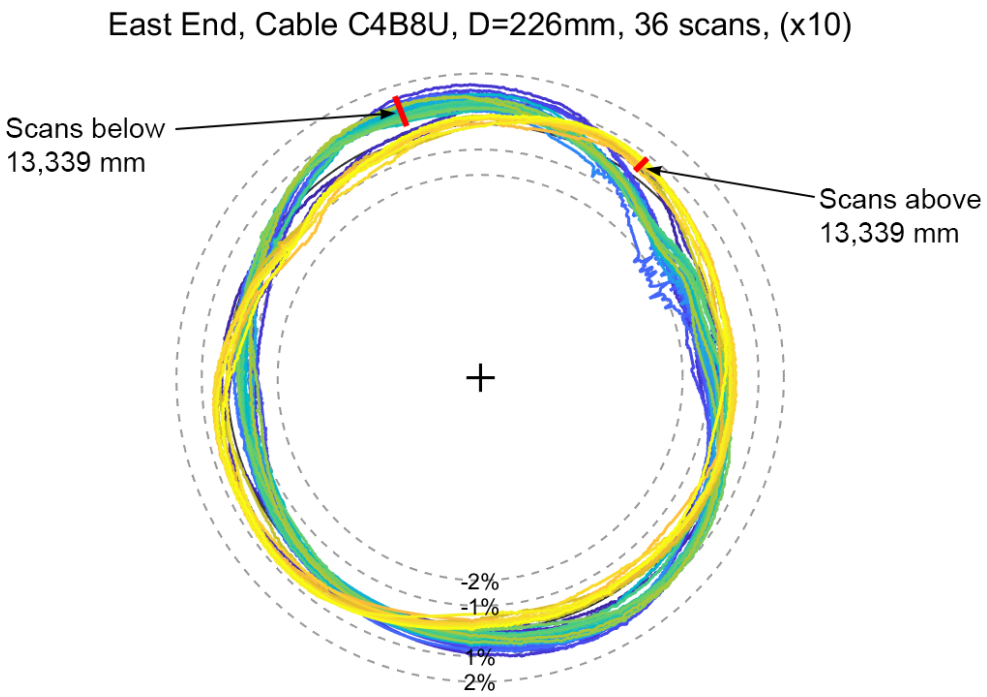

Source: FHWA.

Figure 74. Graph. Comparison of scans above and below 13,339 mm on cable C4B8U.

CHAPTER 11. ROBERT N. STEWART BRIDGE TESTING

FIELD TESTS

The Robert N. Stewart Bridge, which carries a single direction (eastbound) of State Route 46 traffic over the Flatrock River, is a smaller cable-stayed bridge in Columbus, IN. The bridge has a main span of 141.7 m, and the cross section has 1.97-m wide sidewalks on either side of the roadway behind traffic barriers. The tower consists of four large steel columns that are inclined to form a pyramid-shaped structure supporting 20 cables on each side of the roadway. This bridge was the second one tested where the cables are interconnected with crossties. Each set of 20 cables has a single line of crossties forming an arc in the upper third of the cable height, and these crossties did not restrict movement of the cable robot in any way. The cables are anchored to the outer portion of the bridge deck section between each traffic barrier and sidewalk. A photo of the bridge spanning the Flatrock River is shown in figure 75.

Source: FHWA.

Figure 75. Photo. The Robert N. Stewart Bridge in Columbus, IN.

A single day of testing on the Robert N. Stewart Bridge was completed in early December 2016, directly after the completion of the East End Bridge testing. The evening before, new clamp bracket heads were installed to account for the bridge's smaller cables. It was noted that the HDPE pipe on these cables was smooth and had no helical fillet. The cables' anchorages are located on the exterior of the roadway, protected by a concrete barrier and alongside a sidewalk area, which provided ample space to set up the test equipment. Photos of the test area and equipment are shown in figure 76 and figure 77. Table 13 contains a summary of all the testing.

Source: FHWA.

Figure 76. Photo. The robot climbing a cable from the Robert N. Stewart Bridge.

Source: FHWA.

Figure 77. Photo. The test equipment setup at Robert N. Stewart Bridge.

Table 13. Summary of Robert N. Stewart Bridge testing.

Date	Cable	No. of Measurements	Maximum Distance (mm)
12/7/2016	E8D	22	10,798
12/7/2016	E9D	24	11,764
12/6/2016	E10D	2	262

ANALYSIS AND RESULTS

Data from testing was processed using the custom software described in chapter 3. The gaps in the data surrounding the hinge were filled in using polynomial curve fitting, then the data was centered, and the mean, maximum, and minimum radii were calculated for each laser. The resulting data was saved in multiple data file formats.

The out-of-roundness percentage was calculated for each cable scan using equation 1. Table 14 contains a summary of the results from field testing where the mean, maximum, and minimum radii are averaged from all scans for each cable measured.

Table 14. Averaged cable radius data from laser 2 for the Robert N. Stewart Bridge.

Cable	No. of Measurements	Maximum Distance (m)	Mean Radius (mm)	Maximum Radius (mm)	Minimum Radius (mm)	Out-of-Roundness (percent)
E8D	22	10.8	55.83	57.05	54.69	4.2
E9D	24	11.8	55.73	56.29	55.23	1.9
E10D	2	0.3	56.00	56.82	55.05	3.2

The out-of-roundness for these cables varied from 1.9–4.2 percent, which was slightly higher compared to all cables tested for the project thus far. It should be noted that the cables had some of the smallest diameters tested for this project, and the laser's readings should be considered slightly less accurate because they were calibrated for larger cables.

Visualization plots were produced that overlaid all the cross-sectional scans from an individual cable to help identify the cable's general shape and compare how that shape varied along the cable. The cross sections were normalized by the cable's mean diameter and then the deviation from zero was shown by percentage. The plots were exaggerated by a factor of 10 to make slight deviations more visible. Figure 78 through figure 80 contain the visualization plots for the three cables tested at Robert N. Stewart Bridge. A note contains the range of distances up the cable where the scans were taken, measured either from the anchorage or the end of a guide pipe.

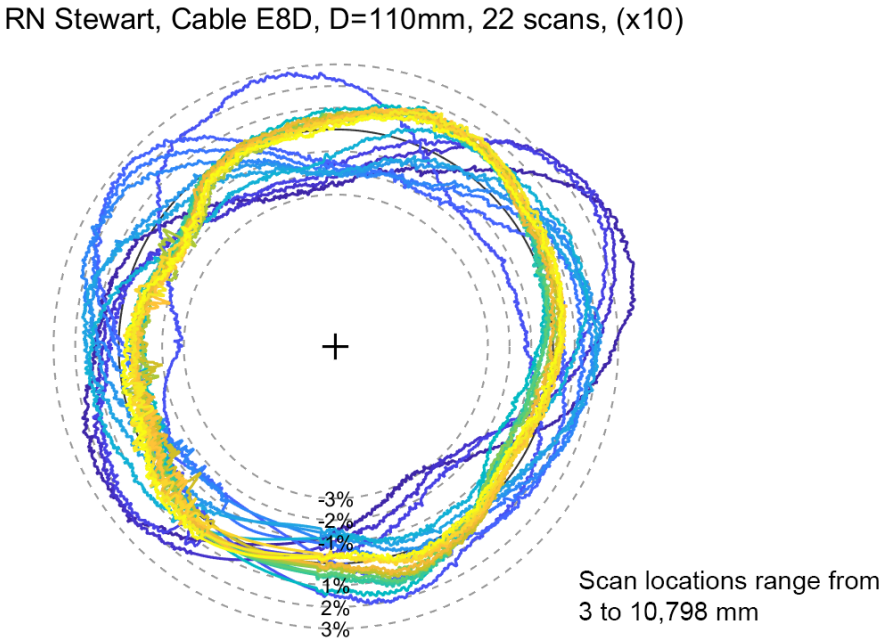

Source: FHWA.

Figure 78. Graph. Percent deviation from the mean plot for cable E8D on the Robert N. Stewart Bridge.

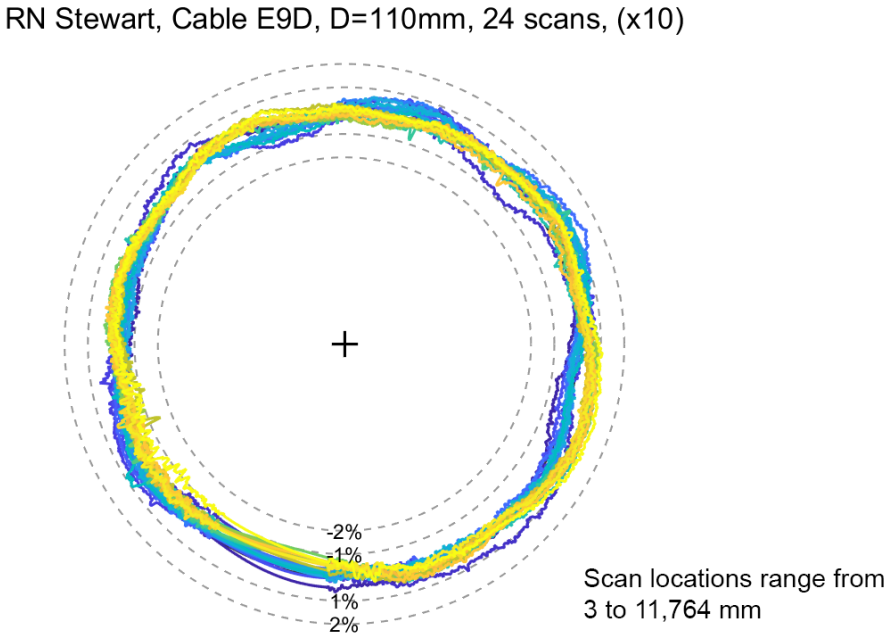

Source: FHWA.

Figure 79. Graph. Percent deviation from the mean plot for cable E9D on the Robert N. Stewart Bridge.

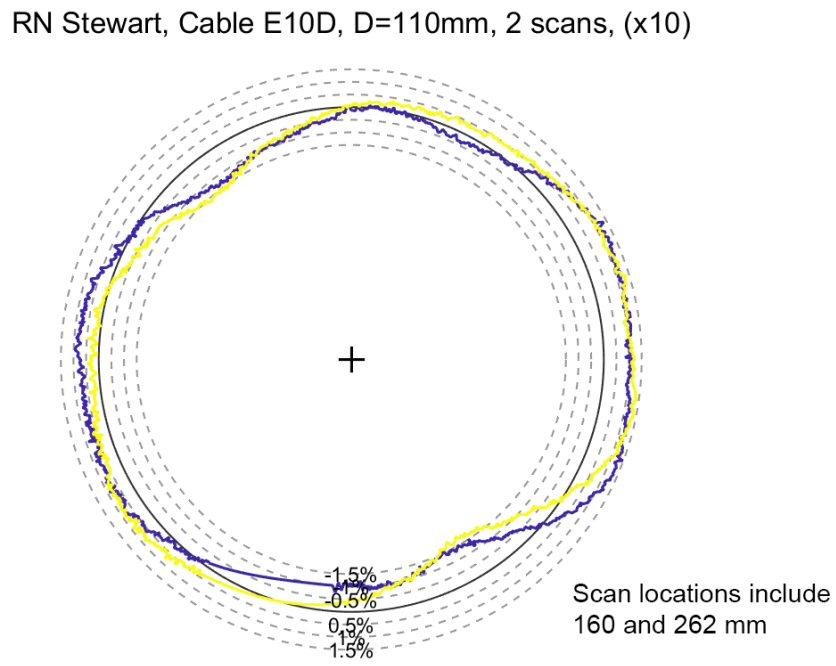

Source: FHWA.

Figure 80. Graph. Percent deviation from the mean plot for cable E10D on the Robert N. Stewart Bridge.

These plots immediately show much more noise in the cable scans compared to the scans for the other bridges. The most likely cause is the smaller diameter of the cables, which results in a greater relative error because the laser travels a longer distance to make the measurement. The laser carriage was calibrated to be most accurate between cable diameters of 154–200 mm, and these cables had diameters around 110 mm. The data could be averaged more to help smooth out the signal.

The two cables with the most measurements, E8D and E9D, vary greatly in their respective plots. The scans taken lower on cable E8D (below 4,100 mm) exhibit a large amount of randomness regarding the shapes. The lowest scans appear to be flattened ovals where the radius exceeds 3 percent of the mean. The shapes become more circular until they begin to approximate a hexagonally shaped circle for the upper cable measurements. For cable E9D, the shapes are much more consistent along the length of the cable, also approximating a circle but with multiple dents along the perimeter.

CHAPTER 12. LANE AVENUE BRIDGE TESTING

FIELD TESTS

The Lane Avenue Bridge is a smaller cable-stayed bridge in Columbus, OH, that carries six lanes of traffic across the Olentangy River near Ohio State University. The bridge has two 56.4-m spans, and the cross section has large 4.15-m wide sidewalks on either side of the roadway behind traffic barriers. The bridge features a pair of 44.2-m tall concrete pylons on either side of the roadway carrying 10 cables per pylon. The cables have an HDPE pipe with helical fillet. The cable anchorages rest in a large sidewalk area on both sides of the roadway, protected by a concrete traffic barrier. A photo of the bridge is shown in figure 81.

Source: FHWA.

Figure 81. Photo. The Lane Avenue Bridge.

Testing on the Lane Avenue Bridge occurred in mid-July 2017 and lasted one week. During testing, it was observed that the HDPE pipe on at least one stay cable exhibited a strange side-to-side deformation (see figure 82) near the upper end. The cables featured 3.048-m-long anti-vandalism steel guide pipes, which required the use of scaffolding for mounting the robot past the pipes. Fortunately, the wide, protected sidewalks on the bridge provided ample space to set up the scaffolding and test equipment. A photo of the test area at the bridge is shown in figure 83, featuring the anti-vandalism guide pipe and scaffolding in the foreground. Table 15 contains a summary of all the testing.

Source: FHWA.

Figure 82. Photo. Deformations in HDPE pipe on one of the stay cables.

Source: FHWA.

Figure 83. Photo. The test setup at the Lane Avenue Bridge.

Table 15. Summary of Lane Avenue Bridge testing.

Date	Cable	No. of Measurements	Maximum Distance (mm)
7/12/2017	SW1	24	12,094
7/12/2017	SW2	21	10,394
7/14/2017	NW1	32	15,883
7/15/2017	SE1	32	15,618
7/15/2017	SE2	26	12,384
7/16/2017	NW2	34	16,937

ANALYSIS AND RESULTS

Data from testing was processed using the custom software described in chapter 3. The gaps in the data surrounding the hinge were filled in using polynomial curve fitting, then the data was centered, and the mean, maximum, and minimum radii were calculated for each laser. The resulting data was saved in multiple data file formats.

The out-of-roundness percentage was calculated for each cable scan using equation 1. Table 16 contains a summary of the results from field testing where the mean, maximum, and minimum radii are averaged from all scans from each cable measured.

Table 16. Averaged cable radius data from laser 2 for the Lane Avenue Bridge.

Cable	No. of Measurements	Maximum Distance (m)	Mean Radius (mm)	Maximum Radius (mm)	Minimum Radius (mm)	Out-of-Roundness (percent)
NW1	32	15.9	70.01	70.66	69.26	2.0
NW2	34	16.9	70.06	70.66	69.46	1.7
SE1	31	15.6	70.09	70.70	69.53	1.7
SE2	26	12.4	70.14	70.74	69.52	1.7
SW1	24	12.1	70.02	70.58	69.40	1.7
SW2	21	10.4	70.17	70.73	69.57	1.6

The out-of-roundness for these cables varied from 1.6–2.0 percent, which was average among cables tested during this project. The cable diameters were the second smallest among those tested; only the Robert N. Stewart Bridge cables were smaller.

Visualization plots were produced that overlaid all the cross-sectional scans from an individual cable to help identify the cable's general shape and compare how that shape varied along the cable. The cross sections were normalized by the cable's mean diameter, and then the deviation from zero was shown by percentage. The plots were exaggerated by a factor of 10 to make slight deviations more visible. Figure 84 through figure 89 contain the visualization plots for the six cables tested at Lane Avenue Bridge. A note contains the range of distances up the cable where the scans were taken, measured either from the anchorage or the end of a guide pipe.

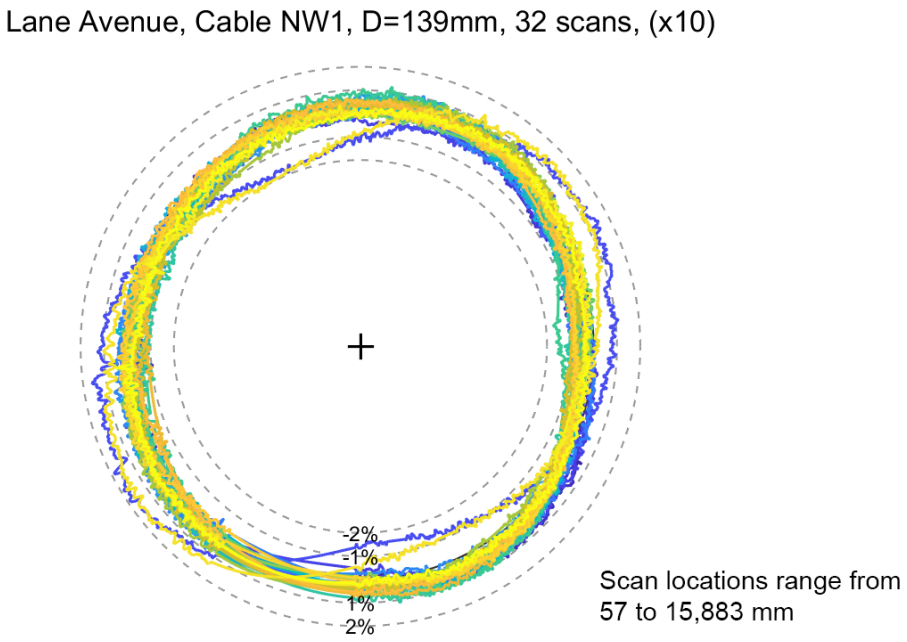

Source: FHWA.

Figure 84. Graph. Percent deviation from the mean plot for cable NW1 on the Lane Avenue Bridge.

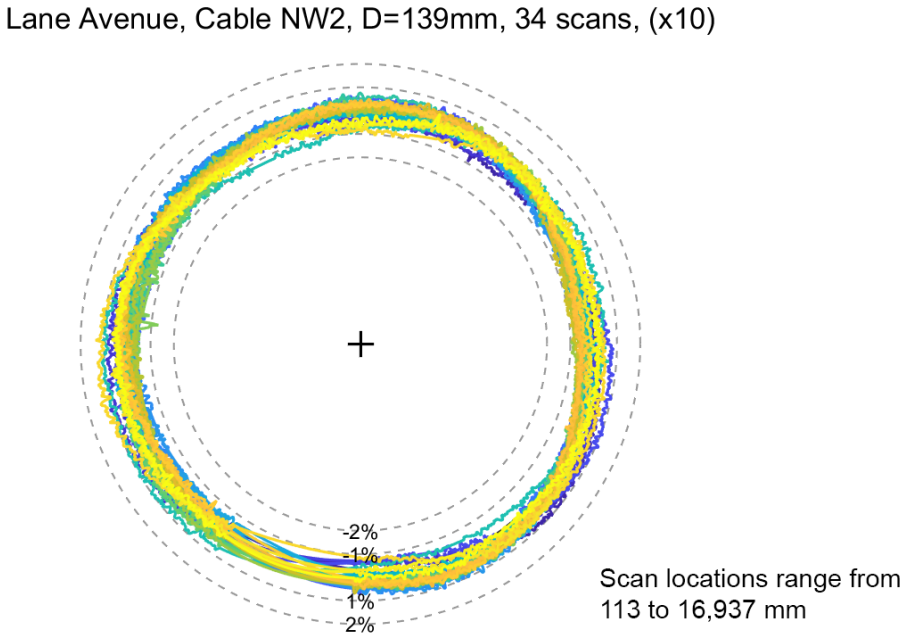

Source: FHWA.

Figure 85. Graph. Percent deviation from the mean plot for cable NW2 on the Lane Avenue Bridge.

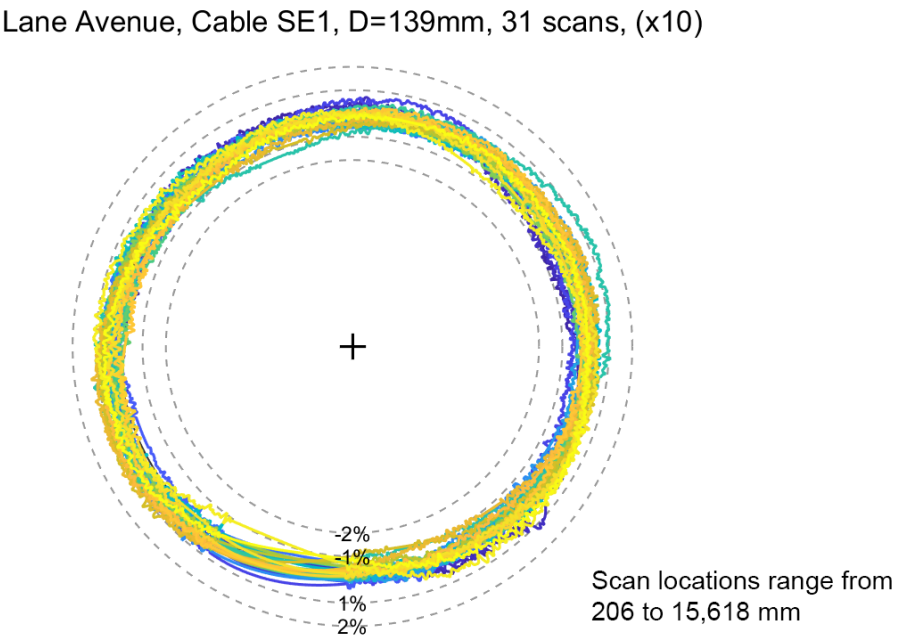

Source: FHWA.

Figure 86. Graph. Percent deviation from the mean plot for cable SE1 on the Lane Avenue Bridge.

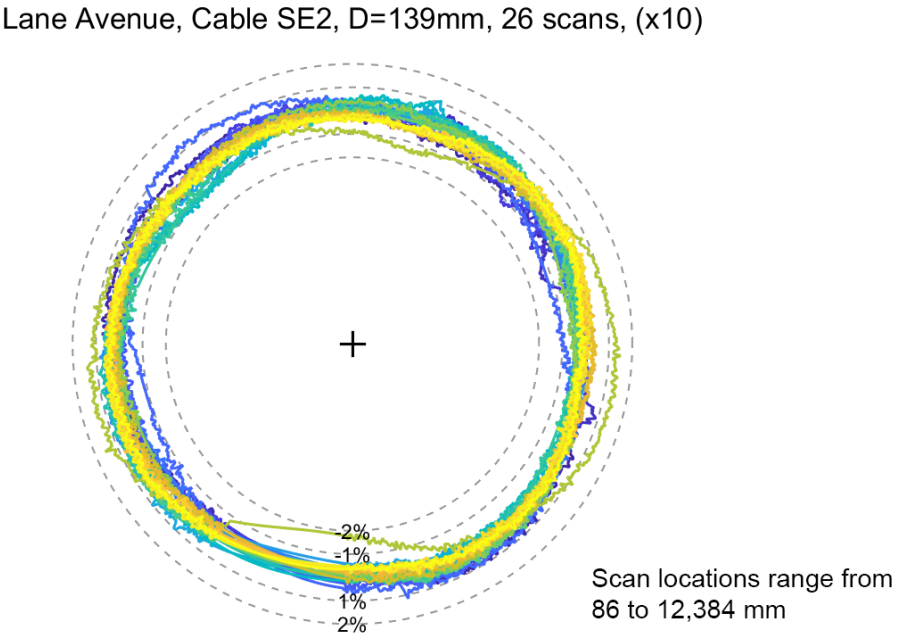

Source: FHWA.

Figure 87. Graph. Percent deviation from the mean plot for cable SE2 on the Lane Avenue Bridge.

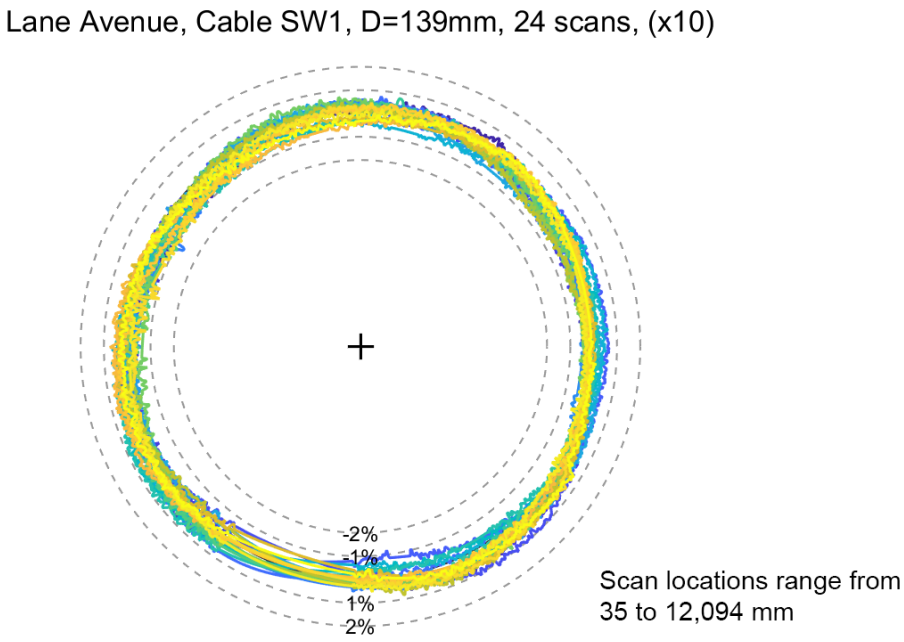

Source: FHWA.

Figure 88. Graph. Percent deviation from the mean plot for cable SW1 on the Lane Avenue Bridge.

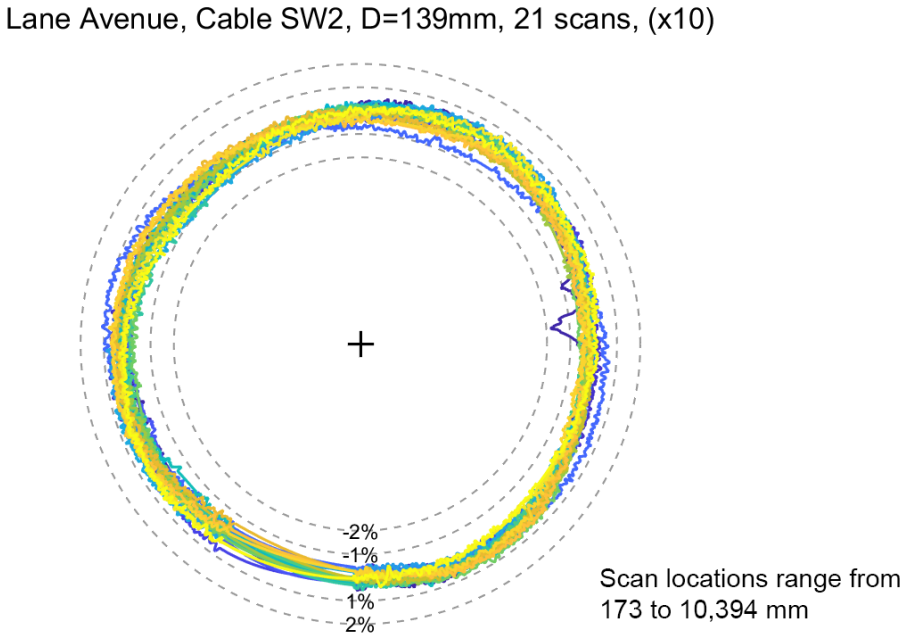

Source: FHWA.

Figure 89. Graph. Percent deviation from the mean plot for cable SW2 on the Lane Avenue Bridge.

Similar to the Robert N. Stewart Bridge cable scans, the scans for Lane Avenue all exhibit a lot of noise, which is likely due to the effect on the laser measurements from the smaller cable diameter. Except for cable NW1, the cable scans are very consistent along each individual cable. The scans also tend to be fairly round in shape, with some cables showing a four-sided bowed circular shape.

CHAPTER 13. POMEROY-MASON BRIDGE TESTING

FIELD TESTS

The Pomeroy-Mason Bridge, officially known as the Bridge of Honor, is a long-span, cable-stayed bridge connecting Pomeroy, OH, and Mason, WV, and carrying State Route 833 over the Ohio River. The bridge has a main span of 205.7 m, side spans of 74.4 m, and a 1.52-m walkway/bike path on the upriver side. Similar to the Ironton-Russell Bridge, the Pomeroy-Mason Bridge features two 75.7-m tall diamond-shaped towers supporting a main span and two side spans, with each tower carrying 24 cables anchored on each side of the deck. Two concrete traffic barriers with steel truck rails border the four-lane highway. A photo of the bridge is shown in figure 90.

Source: FHWA.

Figure 90. Photo. The Pomeroy-Mason Bridge.

Testing on the Pomeroy-Mason Bridge occurred in mid-August 2017 and lasted for one week. The cable anchorages are located between the outer edge of the deck section and the steel pipe fence (pedestrian railing) along the outer edge of sidewalk area. The anchorages feature a short guide pipe with a collar attached to a damper anchored to the bridge deck, but the measurable section of the cable was accessible without using scaffolding. A photo of the tower taken from the bridge's sidewalk is shown in figure 91, and the test setup is shown in figure 92. Table 17 contains a summary of all the testing.

Source: FHWA.

Figure 91. Photo. A tower of the Pomeroy-Mason Bridge, as seen from the sidewalk.

Source: FHWA.

Figure 92. Photo. The test setup for the Pomeroy-Mason Bridge on the sidewalk.

Table 17. Summary of Pomeroy-Mason Bridge testing.

Date	Cable	No. of Measurements	Maximum Distance (mm)
8/16/2017	B21U	31	15,581
8/16/2017	B22U	30	15,724
8/17/2017	B20U	29	14,469
8/18/2017	M21U	28	13,292
8/18/2017	M22U	17	9,296
8/19/2017	M10U	20	10,510
8/19/2017	M11U	32	16,972
8/20/2017	M19U	21	10,623
8/20/2017	M20U	32	16,341

ANALYSIS AND RESULTS

Data from testing was processed using the custom software described in chapter 3. The gaps in the data surrounding the hinge were filled in using polynomial curve fitting, then the data was centered, and the mean, maximum, and minimum radii were calculated for each laser. The resulting data was saved in multiple data file formats.

The out-of-roundness percentage was calculated for each cable scan using equation 1. Table 18 contains a summary of the results from field testing where the mean, maximum, and minimum radii are averaged from all scans from each cable measured.

Table 18. Averaged cable radius data from laser 2 for the Pomeroy-Mason Bridge.

Cable	No. of Measurements	Maximum Distance (m)	Mean Radius (mm)	Maximum Radius (mm)	Minimum Radius (mm)	Out-of-Roundness (percent)
B20U	29	14.5	80.60	81.28	79.74	1.9
B21U	31	15.6	80.81	81.44	80.07	1.7
B22U	30	15.7	80.55	81.12	79.86	1.6
M10U	20	10.5	90.57	91.08	89.87	1.3
M11U	32	17.0	90.39	91.02	89.74	1.4
M19U	21	10.6	80.79	81.35	80.13	1.5
M20U	32	16.3	80.58	81.15	79.84	1.6
M21U	28	13.3	80.68	81.32	79.95	1.7
M22U	17	9.3	90.57	91.16	89.86	1.4

The out-of-roundness for these cables varied from 1.3–1.9 percent, which was average among cables tested during this project and extremely consistent considering the large number of cables tested. This bridge shared similarities in both the tower shape and the cable diameters with the Ironton-Russell Bridge, although the Pomeroy-Mason Bridge cables were slightly rounder.

Visualization plots were produced that overlaid all the cross-sectional scans from an individual cable to help identify the cable's general shape and compare how that shape varied along the cable. The cross sections were normalized by the cable's mean diameter and then the deviation from zero was shown by percentage. The plots were exaggerated by a factor of 10 to make slight deviations more visible. Figure 93 through figure 101 contain the visualization plots for the nine cables tested at Pomeroy-Mason Bridge. A note contains the range of distances up the cable where the scans were taken, measured either from the anchorage or the end of a guide pipe.

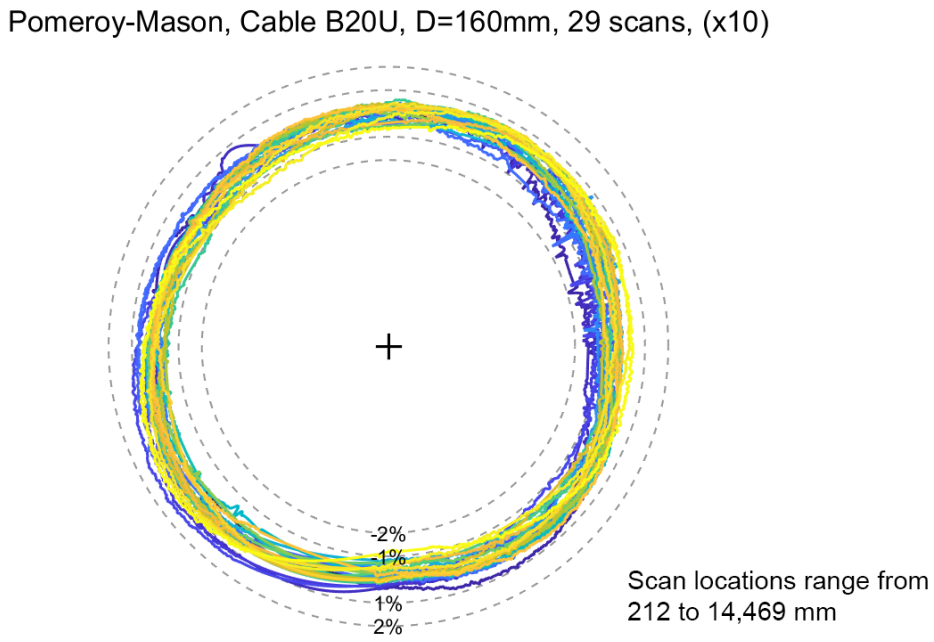

Source: FHWA.

Figure 93. Graph. Percent deviation from the mean plot for cable B20U on the Pomeroy-Mason Bridge.

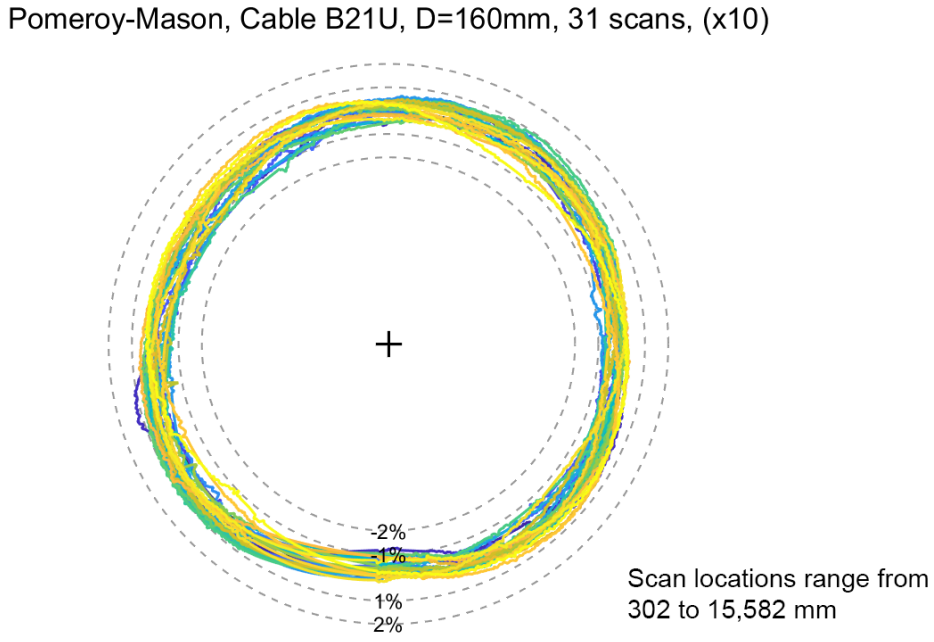

Source: FHWA.

Figure 94. Graph. Percent deviation from the mean plot for cable B21U on the Pomeroy-Mason Bridge.

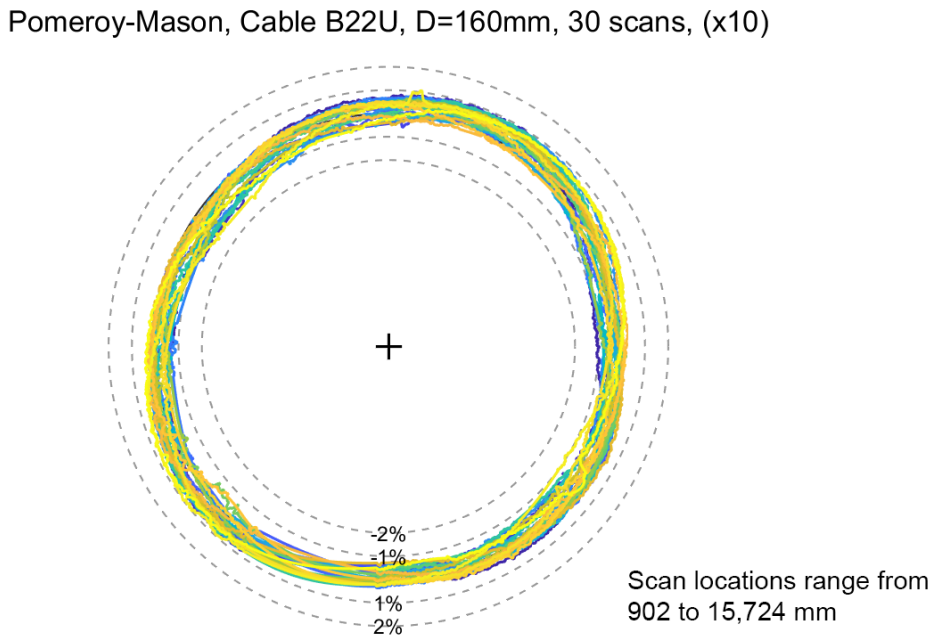

Source: FHWA.

Figure 95. Graph. Percent deviation from the mean plot for cable B22U on the Pomeroy-Mason Bridge.

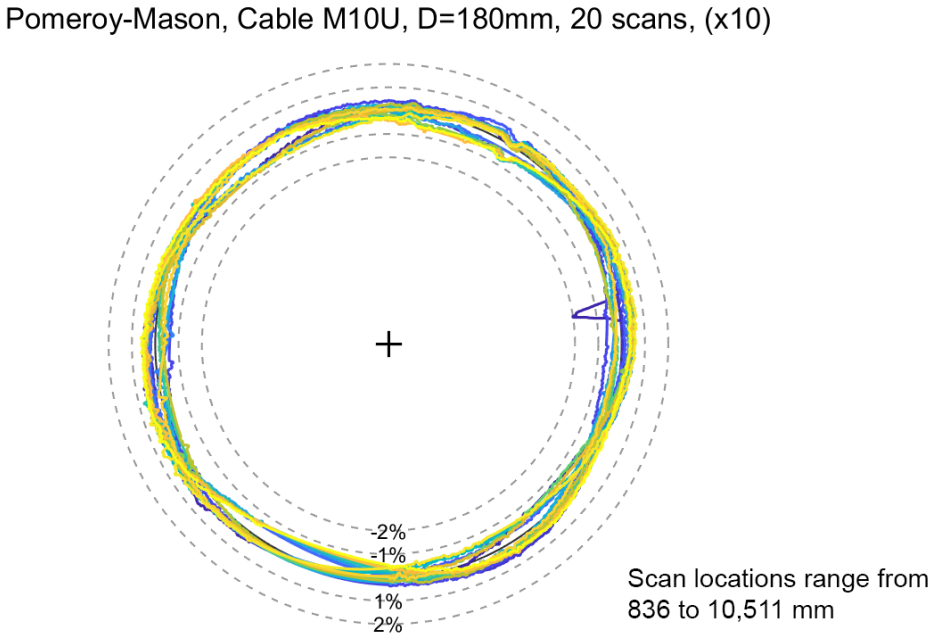

Source: FHWA.

Figure 96. Graph. Percent deviation from the mean plot for cable M10U on the Pomeroy-Mason Bridge.

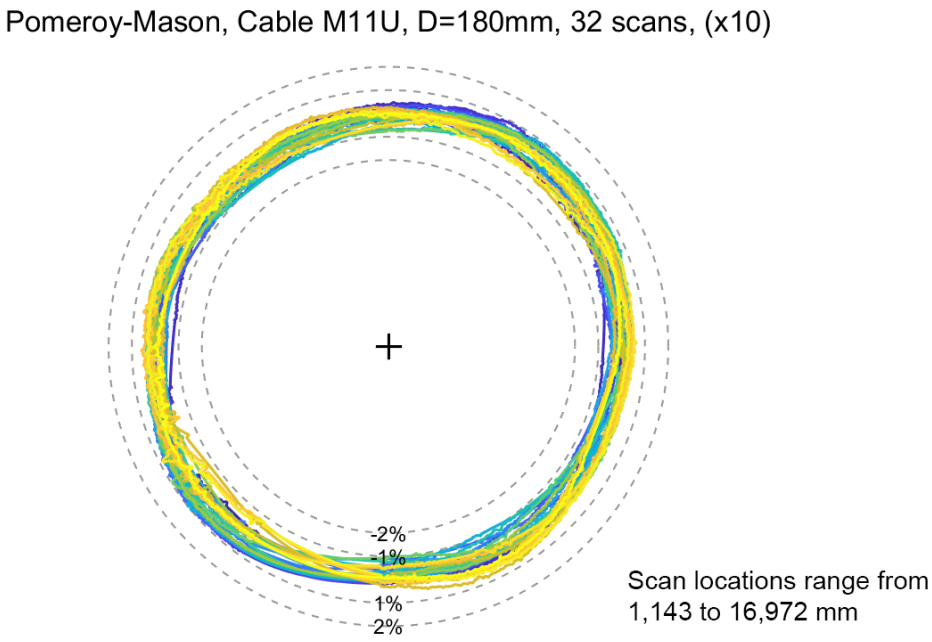

Source: FHWA.

Figure 97. Graph. Percent deviation from the mean plot for cable M11U on the Pomeroy-Mason Bridge.

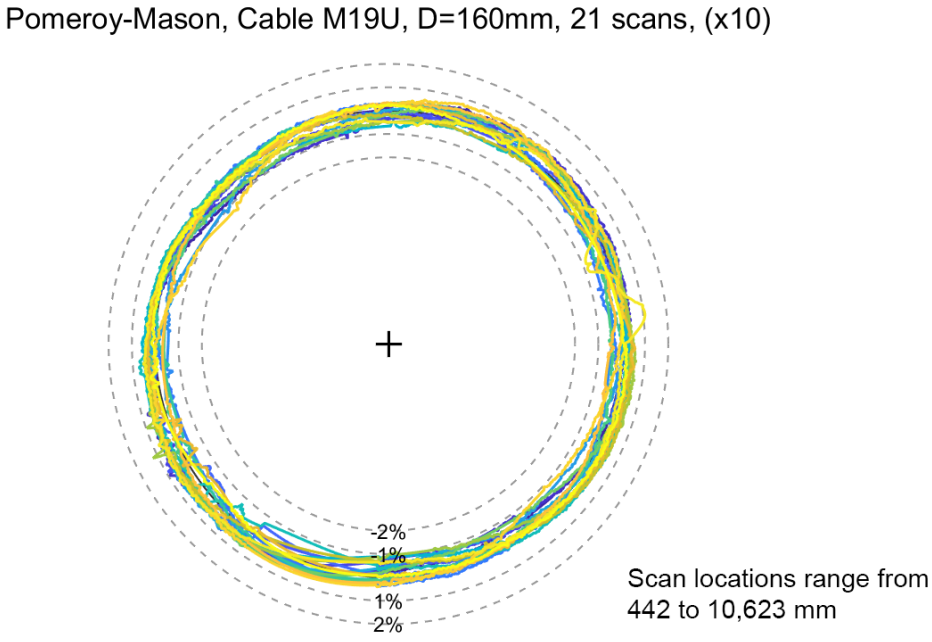

Source: FHWA.

Figure 98. Graph. Percent deviation from the mean plot for cable M19U on the Pomeroy-Mason Bridge.

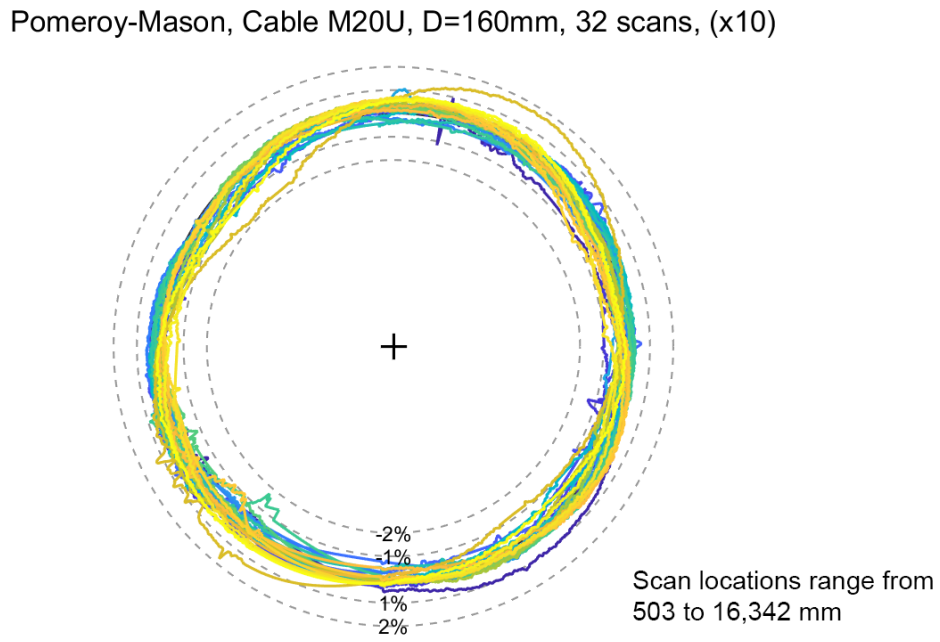

Source: FHWA.

Figure 99. Graph. Percent deviation from the mean plot for cable M20U on the Pomeroy-Mason Bridge.

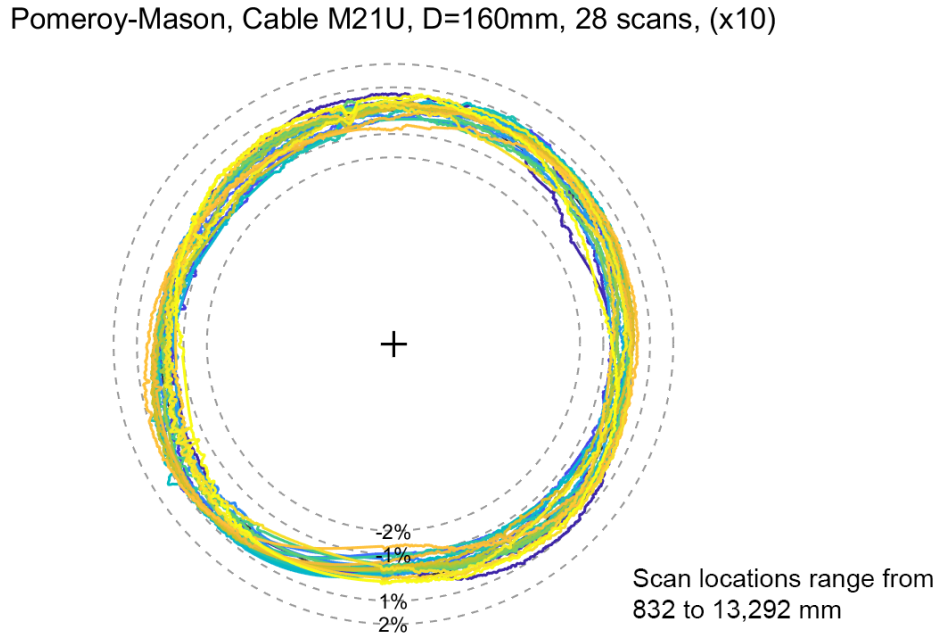

Source: FHWA.

Figure 100. Graph. Percent deviation from the mean plot for cable M21U on the Pomeroy-Mason Bridge.

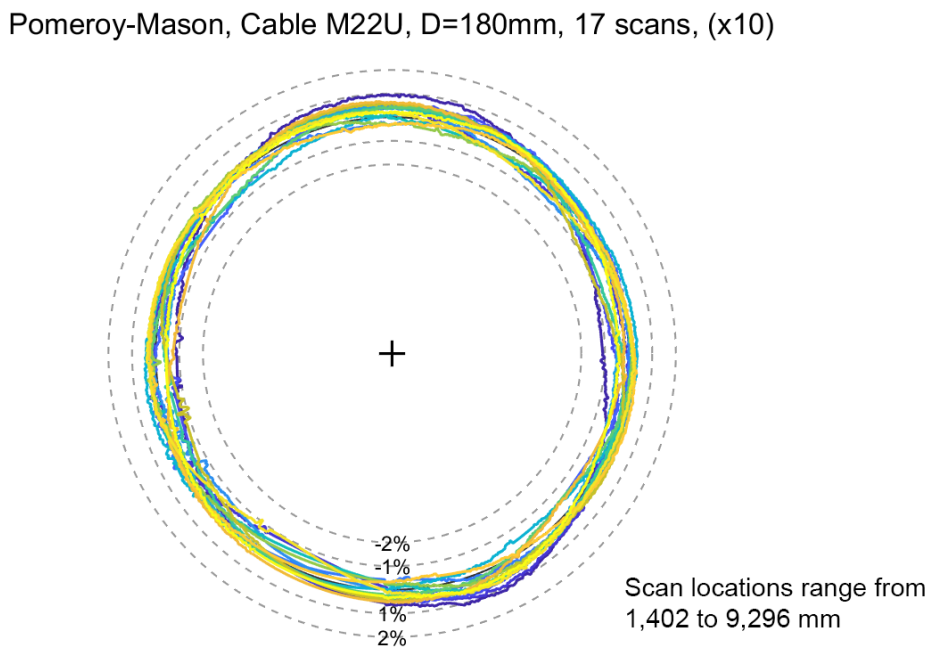

Source: FHWA.

Figure 101. Graph. Percent deviation from the mean plot for cable M22U on the Pomeroy-Mason Bridge.

The scans from testing show that these cables have mostly round shapes, but some of the scans contained measurable noise. During testing, it was observed that the cables were quite dirty, especially on the underside of the cable where rainwater rivulets tend to form and along the fillets themselves. A photo of the underside of a cable from the Pomeroy-Mason Bridge is shown in figure 102.

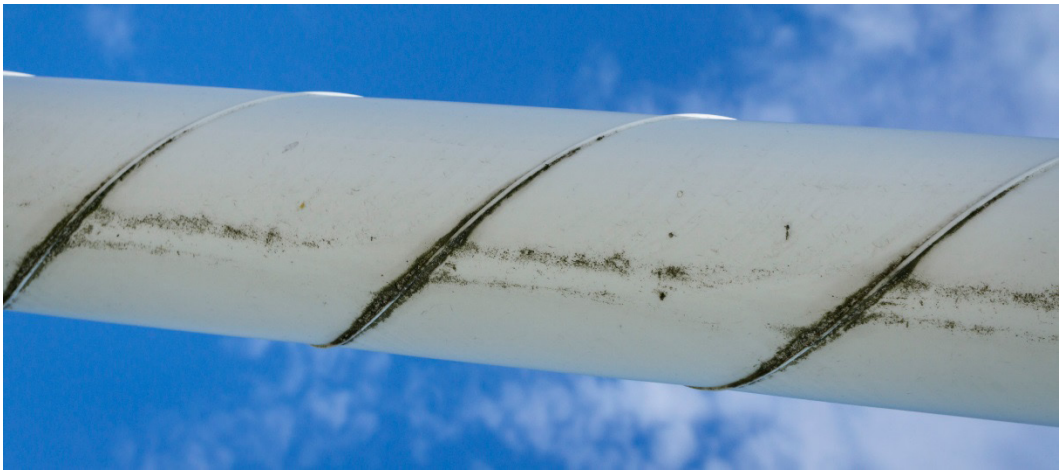

Source: FHWA.

Figure 102. Photo. Dirt collecting on the underside of a cable from the Pomeroy-Mason Bridge.

CHAPTER 14. WILLIAM H. HARSHA BRIDGE TESTING

FIELD TESTS

The William H. Harsha Bridge is a long-span cable-stayed bridge connecting Maysville, KY, and Aberdeen, OH, and carrying two lanes of traffic from U.S. Route 62 over the Ohio River. The bridge features two 93.0-m tall, H-shaped towers supporting a main span with a length of 320.0 m and two side spans with a length of 135.0 m. The bridge features 3.66-m wide shoulders on both sides bordered by a concrete barrier with a steel truck rail. The cable anchorages rest outside the traffic barriers and support the deck by attaching to the steel girders that comprise the exterior frame of the deck's substructure. Each H-shape tower supports 20 cable stays in each fan on both sides of the deck. A photo of the William H. Harsha Bridge, which opened to the public in October 2000, is shown in figure 103.

Source: FHWA.

Figure 103. Photo. The William H. Harsha Bridge.

Testing on the bridge occurred in late September 2017 and lasted for 1 week. Although the cable anchorages are positioned outside of the concrete barriers, the deck slab extended far enough past the barrier for the team to set up testing equipment and safely access the cables. The anchorages are angled steel beams that protrude through the deck slab connecting the deck girder to the cable. The cables are composed of the anchorage pipe, followed by a section of anti-vandalism guide pipe before transitioning to the HDPE pipe for the rest of the cable to the tower. Due to the height of the guide pipe, the scaffolding for mounting the robot about 1.83 m above deck level at the desired starting section of the cable. The test setup for the bridge is shown in figure 104 and figure 105. Table 19 contains a summary of all testing.

Source: FHWA.

Figure 104. Photo. An aerial view of the testing setup.

Source: FHWA.

Figure 105. Photo. A view of the testing setup from the bridge deck.

Table 19. Summary of William H. Harsha Bridge testing.

Date	Cable	No. of Measurements	Maximum Distance (mm)
9/25/2017	S1U	38	20,356
9/26/2017	M20U	47	25,226
9/27/2017	M21U	51	27,096
9/28/2017	S40U	51	27,714
9/29/2017	M19U	33	17,845

ANALYSIS AND RESULTS

Data from testing was processed using the custom software described in chapter 3. The gaps in the data surrounding the hinge were filled in using polynomial curve fitting, then the data was centered, and the mean, maximum, and minimum radii were calculated for each laser. The resulting data was saved in multiple data file formats.

The out-of-roundness percentage was calculated for each cable scan using equation 1. Table 20 contains a summary of the results from field testing where the mean, maximum, and minimum radii are averaged from all scans for each cable measured.

Table 20. Averaged cable radius data from laser 2 for the William H. Harsha Bridge.

Cable	No. of Measurements	Maximum Distance (m)	Mean Radius (mm)	Maximum Radius (mm)	Minimum Radius (mm)	Out-of-Roundness (percent)
M19U	33	17.8	113.97	114.53	113.30	1.1
M20U	47	25.2	114.10	114.71	113.41	1.1
M21U	51	27.1	114.21	114.79	113.53	1.1
S1U	38	20.4	114.09	114.76	113.36	1.2
S40U	51	27.7	114.14	114.81	113.38	1.3

The out-of-roundness for these cables varied only from 1.1–1.3 percent, which was the second roundest among HDPE cables tested during this project; only the U.S. Grant bridge cables were rounder. The cables on the William H. Harsha bridge were a little larger, with diameters about 28 mm bigger. The out-of-roundness percentage was also very consistent among the five cables tested.

Visualization plots were produced that overlaid all the cross-sectional scans from an individual cable to help identify the cable's general shape and compare how that shape varied along the cable. The cross sections were normalized by the cable's mean diameter and then the deviation from zero was shown by percentage. The plots were exaggerated by a factor of 15 to make slight deviations more visible. Figure 106 through figure 110 contain the visualization plots for the five cables tested at the William H. Harsha Bridge. A note contains the range of distances up the cable where the scans were taken, measured either from the anchorage or the end of a guide pipe.

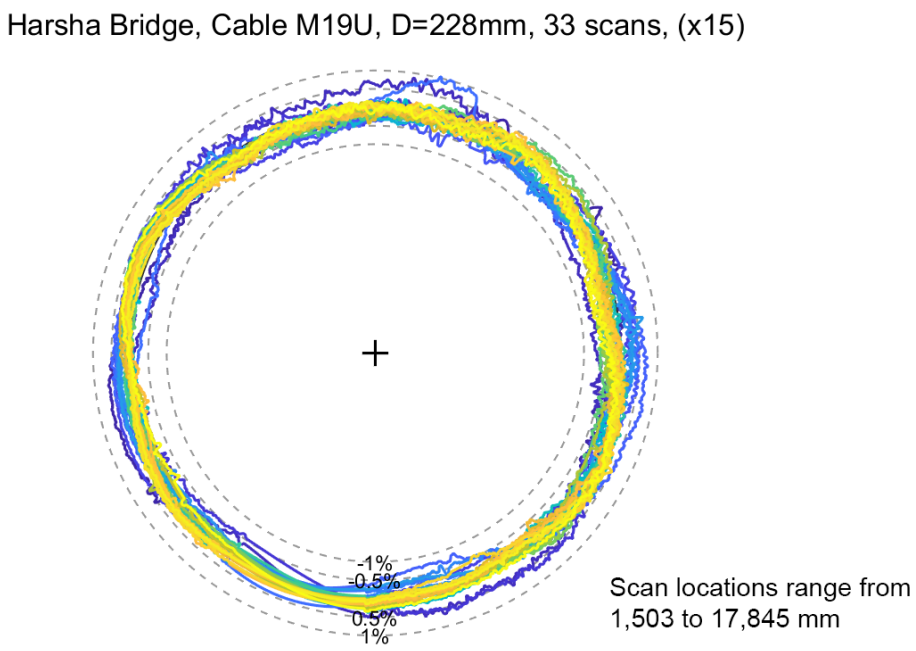

Source: FHWA.

Figure 106. Graph. Percent deviation from the mean plot for cable M19U on the William H. Harsha Bridge.

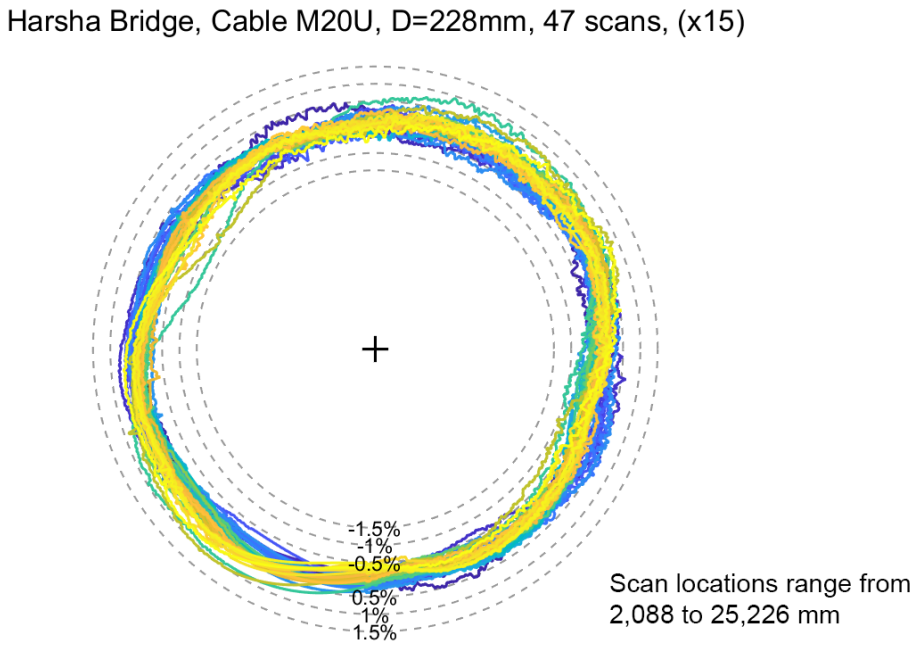

Source: FHWA.

Figure 107. Graph. Percent deviation from the mean plot for cable M20U on the William H. Harsha Bridge.

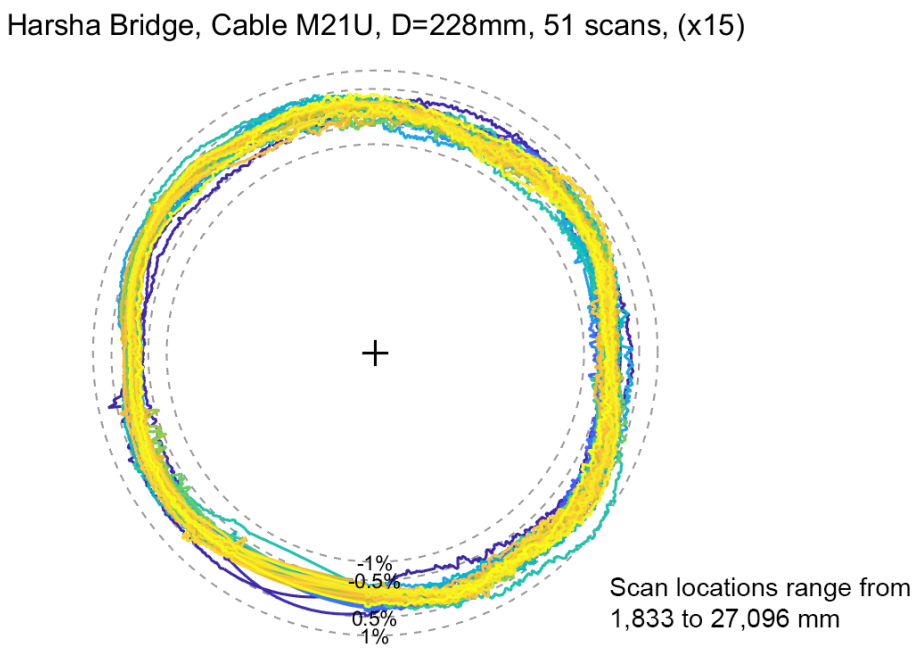

Source: FHWA.

Figure 108. Graph. Percent deviation from the mean plot for cable M21U on the William H. Harsha Bridge.

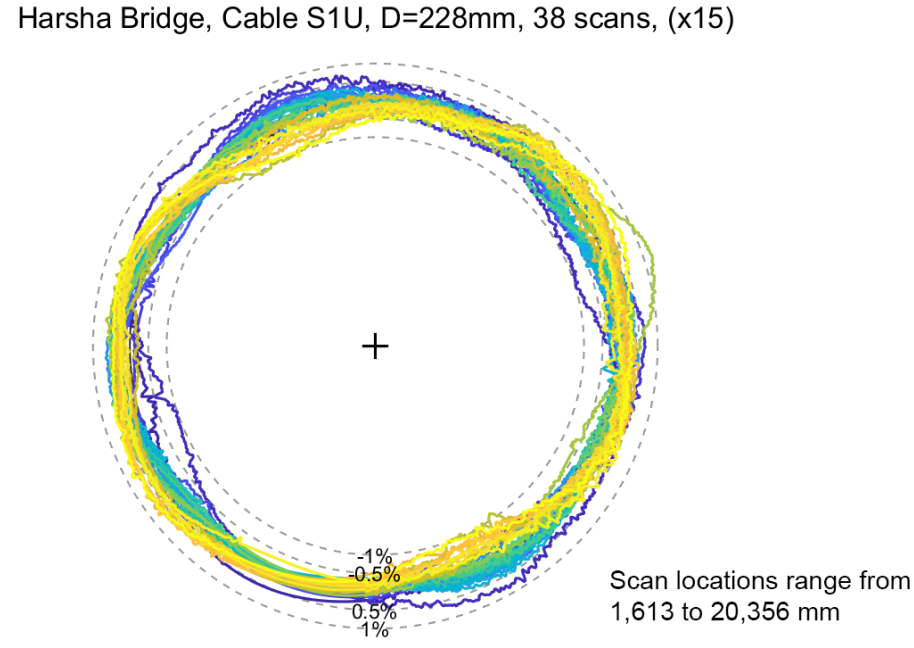

Source: FHWA.

Figure 109. Graph. Percent deviation from the mean plot for cable S1U on the William H. Harsha Bridge.

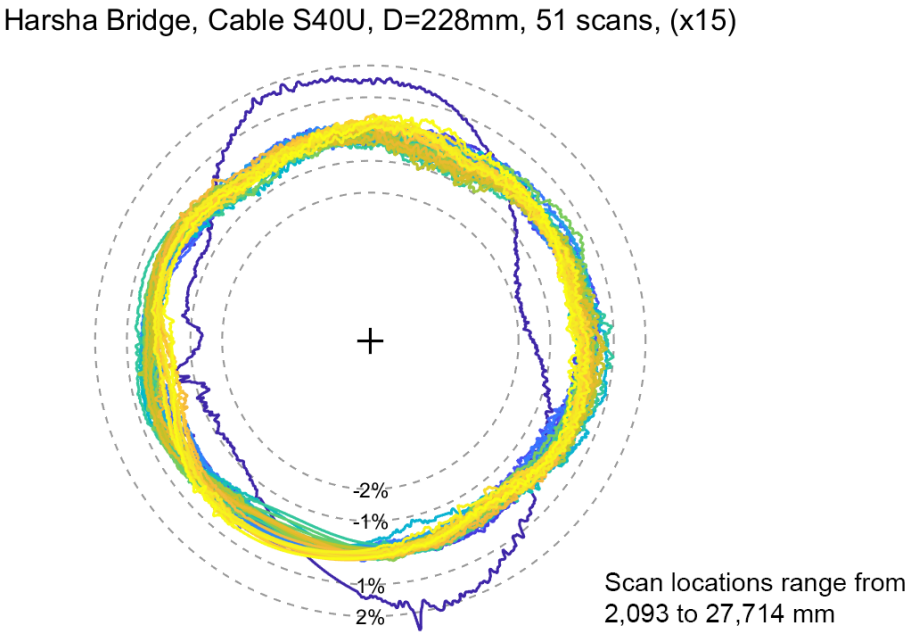

Source: FHWA.

Figure 110. Graph. Percent deviation from the mean plot for cable S40U on the William H. Harsha Bridge.

As expected from their out-of-roundness percentages, these cables' visualization plots are mostly round except for a few outlier measurements. It should be noted that the measurements experienced a measurable noise which could indicate that either the cables were dirty or otherwise presented a difficult surface to scan.

The first few measurements of each cable were on a short section that did not feature helical fillets. These initial sections varied between 2.5–2.7 m in length. The remaining sections of cable had a single helical fillet; all previous bridges tested had two helical fillets. During testing, it was observed that the cables were very dirty, especially on the underside of the HDPE pipe where rainwater rivulets tend to form on the cable. Streak lines were clearly visible (see figure 111) in the dirty surface film on the HDPE pipe, illustrating the flow of rainwater around and down the cable. Crazing was also observed (see figure 112) in selected small areas of the HDPE pipe.

Source: FHWA.

Figure 111. Photo. Rain flow patterns in dirt on the underside of a stay cable.

Source: FHWA.

Figure 112. Photo. Crazing on the surface of the HDPE pipe.

CHAPTER 15. ARTHUR RAVENEL BRIDGE TESTING

FIELD TESTS

The Arthur Ravenel Bridge is a long-span cable-stayed bridge connecting downtown Charleston, SC, with Mount Pleasant, SC, over the Cooper River. The bridge carries eight lanes of traffic from U.S. Route 17 and has a protected 3.66-m walkway/bikeway on the downstream side of the bridge. The bridge features two 175.3-m tall diamond-shaped towers supporting a main span with a length of 457.2 m, side spans of 198.1 m, and very long approach spans. Each fan consists of 32 cables with anchorages located above the bridge deck. In addition to a center concrete barrier, the bridge has two outer concrete traffic barriers to protect the cable anchorages from vehicular traffic. A photo of the Arthur Ravenel Bridge is shown in figure 113.

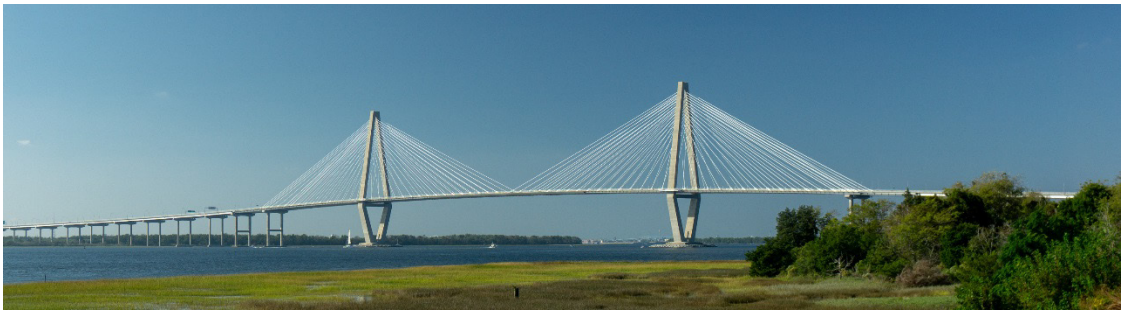

Source: FHWA.

Figure 113. Photo. The Arthur Ravenel Bridge.

Testing on this bridge occurred in mid-October 2017. The longest cables featured steel anchorages protruding from a concrete block while the remaining steel anchorages were mounted directly to the deck itself. Figure 114 shows the anchorage mounts at the center of the bridge. A large-diameter anchorage pipe that leads into a guide pipe protects the cables' attachment to the steel anchorage. For the longer cables, external dampers are attached to the guide pipe while the remaining cables feature a steel crossbar to help brace the anchorages to the deck. The robot was mounted above the anchorage, guide pipes, and dampers. Only cables on the downstream side were tested because the protected sidewalk area provided room to set up the scaffolding and the test equipment, Due to the extreme length of the bridge, a small, motorized cart was used to transport the testing equipment from the parking area to the test site. A photo of the test setup on the bridge's sidewalk showing the scaffolding is shown in figure 115. Table 21 contains a summary of all the testing.

Source: FHWA.

Figure 114. Photo. The anchorages and external dampers at the center of the main span of the bridge.

Source: FHWA.

Figure 115. Photo. The test setup on the sidewalk of the bridge.

Table 21. Summary of Arthur Ravenel Bridge testing.

Date	Cable	No. of Measurements	Maximum Distance (mm)
10/12/17	S58D	31	16,814
10/13/17	S57D	33	13,566
10/16/17	S55D	29	13,452
10/18/17	M39D	34	17,054

ANALYSIS AND RESULTS

Data from testing was processed using the custom software described in chapter 3. The gaps in the data surrounding the hinge were filled in using polynomial curve fitting, then the data was centered, and the mean, maximum, and minimum radii were calculated for each laser. The resulting data was saved in multiple data file formats.

The out-of-roundness percentage was calculated for each cable scan using equation 1. Table 22 contains a summary of the results from field testing where the mean, maximum, and minimum radii are averaged from all scans from each cable measured.

Table 22. Averaged cable radius data from laser 2 for the Arthur Ravenel Bridge.

Cable	No. of Measurements	Maximum Distance (m)	Mean Radius (mm)	Maximum Radius (mm)	Minimum Radius (mm)	Out-of-Roundness (percent)
M39D	34	17.1	113.44	115.47	111.12	3.8
S55D	29	13.5	100.82	101.98	99.45	2.5
S57D	33	13.6	113.59	115.52	111.08	3.9
S58D	31	16.8	113.68	115.52	111.69	3.4

The out-of-roundness for these cables varied from 2.5–3.9 percent, with three cables having an out-of-roundness over 3.4 percent. Although this bridge did not have the most out-of-round individual cable found during testing, these values taken as a group were the worst. The smaller, 200-mm diameter cable was noticeably less out-of-round than the others. The other three cables all had cable diameters of 226 mm.

Visualization plots were produced that overlaid all the cross-sectional scans from an individual cable to help identify the cable's general shape and compare how that shape varied along the cable. The cross sections were normalized by the cable's mean diameter and then the deviation from zero was shown by percentage. The plots were exaggerated by a factor of 10 to make slight deviations more visible. Figure 116 through figure 119 contain the visualization plots for the four cables tested at the Arthur Ravenel Bridge. A note contains the range of distances up the cable where the scans were taken, measured either from the anchorage or the end of a guide pipe.

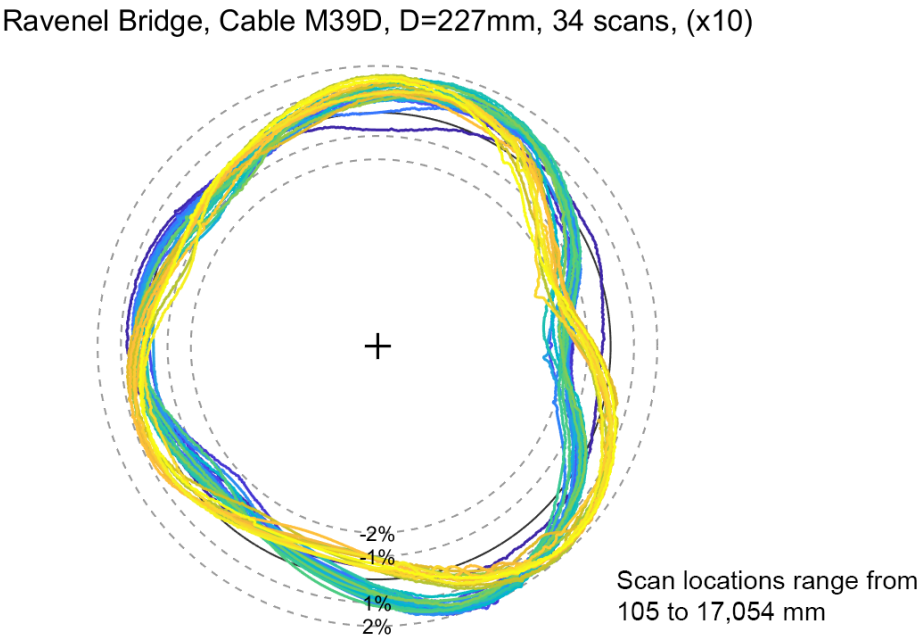

Source: FHWA.

Figure 116. Graph. Percent deviation from the mean plot for cable M39D on the Arthur Ravenel Bridge.

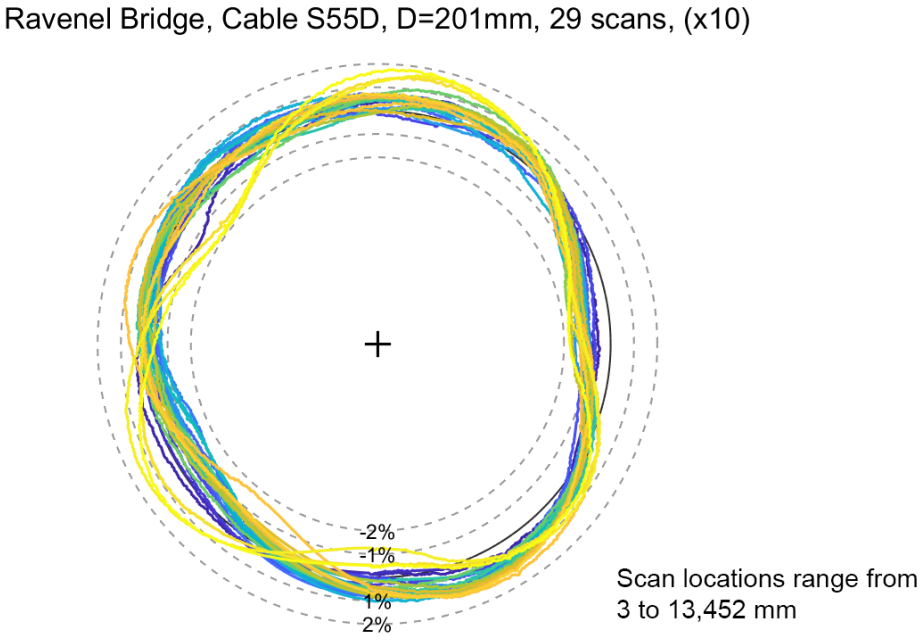

Source: FHWA.

Figure 117. Graph. Percent deviation from the mean plot for cable S55D on the Arthur Ravenel Bridge.

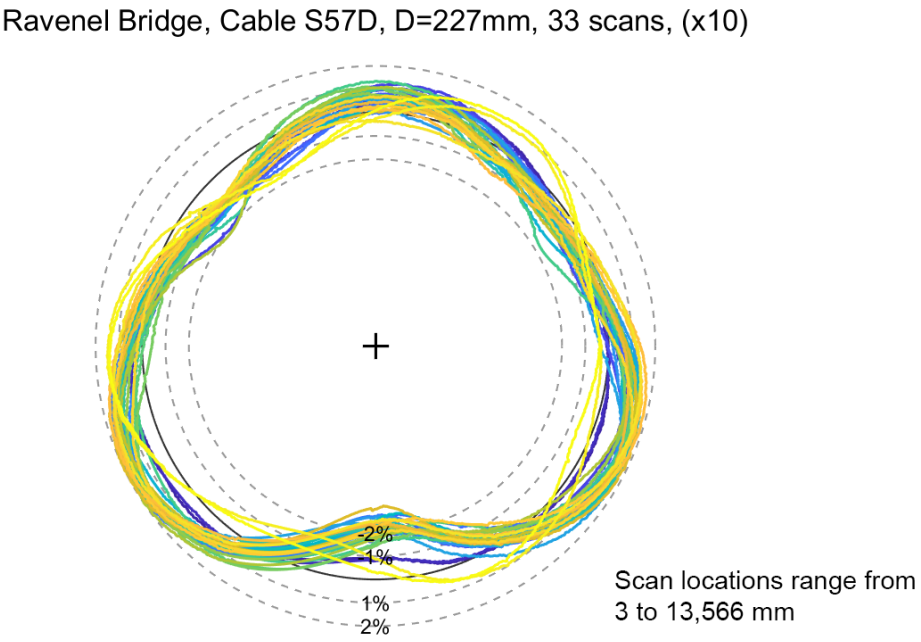

Source: FHWA.

Figure 118. Graph. Percent deviation from the mean plot for cable S57D on the Arthur Ravenel Bridge.

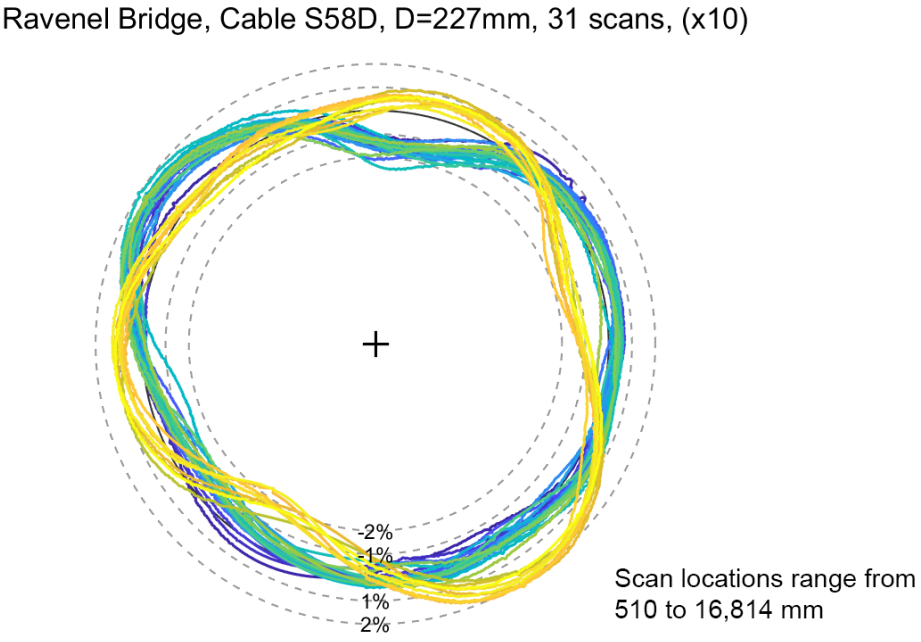

Source: FHWA.

Figure 119. Graph. Percent deviation from the mean plot for cable S58D on the Arthur Ravenel Bridge.

These visualization plots were some of the most interesting encountered during testing. All three of the larger cables feature a distinct shape that (when exaggerated by a factor of 10) looks somewhat heart shaped. Not only is this shape visible at different angles for each of the larger cables, but the shape also appears at different angles in the same cable, indicating that the sections of cable were not perfectly aligned when welded together during construction of the bridge. For cable M39D, this misalignment is about 10 degrees, but for cable S58D, the alignment is off by roughly 170 degrees. The smaller cable, S55D, also has an interesting shape. The robot took only three measurements of the second section of this cable, but the sections also appear to be misaligned.

CHAPTER 16. SUMMARY OF RESULTS

After the completion of 3 years of testing, 11 different bridge sites were visited and a total of 67 individual cables were tested, recording more than 1,700 roundness measurements. In 2015, the first year of testing, the average number of scans on a cable was 15, with the robot climbing to an average distance of 7 m. By the following year, the average number of scans per cable almost doubled to 28.3 scans, with the robot climbing to an average height of 14.9 m. In 2017, the last year of testing, the average number of scans per cable reached 31.5, with the robot climbing to an average height of 16.4 m. These increases were due to improvements in the design of the laser carriage and clamps and efficiencies in the programming.

Of the 11 different bridge sites, 4 were along the east coast; 5 were crossings of the Ohio River on the border of West Virginia, Ohio, and Kentucky; and the remaining 2 sites were small-span bridges located within a few hours' drive from an Ohio river. All the testing sites featured bridges that either contained a protected median, a protected sidewalk, or a wide shoulder to provide the space to safely conduct the tests. A map of the bridge sites is shown in figure 120.

© 2023 Google® Maps™. Map Data: Google®, INEGI. Modifications by FHWA (See Acknowledgements section.)

Figure 120. Map. The bridge testing locations.[19]

A summary of all the testing is shown in table 23, with comparisons of the various cable diameters tested at each bridge, plus the range of out-of-roundness measured among all cables at each bridge, where out-of-roundness is averaged among all scans per cable. Table 23 also notes the furthest section of cable reached by the robot during testing for each bridge.

Table 23. Summary of the cable robot testing.

Bridge	Cables Tested	Total No. of Measurements	Cable Diameter (mm)	Minimum Out-of-Roundness (percent)	Maximum Out-of-Roundness (percent)	Furthest Section Tested
C&D Canal*	4	55	246	0.8	1.0	1
Indian River	9	153	151, 172, 192	1.2	5.2	2
Varina-Enon	6	84	220	0.9	1.8	1
Ironton-Russell	8	175	160, 181	1.9	2.9	2
U.S. Grant	9	258	200	0.8	1.2	2
East End	5	219	226	1.5	2.2	3
Robert N. Stewart	2	46	110	1.9	4.2	2
Lane Avenue	6	169	139	1.6	2.0	4
Pomeroy-Mason	9	240	160, 180	1.3	1.9	2
William H. Harsha	5	220	228	1.1	1.3	4
Arthur Ravenel	4	127	201, 227	2.5	3.9	2

*Note: This bridge has steel pipes.

Figure 121 is a bubble chart that helps visualize the correlation between out-of-roundness and cable diameter and compare the relationship between the two. All bridges are represented except for C&D Canal, which had steel pipes. The bubbles appear in four sizes, which correspond to the number of occurrences at each value of out-of-roundness.

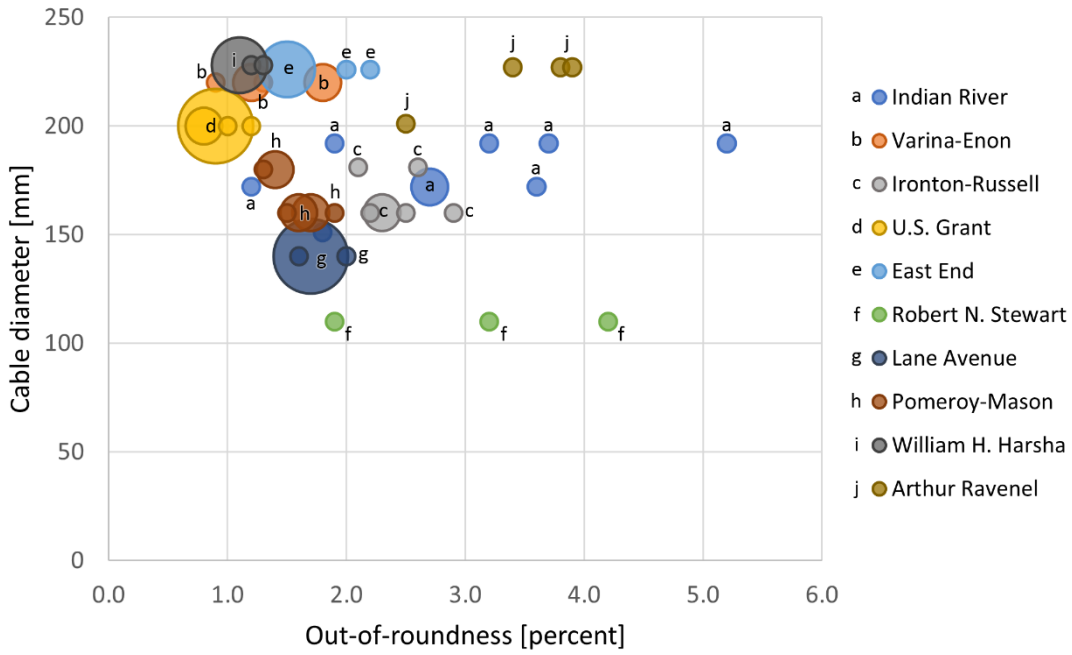

Source: FHWA.

Figure 121. Chart. Cable out-of-roundness versus cable diameter.

Two observations are immediately apparent from this chart. The first is that the bigger bubbles and greater concentration of data points occur below an out-of-roundness value of 2.0 percent, indicating that the majority of cables tested for this project, about 68 percent, had an out-of-roundness value between 0.8 and 2.0 percent. Values between 2.0 and 5.5 percent are mostly single occurrences that appear with less frequency. The second observation is that, while the cables on a specific bridge might have better or worse roundness values than another bridge with similar diameter cables, across all bridges, no apparent correlation exists between cable diameter and out-of-roundness.

CHAPTER 17. CONCLUSIONS

The FHWA Aerodynamics Laboratory designed and constructed a cable robot to climb stay cables and take cross-sectional measurements of the cables with accuracies up to 0.5 mm. During 3 years of testing, 11 different bridge sites were visited and a total of 67 individual cables were tested, recording over 1,700 roundness measurements. These measurements showed clear eccentricities in the cables' roundness, with out-of-roundness varying from about 1–5 percent.

Visualization plots were produced that showed exaggerated versions of the cables' cross-sectional shapes, useful for quickly spotting abnormalities in a cable's shape. These plots showed that, in certain cables, the individual subsections of pipes were not consistently aligned, proving that some cables in the field have varying cross sections along the length of the pipe, which introduces potential complexities into their wind-induced behavior.

A comparison of the cables' out-of-roundness versus diameter showed that no correlation exists for pipe diameter size and out-of-roundness. This plot also showed that the majority of cables tested, about 68 percent, have out-of-roundness values between 0.8 and 2 percent. Only 32 percent of the cables had larger out-of-roundness values of 2–5.2 percent.

The resulting cross-sectional data from the Indian River and Varina-Enon field tests were shared with NRC, who used 3D printing techniques to create scale models of some of the more interesting cable shapes from the shared measurements. NRC extensively tested these scale models in their wind tunnel in both static and dynamic scenarios to further study how eccentricities affect cable behavior. The results of these experiments were published by FHWA in two reports, *Wind-Tunnel Investigations of the Aerodynamics of Bridge Stay Cable Cross-Sectional Shapes* and *Aerodynamic Stability of Bridge Stay Cables—Dynamic Tests and Simulations*.[8,9]

The findings in this report point to several areas for further research related to cable roundness. While this project served as an important start to categorizing cable shapes, it represents only a fraction of the cables found in the field. Less than a third of current cable-stayed bridges in the United States were tested and the maximum number of cables tested on a single bridge was just nine. More cable testing is needed to more thoroughly categorize the typical cable shapes found in the field. In addition, a database of individual cross-sectional shapes could simultaneously be developed.

For verification purposes, cable HDPE pipe data collected from the cable manufacturers for the tested bridges should be compared with the measured results in this report. The cable manufacturers' cable data should be included in the database as well.

More information on the consistency of the cross-sectional shape along the length of the cable would be beneficial. One possible study could focus on both the individual sections of cable pipe and where multiple sections are combined to form the entire cable. Additionally, this data could be extrapolated to a 3D-printed scale model for potential future wind tunnel tests. Another area of future interest is to compare measured cross-sectional shapes relative to the age of the bridge to evaluate how the HDPE pipe shapes might change over time.

Finally, while the definition of out-of-roundness used in this report was a convenient method of comparison among all the cables and bridges tested, in the future, all interested parties should discuss and adopt a universally accepted definition for out-of-roundness.

The authors have a few suggestions for cable robot design improvements if the opportunity arises in the future to develop a second-generation robot. The climbing mechanism with the alternating clamps is quite slow and should be revisited. A faster driving system involving wheels or treads could permit more cables to be tested and more measurements recorded during a testing period. However, this change would also include a massive redesign. Therefore, if the requirement for this task is to keep the current clamp and crawling system, there are several improvements that could be reasonably implemented. By upgrading the robot with larger diameter shafts, the frame would be stiffer lengthwise, which, perhaps, would help create a more stable robot, but this change would also add weight. Adding large wheels on springs to ring A at the top would also help stabilize the robot as it performs its climbing routine. Replacing the precision ring with a ring that is completely free of imperfections, especially at the transition between ring halves, would ensure more accurate measurements. A permanent sun-screen mounted on the laser sensor ring would protect the sensors from interference caused by sunlight and shadows on the cable. Some of the uncertainty in the testing results can be eliminated by upgrading the robot to a two dimensional laser sensor that can more fully map the cables' cross sections, but an assessment is needed to see if this improvement is worth the cost. Finally, by moving the DAQ module to the robot and using the robot control cable only for supplying power and carrying control messages, the laptop programming can be simplified. This change could make the robot easier to control and help prevent laptop software crashes and other issues.

ACKNOWLEDGEMENTS

The map in figure 120 was modified. The original map is the property of Google® Maps™ and can be accessed from https://www.google.com/maps.[19] The image location markers and labels were added by FHWA.

REFERENCES

1. Post-Tensioning Institute. 2012. *Recommendations for Stay Cable Design, Testing and Installation*, Sixth Edition. Farmington Hills, MI: PTI.

2. Kumarasena, S., N. P. Jones, P. Irwin, and P. Taylor. 2007. *Wind-Induced Vibration of Stay Cables*. Report No. FHWA-HRT-05-083. Washington, DC: Federal Highway Administration.

3. Park, S., and H. R. Bosch. 2014. *Mitigation of Wind-Induced Vibration of Stay Cables: Numerical Simulations and Evaluations*. Report No. FHWA-HRT-14-049. Washington, DC: Federal Highway Administration.

4. Larose, G. L. 2014. *Wind Tunnel Investigations of an Inclined Stay Cable with a Helical Fillet*. Report No. FHWA-HRT-14-070. Washington, DC: Federal Highway Administration.

5. Bosch, H. R., and J. R. Pagenkopf. 2014. *Dynamic Properties of Stay Cables on the Penobscot Narrows Bridge*. Report No. FHWA-HRT-14-067. Washington, DC: Federal Highway Administration.

6. Bosch, H. R., and J. R. Pagenkopf. 2014. *Dynamic Properties of Stay Cables on the Bill Emerson Bridge*. Report No. FHWA-HRT-17-037. Washington, DC: Federal Highway Administration.

7. Bosch, H. R., and J. R. Pagenkopf. 2021. *Dynamic Properties of Stay Cables on the Leonard P. Zakim Bunker Hill Bridge*. Report No. FHWA-HRT-21-058. Washington, DC: Federal Highway Administration.

8. Christiansen, H., and G. L. Larose. 2021. *Wind-Tunnel Investigations of the Aerodynamics of Bridge Stay Cable Cross-Sectional Shapes*. Report No. FHWA-HRT-21-074. Washington, DC: Federal Highway Administration.

9. Larose, G. L., S. Stoyanoff, and B. Dunn. 2022. *Aerodynamic Stability of Bridge Stay Cables—Dynamic Tests and Simulations*. Report No. FHWA-HRT-22-097. Washington, DC: Federal Highway Administration.

10. Matteoni, G., and C. Georgakis. 2012. "Effects of Bridge Cable Surface Roughness and Cross-sectional Distortion on Aerodynamic Force Coefficients." *Journal of Wind Engineering and Industrial Aerodynamics* 104: 176–187.

11. Benidir, A., O. Flamand, L. Gaillet, and G. Dimitriadis. 2015. "Impact of Roughness and Circularity-defect on Bridge Cables Stability." *Journal of Wind Engineering and Industrial Aerodynamics* 137: 1–13.

12. Wang, X., and F. Xu. 2007. "Conceptual Design and Initial Experiments on Cable Inspection Robotic System." Presented at the *2007 International Conference on*

Mechatronics and Automation, Harbin, China. https://dx.doi.org/10.1109/ICMA.2007.4304149, last accessed March 29, 2023.

13. Xu, F., X. Wang, and L. Wang. 2011. "Climbing Model and Obstacle-Climbing Performance of a Cable Inspection Robot for a Cable-Stayed Bridge." *Transactions of the Canadian Society for Mechanical Engineering* 35, no. 2: 269–289. https://doi.org/10.1139/tcsme-2011-0016, last accessed March 29, 2023.

14. Kim, H., K. H. Cho, F. Liu, and H. Choi. 2011. "Development of Cable Climbing Robotic System for Inspection of Suspension Bridge." *2011 Proceedings of the 28th International Symposium on Automation and Robotics in Construction*. Seoul, Korea: ISARC. https://doi.org/10.22260/ISARC2011/0269, last accessed March 29, 2023.

15. Yun, H., S. Kim, L. Wu, and J. Lee. 2013. "Development of Inspection Robots for Bridge Cables." *The Scientific World Journal* 2013. https://doi.org/10.1155/2013/967508, last accessed March 29, 2023.

16. Xu, F., L. Wang, X. Wang, and G. Jiang. 2013. "Dynamic Performance of a Cable with an Inspection Robot—Analysis, Simulation, and Experiments." *Journal of Mechanical Science and Technology* 27, no. 5: 1479–1492. https://doi.org/10.1007/s12206-013-0328-2, last accessed March 29, 2023.

17. National Instruments. 1986. *LabVIEW* (software). Version 2015. https://www.ni.com/en-us/shop/labview.html, last accessed March 28, 2023.

18. Mathworks. 2006. *MATLAB* (software). Version 2017b. https://www.mathworks.com/, last accessed March 28, 2023.

19. Google®. 2023. *Google® Maps™*, Mountain View, CA. Obtained from: https://www.google.com/maps, last accessed March 28, 2023.

Recommended citation: Federal Highway Administration,
Development of a Cable Robot and Measurement of Stay Cable Roundness
(Washington, DC: 2024) https://doi.org/10.21949/1521476

HRDI-40/03-24(WEB)E